

**COMPRESSIVE POLAR SPECTRAL
AND POLARIZATION IMAGING**

by

Chen Fu

A dissertation submitted to the Faculty of the University of Delaware in partial fulfillment of the requirements for the degree of Doctor of Philosophy in Electrical & Computer Engineering

Spring 2018

© 2018 Chen Fu
All Rights Reserved

**COMPRESSIVE POLAR SPECTRAL
AND POLARIZATION IMAGING**

by

Chen Fu

Approved: _____
Kenneth E. Barner, Ph.D.
Chair of the Department of Electrical and Computer Engineering

Approved: _____
Babatunde Ogunnaike, Ph.D.
Dean of the College of Engineering

Approved: _____
Ann L. Ardis, Ph.D.
Senior Vice Provost for Graduate and Professional Education

I certify that I have read this dissertation and that in my opinion it meets the academic and professional standard required by the University as a dissertation for the degree of Doctor of Philosophy.

Signed: _____

Gonzalo R. Arce, Ph.D.
Professor in charge of dissertation

I certify that I have read this dissertation and that in my opinion it meets the academic and professional standard required by the University as a dissertation for the degree of Doctor of Philosophy.

Signed: _____

Javier Garcia-Frias, Ph.D.
Member of dissertation committee

I certify that I have read this dissertation and that in my opinion it meets the academic and professional standard required by the University as a dissertation for the degree of Doctor of Philosophy.

Signed: _____

Xiang-Gen Xia, Ph.D.
Member of dissertation committee

I certify that I have read this dissertation and that in my opinion it meets the academic and professional standard required by the University as a dissertation for the degree of Doctor of Philosophy.

Signed: _____

Daniel L. Lau, Ph.D.
Member of dissertation committee

I certify that I have read this dissertation and that in my opinion it meets the academic and professional standard required by the University as a dissertation for the degree of Doctor of Philosophy.

Signed: _____

Xu Ma, Ph.D.

Member of dissertation committee

ACKNOWLEDGEMENTS

It is my pleasure to express the deepest gratitude to my academic advisor Dr. Gonzalo Arce who has been strongly supporting me both academically and financially and providing me all his patience and tolerance during my entire Ph.D. study. I am very thankful for the contributions from our collaborators Dr. Henry Arguello, Dr. Brian Sadler and Dr. Michael Don in this research work. I appreciate all the support and help from my colleagues in Dr. Arce's research group. I'm also very grateful to the members of my dissertation committee, Dr. Javier Garcia-Frias, Dr. Xiang-Gen Xia, Dr. Daniel Lau and Dr. Xu Ma for their valuable time and suggestions. I'd like to express my thanks to our funding sources, Army Research Office, Army Research Laboratory, B&W Tech, Intel Corporation and National Science Foundation. I am deeply indebted to my wife, who has been with me since the second year of my Ph.D., taking care of my life, sharing all the happiness and sadness. And I'd also like to thank my parents and parents-in-law who fully respect and support my pursuit of this doctoral degree.

TABLE OF CONTENTS

LIST OF TABLES	ix
LIST OF FIGURES	x
ABSTRACT	xviii

Chapter

1 INTRODUCTION	1
1.1 Spectral Imaging	1
1.2 Spectral Polarization Imaging	4
1.2.1 Introduction to Polarization	4
1.2.2 Conventional Spectral Polarization Imaging	6
1.3 Introduction to Compressive Sensing	9
1.3.1 Compressive Sampling Theory	9
1.3.2 Signal Reconstruction	10
1.3.3 Incoherence Property	11
1.3.4 Restricted Isometries	12
1.4 Compressive Imaging	12
1.4.1 Single-pixel Camera	13
1.4.2 Compressive Spectral Imaging	14
1.4.3 Compressive Spectral Polarization Imaging	15
1.4.4 Other Compressive Sensing Applications In Imaging Systems	17
1.5 Dissertation Format	18
1.6 Original Contributions	18
1.7 Journal and Conference Publications	19

2	COMPRESSIVE SPECTRAL IMAGING VIA A POLAR CODED APERTURE	21
2.1	Introduction and Related Research Work	21
2.2	Polar Coded Aperture Compressive Spectral Imaging System	24
2.2.1	Discrete Imager Rotation Sensing Model	24
2.2.2	Discussion on the Spectral Resolution	29
2.2.3	Sensing Model of the Rectangular FPA sensors	31
2.2.4	Sensing Matrix of Discrete Rotation Model	33
2.2.5	Spectral Data Cube Recovery	36
2.3	Polar Coded Aperture Geometry Design	37
2.4	Computer Simulations	42
2.4.1	Polar Data Cube Acquisition and Measurements Simulation	42
2.4.2	Reconstruction with Simulated Measurements	44
2.4.3	Influence of the Bandpass Filter Bandwidth	47
2.4.4	Hyper-Spectral Reconstruction	48
2.5	Continuous Imager Rotation Model	49
2.6	Conclusion	54
3	OPTIMIZATION AND EXPERIMENTAL DEMONSTRATION OF A COMPRESSIVE POLAR CODED APERTURE SPECTRAL IMAGER	56
3.1	Introduction	56
3.2	Polar Coded Aperture Optimization	59
3.3	Computer Simulations	65
3.4	Experimental Validation	73
3.5	Conclusion	81
4	COMPRESSIVE SPECTRAL POLARIZATION IMAGING BASED ON A PIXELATED POLARIZER	82
4.1	Introduction	82
4.2	Spectral Polarization Compressive Sensing System	85
4.3	Design of The Micropolarizer and The Colored Filter Array	92
4.4	Reconstruction Using Designed Coded Apertures	93
4.5	Prism Rotation for Multi-shot Acquisition	98

4.6	Laboratory Experiments	101
4.6.1	Hardware Implementation and Calibration	101
4.6.2	Experimental Results	102
4.7	Conclusion	109
5	CONCLUSIONS AND FUTURE WORK	111
	REFERENCES	113
	Appendix	
A	COPYRIGHT NOTICE	121
B	DISCLAIMER	122

LIST OF TABLES

3.1	PSNR comparison between random aperture code and optimized code reconstruction with different numbers of snapshots.	73
-----	---	----

LIST OF FIGURES

1.1	Three-dimensional spectral image cube containing two spatial dimensions x and y , as well as the spectral dimension λ [1].	2
1.2	Experimentally captured multi-spectral image bands from 440nm to 660nm.	2
1.3	Illustration of a spectral-scanning method [2] on left and a spatial-scanning approach [3] on right for conventional spectral image bands acquisition.	3
1.4	A multi-spectral sensor array where multiple spectral channels are sensed simultaneously through the division of focal plane.	4
1.5	Demonstration of an optical wave. The orientation of its electrical field is orthogonal to its propagation direction. This orientation is characterized by polarization.	4
1.6	The vector space demonstration of Stokes parameters, AoP and DoLP.	6
1.7	Polarization intensity images are captured via rotating a linear polarizer, shown in the first row. The second row displays the calculated Stokes images.	7
1.8	DoLP image is displayed on the left, where the brightness represents the degree of linear polarization. AoP image is shown on the right, where false color is used for polarization angle visualization.	8
1.9	One example of a real-time polarization imaging system consisting of several polarization beam-splitters, retarders and cameras [6].	8
1.10	Division of focal plane polarization imaging where a micro-polarizer array is used [4].	9

2.1	Compressive spectral imaging architecture with a polar coded aperture and a continuous viable circular bandpass filter. Compressed projections are captured on the FPA detector.	23
2.2	Geometry illustration of the proposed polar coded aperture. The number of spokes in outer rings is twice of the spokes in inner rings.	25
2.3	Discretized compressive sensing phenomenon of polar imager. The q^{th} ring of the data cube f_{srk} is coded by the polar coded aperture and modulated by the continuous variable circular bandpass filter. The modulated light is integrated in both spatial and spectral domains, captured by the FPA sensors.	26
2.4	Illustration of the spectral modulation of the filtered polar data cube. Two spectrally adjacent polar data cube voxels are modulated in spectrum as passing through a continuous variable circular bandpass filter pixel.	27
2.5	Coding matrix \mathbf{P}^ℓ for $S_{in} = 8, S_{out} = 16, R_{in} = 2, R_{out} = 1, L = 2$ data cube. The entries represent the spatial and spectral modulation factors on the polar data voxels, with 0 entries remaining black. . .	29
2.6	The polar pixels in k^{th} spectral band that can be sensed by the continuous variable filter are concentrated in the region of \mathbf{R}_k^ℓ . This spectral band is split into two sub-bands where the sensed polar pixels are concentrated in two smaller regions $\mathbf{R}_{k_1}^\ell$ and $\mathbf{R}_{k_2}^\ell$	30
2.7	Weight matrix \mathbf{W} for a $S_{in} = 8, S_{out} = 16, R_{in} = 2, R_{out} = 1, L = 2$ data cube and an $N^2 = 4^2$ FPA. The entries with larger values are displayed in brighter points, while the 0 entries remain black.	33
2.8	Sensing matrix \mathbf{H}^ℓ for a $S_{in} = 8, S_{out} = 16, R_{in} = 2, R_{out} = 1, L = 2$ data cube and an $N^2 = 4^2$ FPA.	34
2.9	As the imager rotates, the spatial coding provided by the polar coded aperture is circularly shifting the spokes. The imager is assumed to be static when snapshots are captured, and d_r spokes are shifted between adjacent shots.	35
2.10	One polar image band is transformed into two rectangular matrices representing the inner and outer rings polar image pixels.	36

2.11	(a)-(c) show different polar aperture geometry designs with the shapes polar pixels being analyzed: (a) and (b) show the spoke-ring aperture structure with $S/R = 1$ and $S/R = 4$, respectively; (c) shows the inner-outer rings design. (d)-(f) are the examples of polar images with the corresponding polar pixels geometry in (a)-(c), respectively.	38
2.12	The shape of a polar pixel with rings distance a_{sr} and spokes distance b_{sr} .	39
2.13	Plot of the cost function value changing with the spoke-ring ratio S/R varying from 1 to 16.	40
2.14	Plots of the cost function value changing with the inner-total rings ratio $\varepsilon \in [0, 1]$ in both 128 inner spokes and 256 inner spokes coded apertures.	41
2.15	Comparison of image quality with 6 (left), 20 (middle) and 60 (right) inner rings with the polar pixel number restricted to be 128^2 . Better image quality with 20 inner rings is observed in both zoomed regions.	41
2.16	9 spectral image bands selected from the total 16 bands are displayed. The center wavelength of each band is indicated. Two image points are selected for the spectral reconstruction comparisons.	43
2.17	(a) shows the RGB images of the spatial and spectral modulated polar data cube before projected on the FPA detector. (b) shows the corresponding compressed FPA projections. 4 snapshots selected from the total 64 snapshots are displayed.	44
2.18	16 spectral image bands are reconstructed from 64 snapshots compressed measurements with $\kappa = 25\%$ CS ratio, where 9 image bands are displayed. The average PSNR is 32dB.	45
2.19	Average PSNRs are calculated for different polar coded aperture geometry designs with the number of snapshots ranging from 4 to 128. The corresponding CS ratio ranges from 1.56% to 50%.	46
2.20	PSNRs of 8, 16 and 32 spectral bands reconstructions from 64 snapshots are displayed with γ varying from 0.02 to 1.	48

2.21	The original 580nm image plane (a) and its corresponding reconstruction (b) are displayed. 40dB PSNR is achieved with $\kappa = 25\%$. Two image points are selected for spectral signature reconstruction comparisons.	49
2.22	128-band spectral reconstructions are compared with the original spectral signatures of two image points. The reconstructions of 20 bands from 571nm to 590nm are zoomed for further comparisons.	50
2.23	(a) shows a data pixel entering the polar coded aperture with no transformation, when the discrete approximation of the imager rotation is applied. (b) displays a circularly sheared data pixel hitting two adjacent polar aperture pixels, when the continuous rotation motion of the imager is considered.	51
2.24	Sensing matrix in the continuous rotation model \mathbf{H}^ℓ for a $S_{in} = 8$, $S_{out} = 16$ $R_{in} = 2$, $R_{out} = 1$, $L = 2$ data cube and an $N^2 = 4^2$ FPA.	52
2.25	PSNR comparison between discrete rotation model reconstruction and the continuous rotation model reconstruction. 64 continuous rotation compressed projections are simulated with the normalized shutter time η increasing from 0 to 1.	53
2.26	(a) shows the 4th spectral image band reconstructed by applying the continuous rotation model, with 30.1dB PSNR; (b) displays the same spectral band recovered by utilizing the discrete rotation model with the corresponding PSNR 23.6dB.	54
3.1	(a) shows the affected region by swapping and toggling operations to one pixel. The corresponding affected columns in \mathbf{W}^1 is shown in (b).	63
3.2	The optimized coded aperture (right) is compared with the initial random coded aperture (left) with 12% unblock pixels.	65
3.3	Comparison of the statistics before (left column) and after (right column) optimization. Upper row shows the histogram of the number of sensors sensing one voxel. Lower row shows the histograms of the number of voxels sensed by a certain sensor.	66
3.4	Singular values of the measurement matrices before and after optimization are plotted. Coded aperture optimization leads to a better conditioned measurement matrix.	67

3.5	Reconstruction performance of a set of optimized aperture codes with initial transmittance ranging in $[0.06, 0.4]$. The performance of a 50% random code is plotted as a reference.	69
3.6	Simulations with 12% unblocked random code, 50% blocked random code and the optimized code are performed. PSNR values are computed for each reconstructed spectral image plane. Comparisons show a significant PSNR increase when the optimized coding is used.	70
3.7	Comparison among the original 6 th spectral band in (a), the reconstructed spectral band with random aperture code in (b) and the reconstructed image plane after optimization in (c). Their reconstruction absolute error image planes are shown in (d) and (e), respectively.	71
3.8	Comparison among the original 10 th spectral band in (a), the reconstructed spectral band with random aperture code in (b) and the reconstructed image plane after optimization in (c). Their reconstruction absolute error image planes are shown in (d) and (e), respectively.	72
3.9	Designed photo-mask containing random and optimized polar coding patterns. Microscope zoomed images of two coding patterns are displayed.	74
3.10	Polar coded aperture compressive spectral imaging system consists of an objective lens, a polar coded aperture on a photo-mask, a CVF emulated with bandpass color filters, a relay lens and a monochrome sensor array.	75
3.11	Target mounted on a motorized rotation stage.	76
3.12	(a) The ideal binary polar pattern with 128^2 polar pixels. (b) The calibrated polar pattern from the experimental imaging system. Optical distortion and vignetting compensation is considered by using the calibrated coding pattern in the reconstruction.	77
3.13	An RGB image of the imaging target is shown in the left figure. The right figures are four low-resolution measurement images captured and down-sampled from the experimental imaging system.	77

3.14	A total 16 spectral image bands are reconstructed from 64 low resolution measurements. The spectral range is from 500nm to 650nm. 9 of the 16 spectral bands are selected for display.	78
3.15	Comparison of random (top) and optimized (bottom) reconstructions. Letters “LABOR” are enlarged for a detailed comparison. The optimized coding pattern resolves letters “BOR” more clearly than random coding patterns in both bands.	79
3.16	Spectral signatures of points P_1 and P_2 on the target shown in Fig. 3.15 are experimental measured through a spectrometer. The spectrometer measurements are then compared with the reconstructions using random and optimized coded apertures. The optimized spectral reconstructions fit the spectrometer measurements better.	80
4.1	Proposed compressive spectral polarization imaging system consisting of an objective lens, a colored detector with micropolarizer array aligned, and a prism. Multi-snapshots are achieved by prism rotation.	85
4.2	A micropolarizer array consisting of four angles of polarization is aligned to the colored detector with the same pixel pitch.	86
4.3	Illustrative example of the sensing matrix $\mathbf{H} = [\mathbf{H}_0, \mathbf{H}_1, \mathbf{H}_2, \mathbf{H}_3]$ for $N = 6, L = 3$. To show the influence of the micro-polarizer array $\mathbf{u}_c^k, \mathbf{t}_k$ is assumed to be an all ones vector for each channel.	89
4.4	Illustrative example of matrix $\mathbf{G} = [\mathbf{S}_0, \mathbf{S}_1, \mathbf{S}_2]$ for $N = 6, L = 3$. The corresponding H matrix is taken from Figure 3. White points have the values of $\frac{1}{2}$; green points have the values of $-\frac{1}{2}$; Black points are zero-valued entries.	91
4.5	(a) A random code forms clusters. (b) The designed code reduces the clusters and achieves a more uniform sensing across the FPA.	92
4.6	Test linear polarization intensity image planes in four spectral channels.	94
4.7	Ground truth of S_0, S_1 and S_2 image planes. Each Stokes parameter image plane is displayed in four of eight spectral channels: 500nm, 530nm, 580nm and 620nm.	95

4.8	S_0 , S_1 and S_2 image planes reconstructed with single simulated shot random codes are displayed in four of eight spectral channels. The CS ratio is $\kappa = 4.3\%$. The average PSNRs for each Stokes image plane are also indicated.	96
4.9	S_0 , S_1 and S_2 image planes reconstructed with a single simulated shot with designed codes are displayed in four spectral channels. The CS ratio is $\kappa = 4.3\%$. The average PSNRs for each Stokes image plane are indicated.	97
4.10	A spectral image plane is projected onto four different FPA locations, corresponding to the four prism rotation angles. This induces four different coding patterns.	99
4.11	S_0 , S_1 and S_2 image planes reconstructed from 4 simulated snapshots are displayed in four spectral channels. The CS ratio is $\kappa = 17\%$. The average PSNRs for each Stokes image plane are indicated.	100
4.12	Laboratory implementation of the proposed architecture. Coded projections are acquired on a CCD camera.	101
4.13	(a): The target is captured by an RGB camera. Two points P_1 and P_2 are selected for spectral signature comparison. (b)-(i): Reconstructed S_0 image planes are displayed at all 8 spectral wavelengths from 505nm to 650nm.	104
4.14	Reconstructed S_1 image planes at 8 spectral wavelengths and the average reconstruction of S_2 image plane. The S_1 image planes have the same intensities as reconstructed S_0 images because in this experiment the target is 0° polarized. Also, as expected, the average S_2 image plane has zero intensity.	105
4.15	Spectral reconstructions of two selected points are compared with a spectrometer measurement.	106
4.16	Reconstructed S_1 image planes at 600nm are shown for different polarization angles. The intensity of S_1 images changes with the azimuth angle of the linear polarizer.	107
4.17	Reconstructed S_2 image planes at 600nm are shown for different polarization angles. The intensity of S_2 images changes with the azimuth angle of the linear polarizer.	107

4.18	(a): The target is captured by an RGB camera. (b)-(i): Reconstructed S_0 image planes are displayed at all 8 spectral wavelengths from 505nm to 650nm.	108
4.19	Reconstructed S_1 image planes at 8 spectral wavelengths are displayed. The polarizer film covering the eyes of the toy has strong positive S_1 components. Strong negative S_1 is observed with the polarizer film covering the legs of the toy.	109
4.20	(a)-(h): Reconstructed S_2 image planes at 8 spectral wavelengths are displayed. The sword shaped polarizer film has strong negative S_2 components. (i): AoP image represented by pseudo color is computed at 625nm.	110

ABSTRACT

Conventional digital imaging captures the desired image information directly on an imaging sensor. When high dimensional imaging capability is required such as spectral imaging and spectropolarimetric imaging, inefficient sampling strategies are usually involved, such as scanning and division of the focal plane array, resulting in either poor real-time imaging capability or sensor resolution reduction. Compressive sensing solves these problems via sampling of the high-dimensional image cubes below the Nyquist sampling rate, and recovering the image signal with sparsity constraints. In this dissertation, a newly proposed compressive spectral imaging and a compressive spectropolarimetric imaging system are described. In particular, a novel polar-shaped pixelated coding mask is proposed, optimized and implemented in spinning imaging systems. Multi-snapshots are achieved through the coding mask rotation. By combining with a circular variable filter and a low-resolution monochrome sensor array, super-resolution in both spatial and spectral dimensions is attained. Both the geometry and the pattern of binary polar coded aperture are further optimized. A continuous imager rotation model is developed and simulated to resolve the rotation blur. Finally, the imaging system is tested with experimental measurements and reconstructions. On the other hand, a compressive spectropolarimetric imager is developed based on a micro-polarizer array, aiming at obtaining spectral linear Stokes images. Simulation shows a blue-noise pattern of micro-polarizer distribution highly improves the polarization reconstruction quality. A rotating double-amici prism further enables multi-snapshots. Reconstructions of spectral Stokes images as well as the degree and angle of polarization (DoP and AoP) images are then obtained from testbed experiments.

Chapter 1

INTRODUCTION

1.1 Spectral Imaging

Optical spectroscopy measures the intensity of light across different wavelengths. It's typically used for measuring the light reflection or absorption propensities of material along the spectrum, where important information on material and molecule structure can be extracted. Conventional spectroscopy employs dispersive optical elements for spectrum separation. The sampling on spectrum is usually performed by a line sensor. The spectrum dispersion and line sensor resolution determines the ability of separating neighborhood spectrum, thus determines the spectral resolution.

Spectral Imaging is a combination of two-dimensional (2D) imaging and spectroscopy [1]. It captures intensity images across a number of spectral channels, and for each image point, its spectral signature is measured. Thus, spectral imaging captures a three-dimensional (3D) image cube $f(x, y, \lambda)$, where λ represents the wavelength, as shown in Fig. 1.1. The intensity image in each spectral channel is called a spectral band. Common RGB cameras carry three broad spectral bands in visual range, while typical spectral imaging captures much more bands and the sensitivity spectral range is not limited to visible or infrared (IR). Based on the spectrum resolution requirement, spectral imaging is sometimes named as multi-spectral imaging or hyper-spectral imaging. Figure 1.2 shows an example of 12 spectral image bands captured in our laboratory using a visible monochrometer.

Spectral imaging collects a large amount of image data. Thus conventional spectral imaging techniques usually involve scanning during the measuring process. Based on the scanned image dimension, the scanning strategies are roughly categorized as

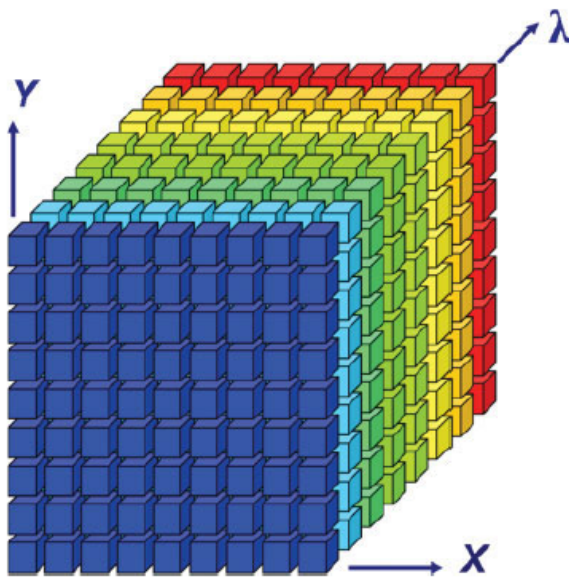


Figure 1.1: Three-dimensional spectral image cube containing two spatial dimensions x and y , as well as the spectral dimension λ [1].

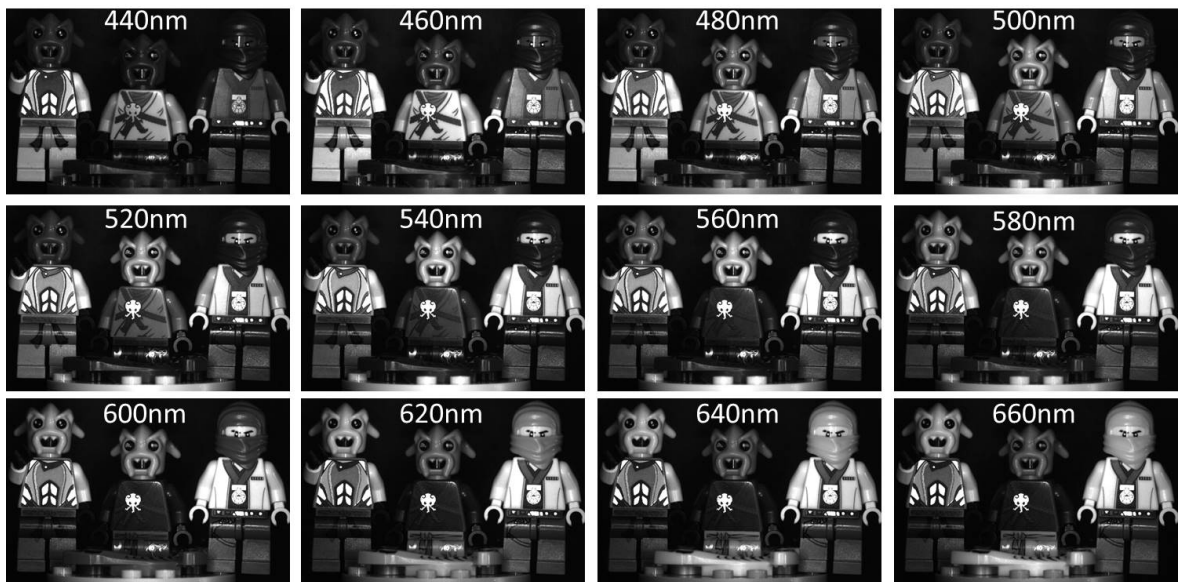


Figure 1.2: Experimentally captured multi-spectral image bands from 440nm to 660nm.

spectral-scanning and spatial-scanning, as shown in Fig. 1.3. Spectrum scanning usually involves switching a set of narrow-band color filters. Circular variable filters or tunable filters are the alternatives. Tunable filter does not require mechanical movement and has the advantage of user-selective spectral range and channel bandwidth. The spectral-scanning approaches work well when a small number of spectral channels are required for a static scene. For narrow spectral bands, it raises the low-light sensitivity requirement for the imaging sensor. The spatial-scanning spectral imaging systems capture the entire spectrum of an image line, and perform line-by-line scanning of the scene. Measuring a dynamic scene using the spatial-scanning method can be very challenging. For static scenes, usually additional post-processing should be involved to solve the problem of image misalignment.

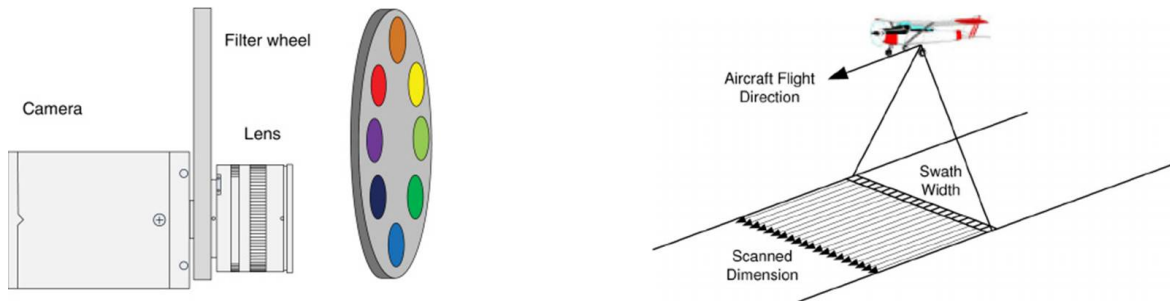


Figure 1.3: Illustration of a spectral-scanning method [2] on left and a spatial-scanning approach [3] on right for conventional spectral image bands acquisition.

The biggest disadvantage of the above scanning-based methods is the sacrifice of the measurement speed, making the mission impossible for some real-time applications such as live-cell spectral imaging. To solve this problem, a division of focal plane (DoFP) strategy was proposed. The imaging sensor is divided into several regions in order to measure multiple spectral bands simultaneously, as shown in Fig. 1.4. This strategy, on the other hand, sacrifices the sensor resolution for spectral information. Interpolations can be employed to recover the full spatial resolution for each spectral bands, however achieving decent recovery can be very challenging when a large number of spectral channels are required.

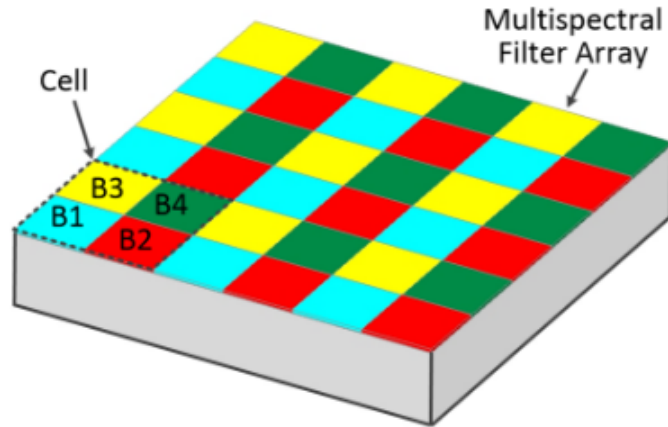


Figure 1.4: A multi-spectral sensor array where multiple spectral channels are sensed simultaneously through the division of focal plane.

1.2 Spectral Polarization Imaging

1.2.1 Introduction to Polarization

Polarization is defined as the orientation of the electrical field of optical waves, as shown in Fig. 1.5. It's an important property of light but usually can not be directly measured on an intensity sensor. Polarization carries important structure information on object surfaces, such as the orientation and roughness [4].

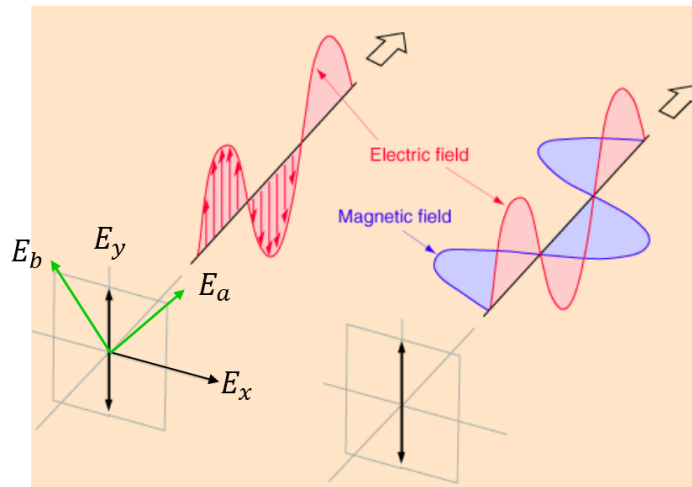


Figure 1.5: Demonstration of an optical wave. The orientation of its electrical field is orthogonal to its propagation direction. This orientation is characterized by polarization.

Polarization can be classified as linear polarization and circular polarization. If the electrical fields of light waves have a single and time-invariant orientation, the

light is linearly polarized. The linear polarization angle ranges from 0 to π . While circular polarization refers to the situations where the orientations of the electrical field rotate during the propagation. Based on the rotation direction, it's categorized as left-handed and right-handed circular polarization. Nature light is composed of a uniform mixture of polarization state thus it is considered as unpolarized. Reflections are usually partial-polarized, which is a mixture of unpolarized and polarized light. For partial-polarized light, one can define the degree of polarization, which represents the percentage of polarized light among all its intensity.

Mathematically, the polarization is represented with a Stokes vector containing four Stokes parameters. The first three Stokes parameters define the state of linear polarization: S_0 is the intensity of light; S_1 is the intensity difference between 0° and 90° polarization, while S_2 measures the intensity difference between 45° and 135° polarization. The last Stokes parameter represents the state of circular polarization: it's defined as the intensity difference between the left and right-handed polarization. Their relationships are listed below:

$$S_0 = I_0 + I_{90}; \quad (1.1)$$

$$S_1 = I_0 - I_{90}; \quad (1.2)$$

$$S_2 = I_{45} - I_{135}; \quad (1.3)$$

$$S_3 = I_L - I_R; \quad (1.4)$$

where I_θ is the intensity of θ° polarization. I_L and I_R represent the left and right handed circular polarization, respectively. The degree of polarization (DoP) is calculated from

$$\text{DoP} = \frac{\sqrt{S_1^2 + S_2^2 + S_3^2}}{S_0}. \quad (1.5)$$

For linear polarized light, the angle of polarization (AoP) is defined as

$$\text{AoP} = \frac{1}{2} \arctan\left(\frac{S_2}{S_1}\right). \quad (1.6)$$

While the degree of linear polarization (DoLP) usually calculated as

$$\text{DoLP} = \frac{\sqrt{S_1^2 + S_2^2}}{S_0}. \quad (1.7)$$

The relationship among AoP, DoP, DoLP and the Stokes parameters are demonstrated in Fig. 1.6, where I is the light intensity, i. e. S_0 , and p represents the degree of polarization. Thus $I p$ provides the total energy of the polarized light. In the polarized portion of light, the orientation of the electrical field is specified through a 3D space defined by S_1 , S_2 and S_3 . In particular, the AoP and DoLP are defined in the S_1 - S_2 plane.

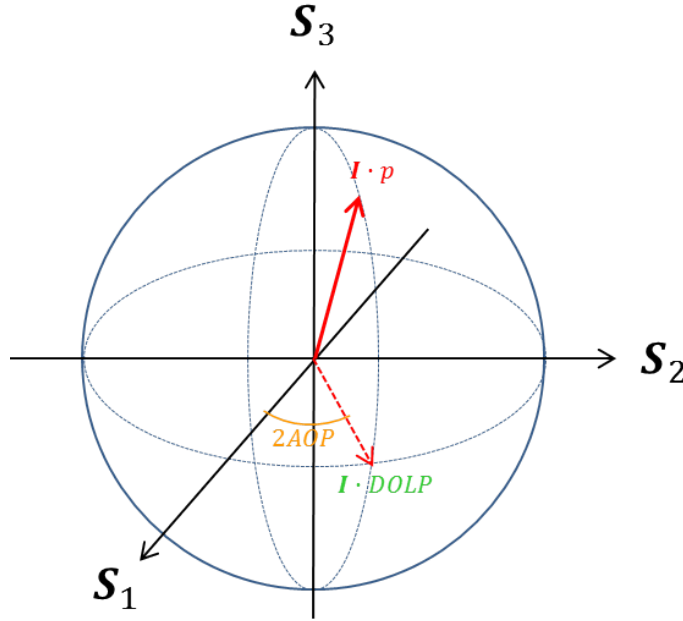


Figure 1.6: The vector space demonstration of Stokes parameters, AoP and DoLP.

1.2.2 Conventional Spectral Polarization Imaging

Polarization imaging measures the Stokes vector for each pixel across the scene. Thus four images are desired for four Stokes parameters. The most straightforward

polarization imaging method involves the rotation of a linear polarizer [5]. After obtaining images for 0° , 45° , 90° and 180° polarization, the linear Stokes image planes can be directly calculated from the above equations. This is considered as a polarization-scanning approach. In the laboratory, we captured the polarization intensity images via rotating a linear polarizer at four rotation angles: 0° , 45° , 90° and 180° . Figure 1.7 shows the polarization intensity images as well as the calculated Stokes images. As only linear polarization information is captured, the first three Stokes parameters are obtained. Then the images of DoLP and AoP are computed and displayed in Fig. 1.8.

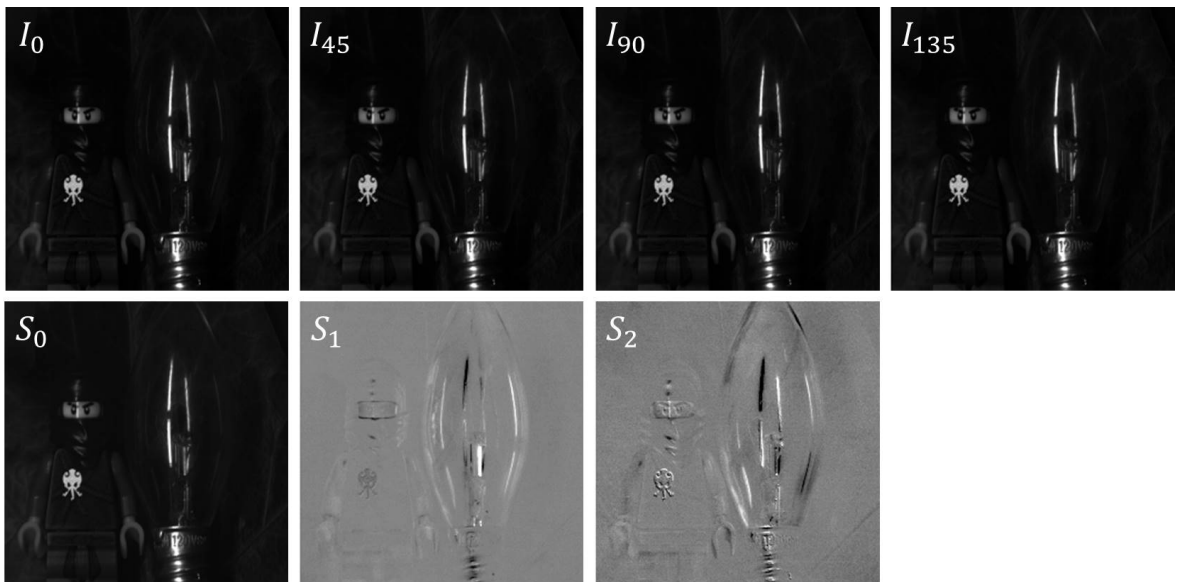


Figure 1.7: Polarization intensity images are captured via rotating a linear polarizer, shown in the first row. The second row displays the calculated Stokes images.

In order to avoid scanning, efforts were made in designing real-time polarization imaging systems. One such system is composed of multiple cameras, a set of polarization beam-splitters and retarders [6], as shown in Fig. 1.9. Each camera is able to capture a different Stokes image. Real-time capability is thus achieved with a tremendous increase of system complexity. Figure 1.10 shows another approach for real-time polarization imaging via the division of focal plane array, where a pixelated polarizer

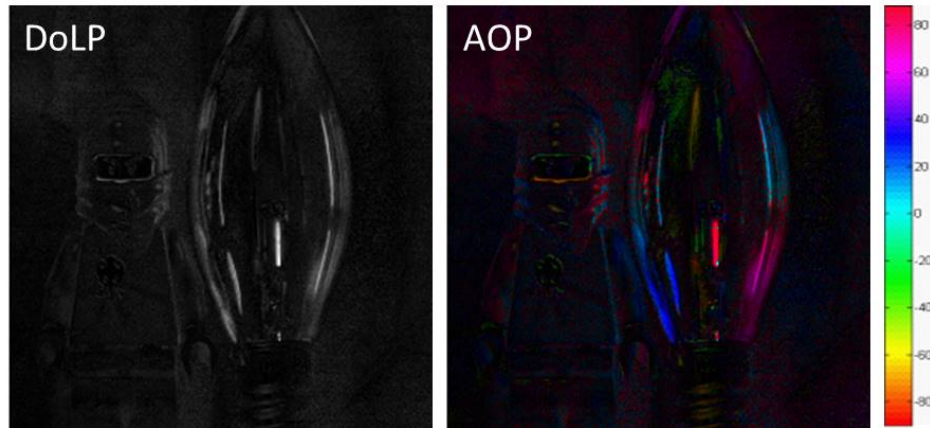


Figure 1.8: DoLP image is displayed on the left, where the brightness represents the degree of linear polarization. AoP image is shown on the right, where false color is used for polarization angle visualization.

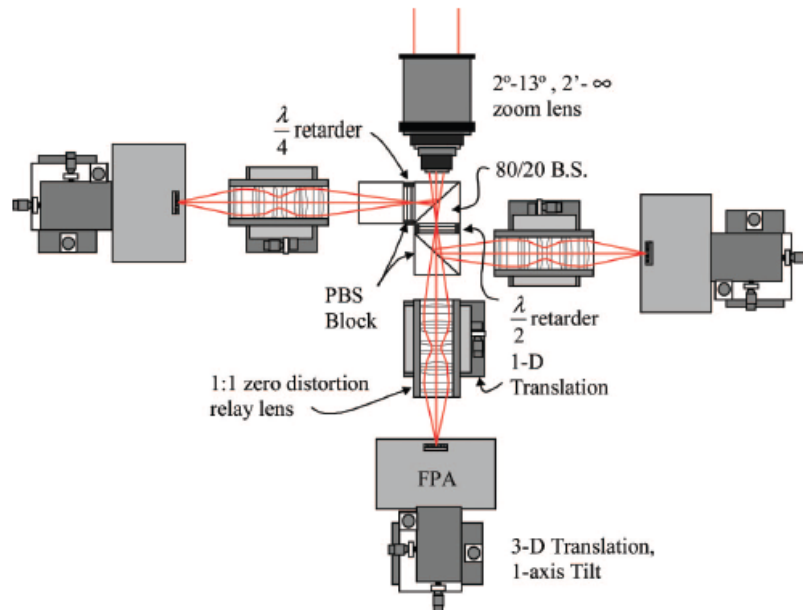


Figure 1.9: One example of a real-time polarization imaging system consisting of several polarization beam-splitters, retarders and cameras [6].

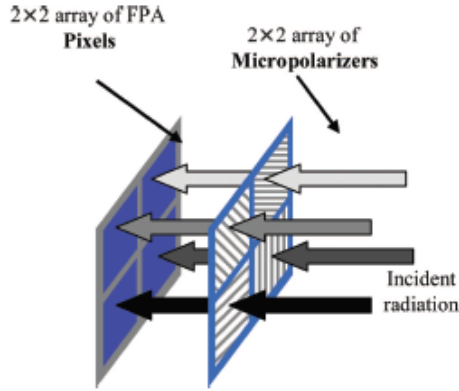


Figure 1.10: Division of focal plane polarization imaging where a micro-polarizer array is used [4].

is usually involved to capture different polarization angle at different sensor locations. This method is less complex but the sensor resolution is reduced in a factor of four.

A four-dimensional (4D) description of the scene can be obtained through combining different polarization imaging and spectral imaging approaches. In particular, the spectral and polarization information is simultaneously obtained through a channeled spectropolarimetry [7], where a set of polarizers and retarders are applied to modulate the Stokes vectors and the spectrum. Fourier transforms are involved to demodulate the Stokes vector from spectrometer measurements. This method has the potential to be transformed into imaging application; however it suffers from channel cross-talk and a reduction of spectral resolution.

1.3 Introduction to Compressive Sensing

1.3.1 Compressive Sampling Theory

Nyquist sampling theory suggests a sampling rate at least two times of the maximum frequency in the signal. This rate is called Nyquist sampling rate. Based on this theory, when sampling below Nyquist rate, it is necessary to apply a low-pass filter to band-limit the signal [8]. Compressive sensing theory, on the other hand, suggests one can perfectly recover the signal from samples obtained below the Nyquist sampling rate. This is based on the assumption on the sparsity of the signal. Image signals, for

example, are largely redundant in both intensity and color. With a proper transformation basis, such as 2D Wavelet or 2D DCT, the image signal can be represented with the corresponding sparse coefficients. If the number of non-zero coefficients is far less than the length of the signal, sampling strategies can be designed aiming at the recovery of the sparse coefficients with much fewer samples.

Mathematically, a N length signal \mathbf{f} can be represented as $\mathbf{f} = \mathbf{\Psi}\boldsymbol{\theta}$, where $\mathbf{\Psi}$ is a set of basis, and $\boldsymbol{\theta}$ is the sparse representation of the original signal \mathbf{f} . \mathbf{f} is S sparse if there are S number of non-zero elements in the sparse coefficients, where $S \ll N$. Compressive sensing measures M -length sample vector ($M \ll N$) \mathbf{g} through a measurement matrix \mathbf{H} . This sensing process is represented as

$$\mathbf{g} = \mathbf{H}\mathbf{f} = \mathbf{H}\mathbf{\Psi}\boldsymbol{\theta}. \quad (1.8)$$

The multiplication between measurement matrix and basis $\mathbf{A} = \mathbf{H}\mathbf{\Psi}$ is usually named sensing matrix.

1.3.2 Signal Reconstruction

The reconstruction of the original signal \mathbf{f} is then transferred into the recovery of the sparse representations $\boldsymbol{\theta}$. Notice that the sensing matrix is highly under-determined. In order to narrow down the solution set, compressive sensing takes the sparsity as prior information. In mathematics, ℓ_0 -norm counts the non-zero elements in the signal vector, thus is a perfect measurement for sparsity. However, ℓ_0 minimization is NP hard. Instead ℓ_1 -norm is most commonly used in compressive sensing for the sparsity measuring. Thus the inverse problem can be converted into solving a ℓ_1 regularized optimization problem,

$$\min_{\boldsymbol{\theta}} \|\mathbf{g} - \mathbf{A}\boldsymbol{\theta}\|^2 + \tau|\boldsymbol{\theta}|_1, \quad (1.9)$$

where τ is a regularization constant. After the reconstruction of $\boldsymbol{\theta}$, the original signal \mathbf{f} can then be recovered from $\mathbf{f} = \mathbf{\Psi}\boldsymbol{\theta}$.

The reconstruction quality can be quantified using Peak Signal-to-Noise Ratio (PSNR). The PSNR of a recovered image is defined as

$$\text{PSNR} = 10\log_{10}\left(\frac{\mathbf{f}_{\max}}{\sqrt{E_{\text{mse}}}}\right), \quad (1.10)$$

where \mathbf{f}_{\max} is the maximum possible value of the elements in \mathbf{f} . For 8-bit images, this number is 256. E_{mse} represents the mean square error between the original signal and the reconstruction. A larger value of PSNR generally indicates a better reconstruction quality.

1.3.3 Incoherence Property

Compressive sensing does not only rely on signal sparsity. The selection of sampling strategy is also critical to the signal reconstruction quality. Coherence is usually used to measure the condition of a sensing matrix. Mutual coherence is defined as the largest correlation between the sensing basis and the representation basis [8]. Mathematically it's represented as

$$\mu(\mathbf{H}, \mathbf{\Psi}) = \sqrt{N} \max_{1 \leq k, j \leq N} |\langle \mathbf{H}_k, \mathbf{\Psi}_j \rangle|. \quad (1.11)$$

Improving the incoherence in compressive sensing usually results in the increase of reconstruction quality. In theory, perfect signal reconstruction is guaranteed when the number of compressed measurement M satisfies

$$M \geq C\mu^2(\mathbf{H}, \mathbf{\Psi})S\log(N), \quad (1.12)$$

where C is a constant. Efforts can be made to achieve incoherence with careful selections of sensing basis and representation basis. Statistically, random sampling guarantees the incoherence with any representation basis. Thus random sampling strategy is commonly employed in compressive sensing architectures.

1.3.4 Restricted Isometries

Despite of incoherence, another important factor to evaluate the condition of the sensing matrix is so-called the restricted isometry property (RIP) [8], where the restricted isometry constant δ_S is defined as the smallest number such that

$$(1 - \delta_S)\|\boldsymbol{\theta}\|_{\ell_2}^2 \leq \|\mathbf{A}\boldsymbol{\theta}\|_{\ell_2}^2 \leq (1 + \delta_S)\|\boldsymbol{\theta}\|_{\ell_2}^2 \quad (1.13)$$

holds for all S -sparse signal $\boldsymbol{\theta}$. Thus the Euclidean norm of the the sparse signal $\boldsymbol{\theta}$ is preserved after going through the linear system \mathbf{A} . In order to successfully recover the desired signal $\boldsymbol{\theta}$, the sensing matrix \mathbf{A} should obey the RIP such that the signal $\boldsymbol{\theta}$ does not lie in the null space of \mathbf{A} . This is equivalent to require that any S columns of \mathbf{A} should be almost orthogonal to each other.

1.4 Compressive Imaging

Natural images usually contain a large amount of redundant information: spatial redundancy, color redundancy, as well as inter-frame redundancy. These redundant information enables a number of image and video compression algorithms [9,10], that allow images and videos to be efficiently stored, transmitted and displayed. However, in conventional imaging pipelines, pixel-wise information of images are required before image compression taking place. This causes a large waste of resources such as the number of sensors, as well as the power and buffer requirement of cameras. Compressive sensing has thus been applied in the imaging application to overcome the above drawbacks. Compressive imaging aims at performing efficient image sampling. It usually employs additional optical modulation elements in the imaging system and involves the demodulation process after sensor measurement to recover the desired image information. An efficient sampling usually benefits the image signal acquisition speed and reduces the hardware requirements to capture high resolution or high dimensional images. This section serves as a brief review on some of the start-of-art compressive imaging architectures.

1.4.1 Single-pixel Camera

Ten years ago, researchers in Rice University proposed a novel 2D imaging system [11]: Instead of using a conventional sensor array, only a single photon detector is used to collect compressed measurements for 2D image recovery. The key coding element is a digital micro-mirror device (DMD). A DMD is an electronic device that contains an array of micro-mirrors and its control circuits. The control unit is capable of flipping each micro-mirror in two different angles, normally -12° and 12° , in hundreds or even thousands of Hz. Placed on the focal plane of the objective lens, a DMD serves as a 2D binary spatial modulation device that is capable of fast alternating the coding patterns. A lens condenser collects and integrates the spatial modulated image signal into a single sensor. A 2D image is then recovered from a time series of sensor collections by employing the sparsity constrain.

Three main advantages exist in this single-pixel camera system: 1. It reduces the sensor size requirement of a conventional 2D camera. The image recovery resolution is instead determined by the DMD. The drawbacks of a 2D sensor array such as low quantum efficiency, buffer and bandwidth limitation and sensor cross-talk can be largely overcome. 2. The low light sensing capability. This is not only because a single detector has more quantum efficiency than a sensor array, but also due to the fact that the sensor measurement is a collection of light from the whole field of view. 3. The use of a point detector provides very flexible sensing capability. Many of the existing compressive imaging systems are indeed the conversions of this architecture. One example is the Compressive Raman spectral imaging system proposed in [12], where the single sensor is replaced by a Raman spectroscopy. With the additional spectral filter, mirrors and laser illumination, Raman imaging is achieved without scanning the scene. Another impressive conversion is the development of compressive LiDAR [13,14], where a photon counting detector is instead applied with an additional modulated laser source. Recently the compressive LiDAR systems draw attention to automotive industry for the potentiality in the advanced driver-assistance systems (ADAS).

1.4.2 Compressive Spectral Imaging

During the same time, a coded aperture compressive spectral imaging (CASSI) system was proposed aiming at achieving real-time multi-spectral imaging capability [15]. Different from the single-pixel camera, this imaging system applies a much simpler and cheaper spatial modulation solution: a two-dimensional block-unblock photo-mask named coded aperture. This fixed-patterned coded aperture is placed on the focal plane of the objective lens, followed by a relay system and a dispersive element. The dispersive element can be either a grating or a prism, results in an image cube shearing along the spectrum dimension. A monochrome sensor array then integrate the coded and sheared spectral bands into a single focal plane array (FPA) measurement. Spectral image bands are then recovered from this single snapshot measurement via compressive sensing reconstruction algorithms.

This imaging system has the advantage in the real-time spectral imaging capability, overcoming the conventional scanning or resolution reduction drawbacks. But it suffers from low reconstruction image quality and low spectrum recovery accuracy. Since then, several CASSI-based spectral imaging systems have been proposed aiming at achieving largely improved reconstruction performance [16]. This includes the construction of a DMD-based CASSI [17]. Through replacing the static coded aperture into a DMD, the imaging system is capable of alternating its coding pattern during different snapshot measurement of the same scene. This enables the multi-snapshot spectral imaging system that largely improves the ill-condition measurement matrix. Moreover, a more precise spectrum dispersion model named high-order CASSI [18] was developed, where the continuous spectrum shearing as well as the non-linearity of dispersion is accounted. Followed are the proposal and optimization of a colored coded aperture CASSI [19,20], a simplified color-sensor spectral imaging system [21], spatial and spectrum super-resolution approaches [22,23], as well as side-information CASSI [24]. Another state-of-art compressive spectral imaging system is a spatial-spectral coded compressive spectral imaging system [25], where the coding mask is placed between an imaging plane and a Fourier plane to achieve simultaneous spatial-spectral

modulation.

The above mentioned compressive imaging systems all apply dispersive elements for spectrum modulation. The shearing blur caused by the dispersive element is a key factor that limits the experimental reconstruction quality. There are some other optical elements that provide different spectrum modulation patterns instead of spectrum dispersion. A circular variable filter (CVF) [26] can be an alternative which provides continuous and different spectrum modulation along the angular position of the filter. The CVF does not require additional attention to the precise dispersion modeling. Instead, a spinning or rotation is beneficial to vary the spectrum modulation across the scene.

In this dissertation, a novel compressive spectral imaging system based on a CVF and a novel polar coded aperture is proposed, optimized and experimentally implemented. The polar shaped coded aperture and the CVF are placed on the focal plane of the objective lens to provide a spatial-spectral modulation to the scene. A low resolution monochrome sensor is applied to collect the compressed measurements. The system was initially proposed for munition guidance purposes. When mounted on a spinning munition, this imager continuously changes its spatial and spectral coding and captures a number of measurement shots during a 2π period. Spectral image reconstruction is then performed with these compressive coded low resolution measurements. In the dissertation, a detailed design and optimization of the polar coded aperture is described. Two mathematical models are developed aiming at finding the precise system matrix. Computer simulations as well as proof-of-concept experiments are conducted as an evaluation of the system performance.

1.4.3 Compressive Spectral Polarization Imaging

Compressive spectral polarization imaging aims at capturing a 4D image cube efficiently. Based on the number of Stokes parameter recovered, the 4D image cube can be organized as two to four 3D spectral image cubes. The most straightforward approach involves rotating a linear polarizer in a compressive spectral imaging system

[27]. However the rotation of a linear polarizer is actually scanning the polarization space. For more efficient sensing, polarization scanning needs to be avoided through the use of additional optical modulation elements. One optical element that provides both spectral and polarization modulation can be a birefringent prism. Light with different wavelengths and polarization states are projected into different propagation directions after passing through a birefringent prism. Based on this, a snapshot spectral polarization imaging system is proposed through the use of a coded aperture, two birefringent prisms, a set of lenses and a monochrome sensor array [28]. This single snapshot system achieves real-time spectral polarization imaging with the application of compressive sensing theory. However, it can only resolve the first two Stokes parameters: an irradiance term \mathbf{S}_0 and a polarization difference term \mathbf{S}_1 . Another state-of-art compressive spectral polarization imaging system applies an expensive spatial light modulator for spatial coding. The system also involves the use of a linear polarizer, a beam-splitter and a retarder to achieve polarization modulation [29]. This system captures the first three Stokes parameters. However, the spectrum is only limited to RGB bands. Moreover, the use of a collimating lens and the beam-splitter tremendously increases the complexity of the hardware. This encourages the development of a spectral polarization imaging system that is capable of capturing multi-spectral Stokes image planes with a simple optical layout.

In this dissertation, a novel compressive spectral polarization imaging system is developed and implemented. Inspired by the division of focal-plane array methods, a micro-polarizer array (MPA) is used for polarization modulation. The MPA, also named pixelated polarizer, is an array of micro-polarizers. It provides pixel-wise polarization modulation to the scene. For each Stokes image plane, the MPA acts as a block-unblock spatial coding, which is an ideal replacement of the coded aperture and the expensive spatial light modulator. In the proposed system, this MPA is integrated into a color sensor array. A dispersive element, such as an Amici prism, is placed in front of the integrated sensor to provide spectral modulation. The optical layout of this system is extremely simple: an objective lens, an Amici prism and a polarization

integrated color sensor. This system is capable of capturing first Stokes image planes across multiple spectral channels. With a careful design of the micro-polarizer distribution, a single snapshot measurement provides decent spectral polarization image reconstruction. The system is also flexible to capture multi-snapshots for an improved reconstruction through prism rotation. This dissertation describes the mathematical model of the system, the design of the micro-polarizer distribution, computer simulations as well as experimental implementations.

1.4.4 Other Compressive Sensing Applications In Imaging Systems

The application of compressive sensing is not limited to the above domains. For example, in medical imaging, research on compressive MRI can be dated back from 2007 [30]. Through a random sparse sampling on the Fourier domain, MRI images can be captured in a much faster manner compared with traditional scanning MRI. Another example of applying compressive sensing in medical imaging system is the coded aperture x-ray computed tomography approaches [31]. By randomly blocking x-ray sources and collecting the integrated measurements, compressive x-ray computed tomography has a much lower x-ray radiation requirement to accomplish 3D reconstruction.

In the domain of computational photography, a research group in MIT proposed a compressive light field camera [32], where a coded photo-mask is placed slightly in front of the sensor. This allows the modulation and capture of different light field with a simple modification of traditional camera. For video recording, compressive sensing takes advantage of large redundancy among video frames. Through a fast coded aperture movement or the implementation of a DMD, temporal super-resolution can be easily achieved through a conventional camera with a much lower frame-rate [33].

For high-dimensional imaging, compressive sensing also benefits the joint acquisition of spectral and 3D imaging, as well as the realization of high frame-rate spectral video. I'm lucky to be involved in the development of a 3D compressive spectral integral imaging system [34], a compressive spectral + ToF imaging system [35] and a

compressive spectral temporal imaging system. All the three are unfortunately out of the scope of this dissertation.

1.5 Dissertation Format

This dissertation contains five chapters. The first chapter clarifies some concepts in the area of spectral imaging, spectral polarization imaging and compressive sensing. A brief review of conventional and state-of-art spectral imaging and spectral polarization imaging systems is also included. Chapter two describes the optical design, mathematical modeling and computer simulations on a polar coded aperture compressive spectral imaging system. Chapter three further develops the polar coded aperture optimization algorithms as well as the experimental implementations. Chapter four presents a compressive spectral polarization imaging system based on a pixelated polarizer. Mathematical modeling, computer simulations, coding pattern design as well as optical experiments are all included.

1.6 Original Contributions

My work contributes in the development of compressive spectral imaging and compressive spectral polarization imaging systems in the following aspects:

1. I contributed in the structure design and optimization of a polar coded aperture for compressive sensing purposes.
2. Developed and mathematical modeled the proposed polar coded aperture spectral imaging system.
3. Modeled the continuous rotation motion of the spinning imager to reduce the reconstruction rotation blur.
4. Simulated the polar coded aperture spectral imager in computer programs with different parameter settings in different noise levels.
5. Performed the polar aperture coding optimization.
6. Conducted the experimental implementation of the polar coded aperture spectral imaging system.
7. Contributed in the optical layout design of the compressive spectral polarization imaging system.

8. Developed the mathematical model and reconstruction strategy for directly reconstructing Stokes images without the recovery of intensity images.
9. Contributed in the design of micro-polarizer patterns for better reconstruction quality.
10. Performed computer simulations and image reconstruction on the compressive spectral polarization imaging system.
11. Conducted the experimental implementation of the compressive spectral polarization imaging system.

1.7 Journal and Conference Publications

Below I list the journal and conference publications as a result of my Ph.D. research:

Journal publications:

1. **C. Fu**, M. Don, G. R. Arce, “Optimization and Experimental Demonstration of a Compressive Polar Coded Aperture Spectral Imager”, submitted to IEEE Trans. on Computational Imaging, 2018.
2. H. Rueda, **C. Fu**, D. L. Lau, G. R. Arce “Spectral-ToF Compressive Snapshot Camera: Towards Hyperspectral+Depth Imagery”, IEEE Journal of Selected Topics in Signal Processing, vol. **11**, no. 7, 992-1003, 2017.
3. **C. Fu**, M. Don, G. R. Arce, “Compressive Spectral Imaging via Polar Coded Aperture”, IEEE Trans. on Computational Imaging, vol. **3**, no. 3: 408-420, 2017.
4. M. L. Don, **C. Fu**, G. R. Arce, “Compressive imaging via a rotating coded aperture,” Appl. Opt. **56**, B142-B153, 2017.
5. W. Feng, H. F. Rueda, **C. Fu**, G. R. Arce, W. He, Q. Chen, “3D compressive spectral integral imaging”, Opt. Express **24**, 24859-24871, 2016.
6. **C. Fu**, H. Arguello, B. M. Sadler, G. R. Arce, “Compressive Spectral Polarization Imaging By Pixelized Polarizer And Colored Patterned Detector”, J. Opt. Soc. Am. A **32**, 2178-2188, 2015.

Conference publications:

1. W. Feng, H. Rueda, **C. Fu**, Q. Chen and G. R. Arce, “Compressive spectral integral imaging using a microlens array”, Proc. SPIE 9857, Compressive Sensing V, 985706, May, 2016.

2. **C. Fu**, H. Arguello, B. M. Sadler, G. R. Arce, “Compressive spectral polarization imaging with coded micropolarizer array”, Proc. SPIE 9484, Compressive Sensing IV, 948409, May, 2015.
3. **C. Fu**, H. Arguello, G. R. Arce, Virginia O. Lorenz, “Compressive spectral polarization imaging”, Proc. SPIE 9109, Compressive Sensing III, 91090D, May, 2014.

Chapter 2

COMPRESSIVE SPECTRAL IMAGING VIA A POLAR CODED APERTURE

In this chapter, a compressive spectral imager based on a polar coded aperture and a continuous variable circular bandpass filter is proposed for spinning munitions. As the imager rotates with the munition, compressive projections are sequentially captured with embedded spatial and spectral modulation. The polar coded aperture design is introduced, aiming at optimizing the sensing process. Both discrete and continuous rotation models of the proposed imager are derived and used to characterize the compressive imager. Computer simulations validate the computational models and the reconstruction algorithm.

2.1 Introduction and Related Research Work

Imaging techniques have been introduced in guided munitions to perform precise target detection and pinpoint strike capabilities. They have many advantages over global positioning system (GPS) driven systems, such as jamming immunity and greater accuracy as demonstrated in many unmanned aerial vehicle (UAV) platforms [39-40]. Typically, monochromatic imaging is used in these applications. Spectral imaging, however, is capable of increasing the precision in target detection and munition guidance by providing additional spectral information of the scene [41,42]. Spectral imaging architectures usually involve moving filters or the application of expensive color patterned imaging sensor arrays [43] to achieve spectral modulation. The spinning nature of munitions provides an approach to modulate the spectrum via a circular variable filter (CVF) without the need for moving parts. A CVF is a bandpass filter whose center wavelength continuously varies with its angular position and has a history

of being used in spectrometers, monochrometers, and spectral imagers [44-50]. When mounted on a spinning munition, the CVF provides a continuous spectral modulation of the target.

In addition to spectral modulation, the munition's spin can also be leveraged to increase the spatial resolution of the imager using compressive sensing (CS) theory. In CS, a compressive sample is normally acquired by applying a binary code in the spatial domain. Besides increased resolution, compressive imaging can provide faster measurement acquisition, easy data storage and transmission, as well as reduced system noise. Thus, a new compressive spectral imager is proposed for spinning munitions that combines a CVF with a coded aperture.

Our design has three advantages over existing coded aperture compressive imaging system design. First, in traditional coded aperture compressive imaging, a square shaped coded photomask was initially used to provide spatial coding for a single snapshot. To capture additional snapshots, elaborate mechanisms are typically employed to apply multiple codes, such as using a digital micro-mirror device (DMD) or by shifting an aperture code with a piezoelectric actuator. These complex, expensive architectures are not suited to munitions, however, which require a simple, inexpensive imager. Our design solves this problem by using a polar shaped coded mask together with the munition's natural spin to obtain multiple snapshots without any moving parts or complex devices. Secondly, although spatial super-resolution methods have been proposed, traditional coded aperture compressive spectral imagers usually employ coded apertures the same size as the focal plane array (FPA) sensors, thus limiting the resolution of the spectral image to that of the FPA. However, this is unnecessary since the reconstructed spatial resolution is only determined by the resolution of the coded aperture. Instead, a low resolution FPA is applied here with less expense on munition applications. Sufficient measurements are captured through the imager rotation with a high-resolution coded aperture. Third, in traditional compressive spectral imagers, one or more dispersive elements are typically applied to produce spectral separation. However, the non-linear spectral dispersion makes the spectrum sampling non-uniform.

A high-order model is needed to characterize the dispersion, increasing the complexity of modeling and calibration. Our design solves this problem by using a CVF, which has a linear spectral modulation. Combined with the polar coded aperture, the CVF is placed on the focal plane of the objective lens, making our imager more compact than other existing coded aperture compressive spectral imagers.

Challenges exist when developing the coded aperture design. The spatial coding provided by conventional square shaped coded apertures requires complex rotation transformations. Additionally, the coded aperture provides less modulation towards its center, resulting in an inefficient sensing strategy. Different from traditional square coded apertures in compressive imaging, we propose a polar coded aperture with a spokes-rings structure to solve the above problems. The rotation motion is transformed into a simple circular shifting of image pixels which provides uniform modulation.

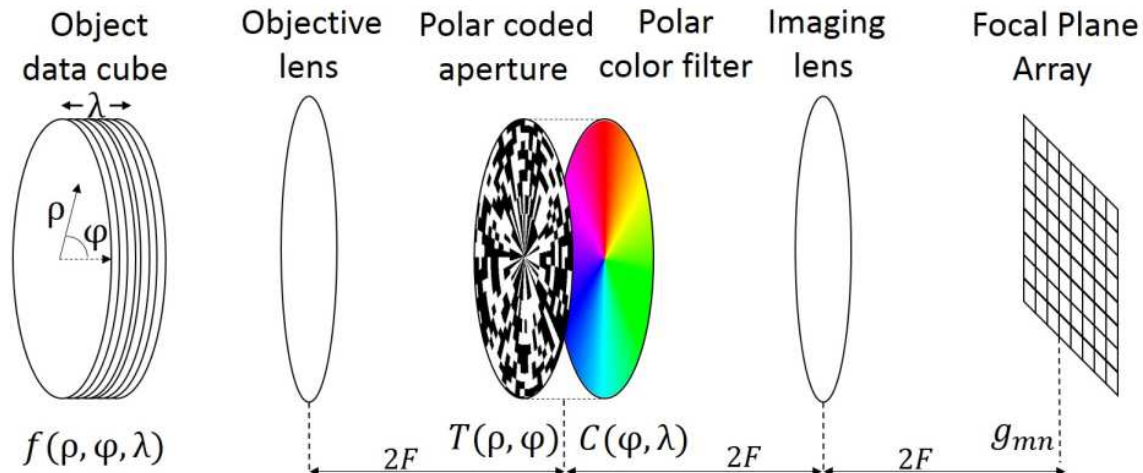


Figure 2.1: Compressive spectral imaging architecture with a polar coded aperture and a continuous viable circular bandpass filter. Compressed projections are captured on the FPA detector.

Figure 1 shows the proposed imaging architecture which consists of an objective lens, a polar coded aperture, a CVF, a relay lens and a focal plane array (FPA) detector. The polar coded aperture, combined with the continuous circular variable bandpass filter, is placed in the image focal plane of the objective lens, providing the spatial and spectral modulation to the scene. As the munition spins, the imager conducts a continuous rotation. In general, the imager can also be mounted on other

spinning equipment, or simply on an electronic controlled rotating platform to perform compressive spectral imaging.

For guided munitions, the motion of the imager can be described in multiple dimensions. The translation motion should be precisely acquired for characterizing the compressive sensing reconstruction. In this research, only a two-dimensional rotation is considered for simplicity, with the rotation speed assumed to be constant and known a priori. For further research, the robustness of the system should also be evaluated by calculating the tolerance of the rotation modelling error.

The main contributions of this chapter are addressed in three aspects: First, a novel method of changing spatial coding for compressive imaging is developed by the rotation of a polar coded aperture. The geometry design of the polar aperture is presented to optimize the image quality. Second, the CVF is introduced into compressive spectral imaging. To our knowledge, this is the first time a CVF is applied to compressive coded aperture imaging. The influence of CVF bandwidth to the reconstruction quality is analyzed. Finally, both the discrete and continuous rotation forward models are developed with the corresponding computer simulation results presented.

2.2 Polar Coded Aperture Compressive Spectral Imaging System

Generally compressive imaging systems collect the sensor measurement \mathbf{g} through a measurement matrix \mathbf{H} . \mathbf{H} is directly determined by the optical layout and optical modulation patterns. A good knowledge of the measurement matrix \mathbf{H} is critical to an accurate reconstruction. Thus in this section, a detailed mathematical modeling is presented.

2.2.1 Discrete Imager Rotation Sensing Model

The proposed compressive imaging architecture is displayed in Figure 2.1. A polar coded aperture combined with a continuous variable circular bandpass filter is applied at the image focal plane to provide spatial and spectral compressive coding. The polar coded aperture is designed to have a ring-spoke structure as shown in Fig. 2.2.

The aperture consists R_{in} inner rings and R_{out} outer rings. The outer rings are designed to have a denser distribution of spokes than the inner rings. S_{in} and S_{out} are denoted as the numbers of spokes in the inner and outer rings, respectively. The design of the aperture geometry is further introduced in Section III.

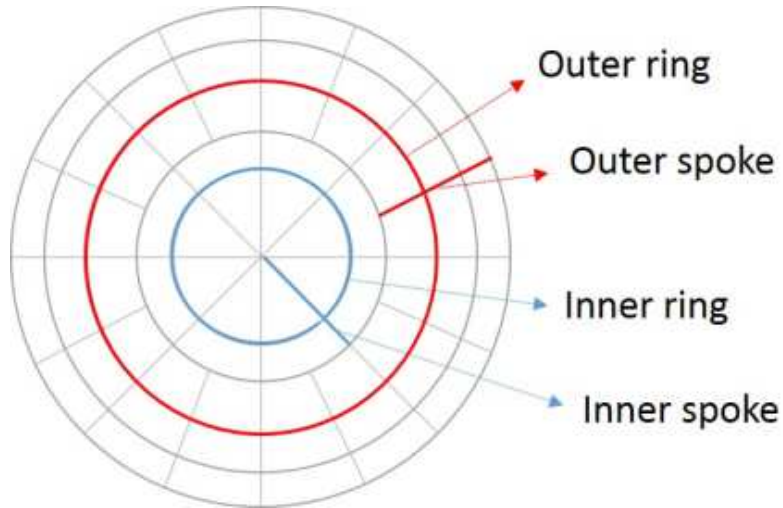


Figure 2.2: Geometry illustration of the proposed polar coded aperture. The number of spokes in outer rings is twice of the spokes in inner rings.

Compressed FPA projections of the coded data cube are captured as the imager rotates. If the image rotations are generated by electronic devices, the rotation can be controlled to have discrete angle increments, where the imager remains fixed during one snapshot measurement. When the imager is mounted on a spinning munition, continuous rotation motion occurs when measurements are captured. However, if the shutter time τ_s of the camera is much smaller than the rotation period of the imager τ_r , $\tau_s \ll \tau_r$, the imager can be assumed to be static during each snapshot. With this assumption, a discrete approximation model of the imager rotation is described next. In Section V, a continuous rotation model is further developed.

Denote the scene as a 3D data cube $f(\varphi, \rho, \lambda)$, where φ and ρ are the spatial polar coordinates, and λ is the spectral wavelength. The polar coded aperture is represented as $T(\varphi, \rho)$, while the continuous variable circular bandpass filter is modeled as $C(\varphi, \lambda)$. The center wavelengths of the polar bandpass filter continuously change

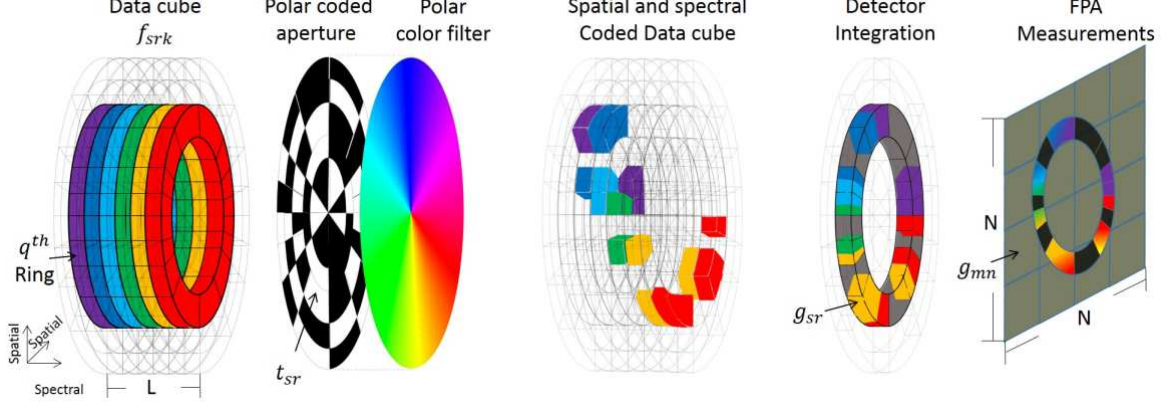


Figure 2.3: Discretized compressive sensing phenomenon of polar imager. The q^{th} ring of the data cube f_{srk} is coded by the polar coded aperture and modulated by the continuous variable circular bandpass filter. The modulated light is integrated in both spatial and spectral domains, captured by the FPA sensors.

in the range of $[\lambda_{min}, \lambda_{max}]$ with φ increasing from 0 to 2π . The bandwidth of the bandpass filter is denoted as b_w for all φ . Thus the transmitted wavelength range of the continuous variable circular bandpass filter is $[\lambda_{min} - b_w/2, \lambda_{max} + b_w/2]$. The polar coordinates representation of the FPA projection is written as:

$$g_p(\varphi, \rho) = T(\varphi, \rho) \int_{\lambda_{min} - b_w/2}^{\lambda_{max} + b_w/2} C(\varphi, \lambda) f(\varphi, \rho, \lambda) d\lambda. \quad (2.1)$$

The physical phenomenon of this compressive sensing procedure is shown in Figure 2.3, where the discrete form of the binary polar coded aperture is written as

$$t_{sr} = \int_{r\Delta_\rho(r)}^{(r+1)\Delta_\rho(r)} \int_{s\Delta_\varphi(r)}^{(s+1)\Delta_\varphi(r)} T(\varphi, \rho) \rho d\varphi d\rho, \quad (2.2)$$

where s and r index the spokes and rings in the polar coded aperture, respectively. $\Delta_\varphi(r)$ is the pitch of spokes in r^{th} ring, while $\Delta_\rho(r)$ represents the pitch of the r^{th} ring. Denote the integration region of the $(s, r)^{\text{th}}$ polar pixel as Ω_{sr} , then the binary polar coded aperture is rewritten as

$$t_{sr} = \iint_{\Omega_{sr}} T(\varphi, \rho) \rho d\varphi d\rho. \quad (2.3)$$

The discrete representation of the 3D data cube is written as

$$f_{srk} = \int_{\lambda_k}^{\lambda_{k+1}} \iint_{\Omega_{sr}} f(\varphi, \rho, \lambda) \rho d\varphi d\rho d\lambda. \quad (2.4)$$

Similarly, the discrete form of the continuous variable circular bandpass filter is represented as

$$c_{srk} = \int_{\lambda_k}^{\lambda_{k+1}} \iint_{\Omega_{sr}} C(\varphi, \lambda) \rho d\varphi d\rho d\lambda. \quad (2.5)$$

The physical phenomenon of this discrete spectral modulation is illustrated in Figure 2.4. The modulation amplitude c_{srk} is determined by the center wavelengths and the bandwidth of the bandpass filter. The impact of the bandpass filter bandwidth is further discussed in Section IV.

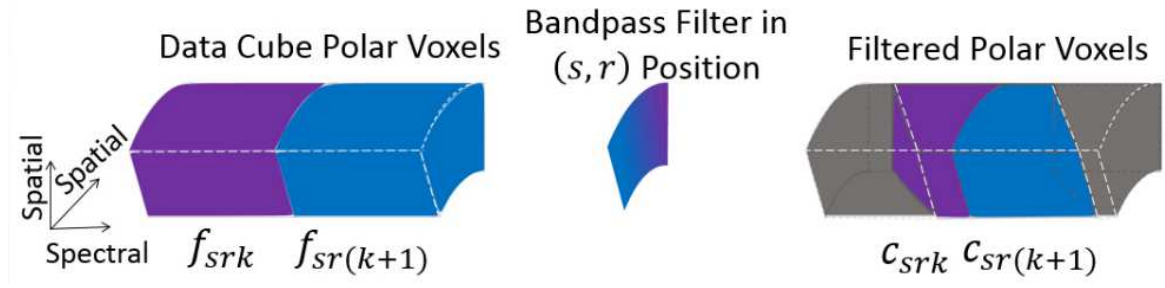


Figure 2.4: Illustration of the spectral modulation of the filtered polar data cube. Two spectrally adjacent polar data cube voxels are modulated in spectrum as passing through a continuous variable circular bandpass filter pixel.

The continuous change of the center wavelength with the change of the angular position in the circular bandpass filter enables the division of the spectral channels. The spectrum is uniformly divided into L bands from $\lambda_{min} - b_w/2$ to $\lambda_{max} + b_w/2$, where as defined above, $[\lambda_{min}, \lambda_{max}]$ is the center wavelength range of the bandpass filter, and b_w is the filter bandwidth. The spatial and spectral modulated polar data cube is integrated in the spectral domain. The discrete form of this polar projection is

$$\begin{aligned} g_{sr} &= \iint_{\Omega_{sr}} T(\varphi, \rho) \int C(\varphi, \lambda) f(\varphi, \rho, \lambda) d\lambda \rho d\rho d\varphi \\ &= \sum_k \iint_{\Omega_{sr}} T(\varphi, \rho) \int_{\lambda_k}^{\lambda_{k+1}} C(\varphi, \lambda) f(\varphi, \rho, \lambda) \rho d\lambda d\rho d\varphi \\ &= \sum_k t_{sr} c_{srk} f_{srk}. \end{aligned} \quad (2.6)$$

Denote the vector form of the data cube and the integrated coded scene as \mathbf{f} and \mathbf{g}_1 , respectively. This sensing process in the ℓ^{th} snapshot can be written in matrix form as

$$\mathbf{g}_1^\ell = \mathbf{P}^\ell \mathbf{f}, \quad (2.7)$$

where \mathbf{P}^ℓ represents the effect of the polar coded aperture and the continuous variable circular bandpass filter. The vector form of the bandpass filter modulation in k^{th} spectral channel is represented as

$$\mathbf{c}_k^\ell = [c_{11k}^\ell, c_{21k}^\ell, \dots, c_{12k}^\ell, \dots, c_{S_{out}Rk}^\ell]^T. \quad (2.8)$$

Similarly, the vector form of the polar coded aperture in the ℓ^{th} snapshot is given by

$$\mathbf{t}^\ell = [t_{11}^\ell, t_{21}^\ell, \dots, t_{12}^\ell, \dots, t_{S_{out}R}^\ell]^T. \quad (2.9)$$

Then the coding matrix \mathbf{P}^ℓ is written as

$$\mathbf{P}^\ell = [\text{diag}(\mathbf{t}^\ell \circ \mathbf{c}_1^\ell), \text{diag}(\mathbf{t}^\ell \circ \mathbf{c}_2^\ell), \dots, \text{diag}(\mathbf{t}^\ell \circ \mathbf{c}_L^\ell)], \quad (2.10)$$

where $\mathbf{t}^\ell \circ \mathbf{c}_k^\ell$ is the element-wise product of \mathbf{t}^ℓ and \mathbf{c}_k^ℓ . Denote the total number of polar pixels in the coded aperture as $V = R_{in}S_{in} + R_{out}S_{out}$. Then \mathbf{P}^ℓ has the dimensions of $V \times VL$. In order to visualize \mathbf{P}^ℓ , a test data cube with 2 inner rings ($R_{in} = 2$), 8 inner spokes ($S_{in} = 8$), 1 outer rings ($R_{out} = 1$), 16 outer spokes ($S_{out} = 16$), and 2 spectral channels ($L = 2$) is applied. The corresponding \mathbf{P}^ℓ generated via Eq. (2.12) is displayed in Figure 2.5. The gray scale values are between 0 and 1. 80% unblocked pixels are randomly distributed in the polar coded aperture for better demonstration of the CVF modulation \mathbf{c}_k^ℓ in \mathbf{P}^ℓ . Each spectral band is organized from inner to outer rings, with the spokes in each ring arranged from angles 0 to 2π . In this two band example, the CVF acts as a low pass filter for the first spectral band, and a high pass filter for the second spectral band. This can be observed by the spoke values of the first spectral band falling off from 1 to 0, while the spoke values in the second spectral band increase from 0 to 1.

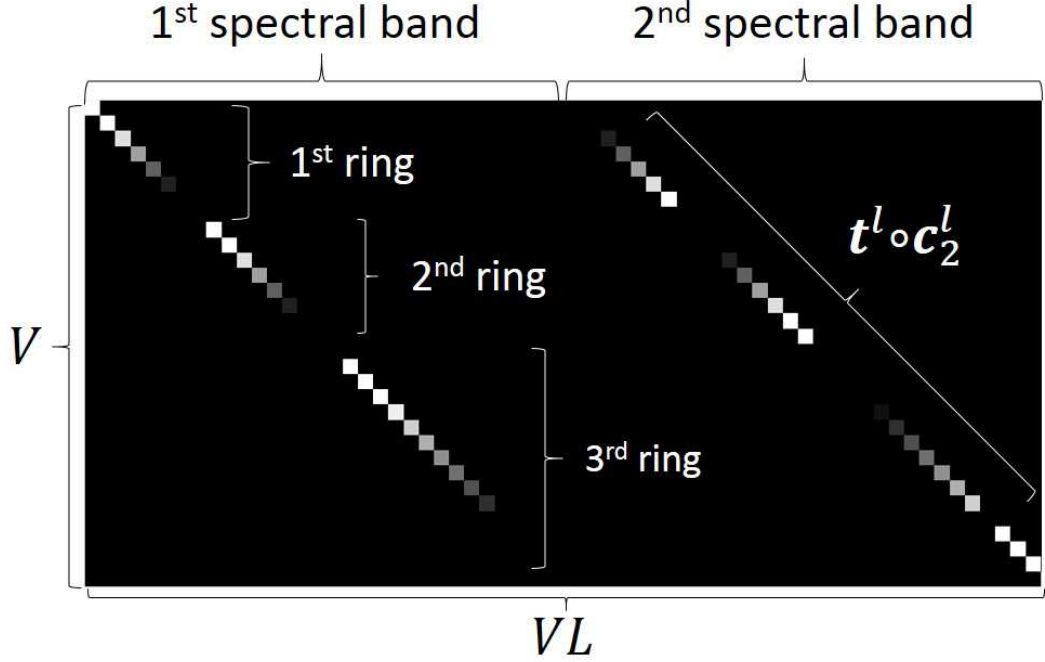


Figure 2.5: Coding matrix \mathbf{P}^ℓ for $S_{in} = 8$, $S_{out} = 16$, $R_{in} = 2$, $R_{out} = 1$, $L = 2$ data cube. The entries represent the spatial and spectral modulation factors on the polar data voxels, with 0 entries remaining black.

2.2.2 Discussion on the Spectral Resolution

As displayed in the \mathbf{P}^ℓ image, distinct spectral modulation \mathbf{c}_k^ℓ for each band k enables the separation of the spectral bands. One spectral band k can always be separated into two or more sub-bands k_i when the spectral modulations $\mathbf{c}_{k_i}^\ell$ are different. It is thus possible to separate a band into two sub-bands with distinct spectral coding. Thus, an infinite number of spectral bands could be recovered in principle. As shown in Figure 2.6, the region $\mathbf{R}_k^\ell = \{(s, r) | c_{srk}^\ell \neq 0\}$ is the spatial area where the k^{th} spectral band is sensed by the continuous variable filter. Assume this spectral band is uniformly divided into two sub-bands k_1 and k_2 . Thus, denote $\mathbf{R}_{k_1}^\ell = \{(s, r) | c_{srk_1}^\ell \neq 0\}$ and $\mathbf{R}_{k_2}^\ell = \{(s, r) | c_{srk_2}^\ell \neq 0\}$. Since the bandpass wavelengths differ for different angular positions in the spatial domain, $\mathbf{R}_{k_1}^\ell \neq \mathbf{R}_{k_2}^\ell$ when the number of spectral bands $L \leq S_{out}$. Then, there exists a polar pixel (s_1, r_1) , such that $(s_1, r_1) \in \mathbf{R}_{k_1}^\ell$ and $(s_1, r_1) \notin \mathbf{R}_{k_2}^\ell$. Similarly,

another polar pixel (s_2, r_2) exists, such that $(s_2, r_2) \in \mathbf{R}_{k_2}^\ell$ and $(s_2, r_2) \notin \mathbf{R}_{k_1}^\ell$. Therefore, the following equations hold,

$$\begin{cases} c_{s_1 r_1 k_1}^\ell \neq 0 \\ c_{s_1 r_1 k_2}^\ell = 0 \end{cases} \quad \text{and} \quad \begin{cases} c_{s_2 r_2 k_1}^\ell = 0 \\ c_{s_2 r_2 k_2}^\ell \neq 0 \end{cases}, \quad (2.11)$$

resulting in $\mathbf{c}_{k_1}^\ell \neq \mathbf{c}_{k_2}^\ell$. Thus, the two sub-bands k_1 and k_2 are separated.

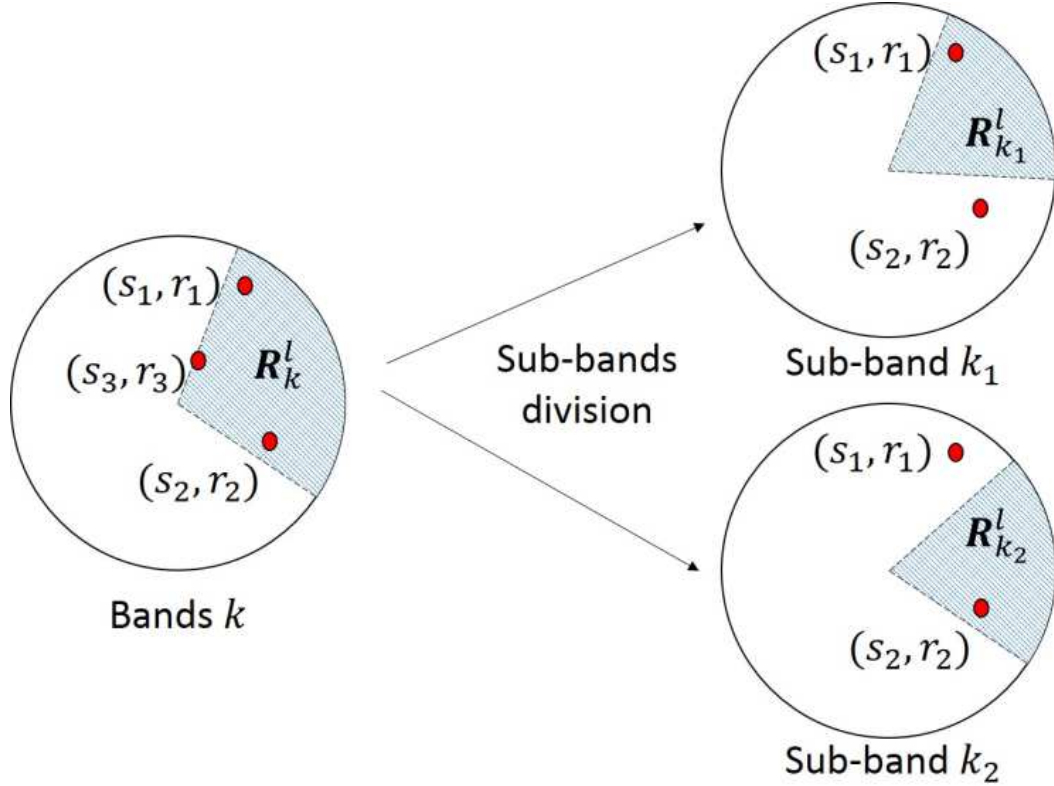


Figure 2.6: The polar pixels in k^{th} spectral band that can be sensed by the continuous variable filter are concentrated in the region of \mathbf{R}_k^ℓ . This spectral band is split into two sub-bands where the sensed polar pixels are concentrated in two smaller regions $\mathbf{R}_{k_1}^\ell$ and $\mathbf{R}_{k_2}^\ell$.

In the situations that $L > S_{out}$, $\mathbf{R}_{k_1}^\ell = \mathbf{R}_{k_2}^\ell = \mathbf{R}_k^\ell$. For any polar pixel (s_3, r_3) located in the edges of $\mathbf{R}_{k_1}^\ell$, $c_{s_3 r_3 k_1}^\ell \neq c_{s_3 r_3 k_2}^\ell$. Thus $\mathbf{c}_{k_1}^\ell \neq \mathbf{c}_{k_2}^\ell$. The two sub-bands k_1 and k_2 can still be distinguished by the imager.

However, notice from Figure 2.6 that in each single snapshot, amounts of elements in both $\mathbf{c}_{k_1}^\ell$ and $\mathbf{c}_{k_2}^\ell$ are 0, making it impossible to recover either k_1 or k_2 band in the corresponding spatial area. Thus, a number of imager rotations are needed to

modulate a certain spatial area with the whole spectrum of the bandpass filter. In consequence, an infinite number of spectral bands could be separated with unlimited number of shots, under the conditions that the bandpass filter ideally changes its center wavelength continuously along the angular positions.

In addition, as discussed in Section IV, a larger number of reconstructed spectral bands requires a narrower bandwidth of the bandpass filter to achieve the best recovery performance. In Section IV. D, a 11.6nm wide bandpass filter is applied for a successful reconstruction of 128 bands, where $L = 2S_{out}$. Narrower bandwidths are more difficult to manufacture. Moreover, the difficulties for the spectral modulation calibration process also increase with $L > S_{out}$. All these practical difficulties need to be considered for the real implementation of the proposed imager.

2.2.3 Sensing Model of the Rectangular FPA sensors

The FPA detector consists of N^2 rectangular sensors. Denote the Cartesian representation of the FPA projection as $g_c(x, y)$. Then $g_c(\rho \cos \varphi, \rho \sin \varphi) = g_p(\varphi, \rho)$. The discrete FPA pixel measurement is

$$g_{mn} = \int_{n\Delta_c}^{(n+1)\Delta_c} \int_{m\Delta_c}^{(m+1)\Delta_c} g_c(x, y) dx dy, \quad (2.12)$$

where Δ_c is the square FPA pixel pitch. Denote the integration region of $(m, n)^{th}$ pixel as D . Then the discrete FPA measurement is

$$\begin{aligned} g_{mn} &= \iint_{D_{mn}} g_c(x, y) dx dy \\ &= \iint_{D_{mn}} g_p(\varphi, \rho) \rho d\rho d\varphi. \end{aligned} \quad (2.13)$$

With the forward model expressed in Eq. (2.3) and Eq. (2.8), the FPA measurement is represented as

$$\begin{aligned}
g_{mn} &= \iint_{D_{mn}} T(\varphi, \rho) \int C(\varphi, \lambda) f(\varphi, \rho, \lambda) d\lambda \rho d\rho d\varphi \\
&= \sum_r \sum_s w_{sr mn} \int_{r\Delta_\rho(r)}^{(r+1)\Delta_\rho(r)} \int_{s\Delta_\varphi(r)}^{(s+1)\Delta_\varphi(r)} T(\varphi, \rho) \\
&\quad \int_{\lambda_{min}-b_w/2}^{\lambda_{max}+b_w/2} C(\varphi, \lambda) f(\varphi, \rho, \lambda) \rho d\lambda d\rho d\varphi \\
&= \sum_r \sum_s w_{sr mn} g_{sr},
\end{aligned} \tag{2.14}$$

where $w_{sr mn}$ is the proportion of the energy in the $(s, r)^{\text{th}}$ polar coded aperture pixel sensed by the $(m, n)^{\text{th}}$ FPA sensor, given by

$$w_{sr mn} = \iint_{D_{mn} \cap \Omega_{sr}} \rho d\rho d\varphi \left(\iint_{\Omega_{sr}} \rho d\rho d\varphi \right)^{-1}. \tag{2.15}$$

Denote the vector form of the ℓ^{th} shot measurements as \mathbf{g}^ℓ . Then this polar-rectangular transformation can be expressed in matrix form as

$$\mathbf{g}^\ell = \mathbf{W}^\ell \mathbf{g}_1^\ell, \tag{2.16}$$

where \mathbf{W}^ℓ has the dimensions of $N^2 \times V$. Then \mathbf{W}^ℓ accounts for the weights $w_{sr mn}$ of the polar coded aperture sensed on $N \times N$ FPA sensors. Thus, the $(i, j)^{\text{th}}$ entry of \mathbf{W}^ℓ is $W_{ij}^\ell = w_{pq uv}$, where $v = \lfloor \frac{i}{N} \rfloor$ indexes the number of FPA columns, and $u = i - vN$ counts the number of FPA rows; Similarly,

$$q = \begin{cases} \lfloor \frac{j}{S_{in}} \rfloor, & \text{if } j \leq S_{in} R_{in} \\ R_{in} + \lfloor \frac{j - S_{in} R_{in}}{S_{out}} \rfloor, & \text{otherwise} \end{cases} \tag{2.17}$$

indexes the polar coded aperture rings, and

$$p = \begin{cases} j - q S_{in}, & \text{if } j \leq S_{in} R_{in} \\ j - R_{in} S_{in} - (q - R_{in}) S_{out}, & \text{otherwise} \end{cases} \tag{2.18}$$

counts the spokes of the polar coded aperture.

In order to visualize \mathbf{W} , the same test data cube used in Figure 2.5 is applied here. The

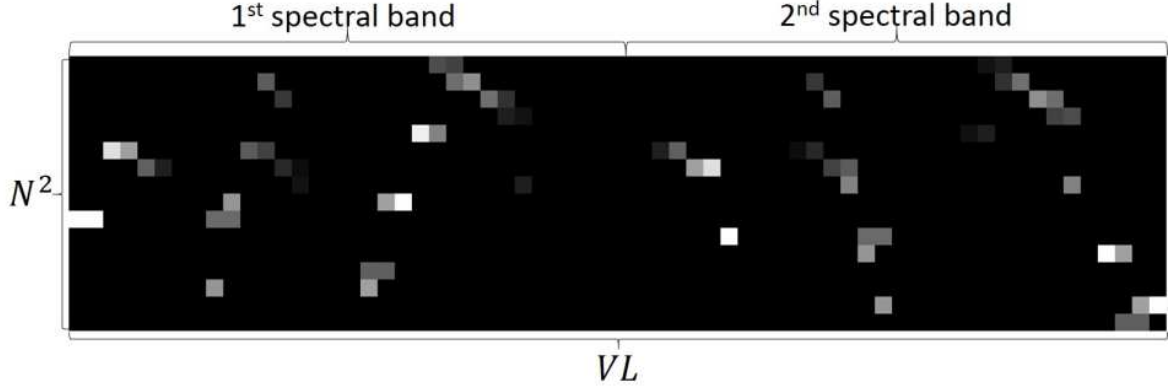


Figure 2.8: Sensing matrix \mathbf{H}^ℓ for a $S_{in} = 8$, $S_{out} = 16$, $R_{in} = 2$, $R_{out} = 1$, $L = 2$ data cube and an $N^2 = 4^2$ FPA.

Let K -snapshot measurements be represented in the form of a column vector $\mathbf{g} = [(\mathbf{g}^1)^T, (\mathbf{g}^2)^T, \dots, (\mathbf{g}^K)^T]^T$. Then the sensing procedure is written as $\mathbf{g} = \mathbf{H}\mathbf{f}$, where $\mathbf{H} = [(\mathbf{H}^1)^T, (\mathbf{H}^2)^T, \dots, (\mathbf{H}^K)^T]^T$. The relationship between the sensing procedures in different snapshots is further analyzed. The imager rotation motion enables multiple snapshots measurements embedded with different spatial and spectral coding. If the imager rotation exceed 2π , the patterns of polar coded aperture and the circular band-pass filter repeats themselves, resulting in duplicated measurements. Thus the number of snapshots is restricted to the coded aperture design. As will be shown in Section III, a good geometry design of the coded aperture has fewer spokes in the inner rings than the outer rings, i.e., $S_{in} < S_{out}$. Thus the maximum number of snapshots captured is limited by the number of spokes in the polar coded aperture inner rings, $K \leq S_{in}$.

Assume the polar coded aperture rotates d_r pixels in the r^{th} ring between adjacent snapshots acquired and assume K snapshots are taken within the rotation period τ_r , then, d_r is represented as

$$d_r = \left\lfloor \frac{S_r}{K} \right\rfloor, \quad (2.21)$$

where S_r is the number of spokes in r^{th} ring. As shown in Figure 2.9, the spatial coding provided by the coded aperture has a circular shift in its spokes between snapshots.

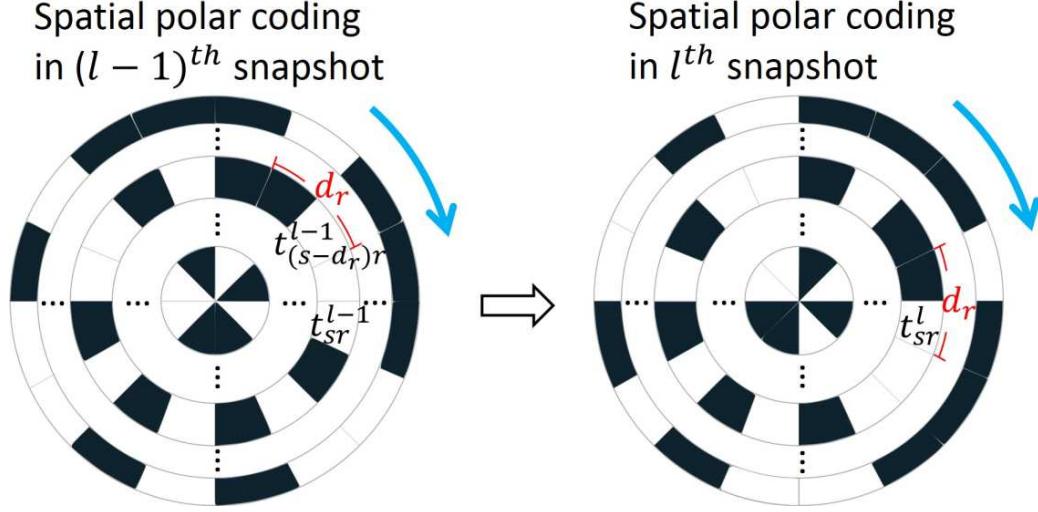


Figure 2.9: As the imager rotates, the spatial coding provided by the polar coded aperture is circularly shifting the spokes. The imager is assumed to be static when snapshots are captured, and d_r spokes are shifted between adjacent shots.

Then the current snapshot coded aperture can be obtained from the previous shot coded aperture as

$$t_{sr}^\ell = \begin{cases} t_{s-d_r, r}^{\ell-1}, & \text{if } r \leq d_r \\ t_{s+S_r-d_r, r}^{\ell-1}, & \text{otherwise.} \end{cases} \quad (2.22)$$

A permutation matrix \mathbf{M} can represent this circular shift procedure, with the ℓ^{th} shot coded aperture calculated as

$$\mathbf{t}^\ell = \mathbf{M}\mathbf{t}^{\ell-1}. \quad (2.23)$$

Similarly, the spectrum modulation of each spectral band performs the same spokes shift between snapshots. Thus the ℓ^{th} shot spectrum modulation is calculated as

$$\mathbf{c}_k^\ell = \mathbf{M}\mathbf{c}_k^{\ell-1}. \quad (2.24)$$

\mathbf{P}^ℓ can be constructed by applying Eq. (2.11). Notice that the columns of \mathbf{W}^ℓ are organized in the same fashion as the polar coded aperture structure, performing the same permutation procedure. Then the transformation of \mathbf{W}^ℓ between adjacent snapshots is modelled as

$$(\mathbf{W}^\ell)^T = \mathbf{M}(\mathbf{W}^{\ell-1})^T. \quad (2.25)$$

2.2.5 Spectral Data Cube Recovery

Since the polar coded aperture pixels share the same pixel size, the desired polar image band can be organized into rectangular matrix as shown in Fig 2.10. The inner-ring matrix with the dimension of $S_{in} \times R_{in}$ is the matrix formulation of the inner rings polar pixels. Similarly, the outer rings polar pixels are transformed into a $S_{out} \times R_{out}$ rectangular matrix.

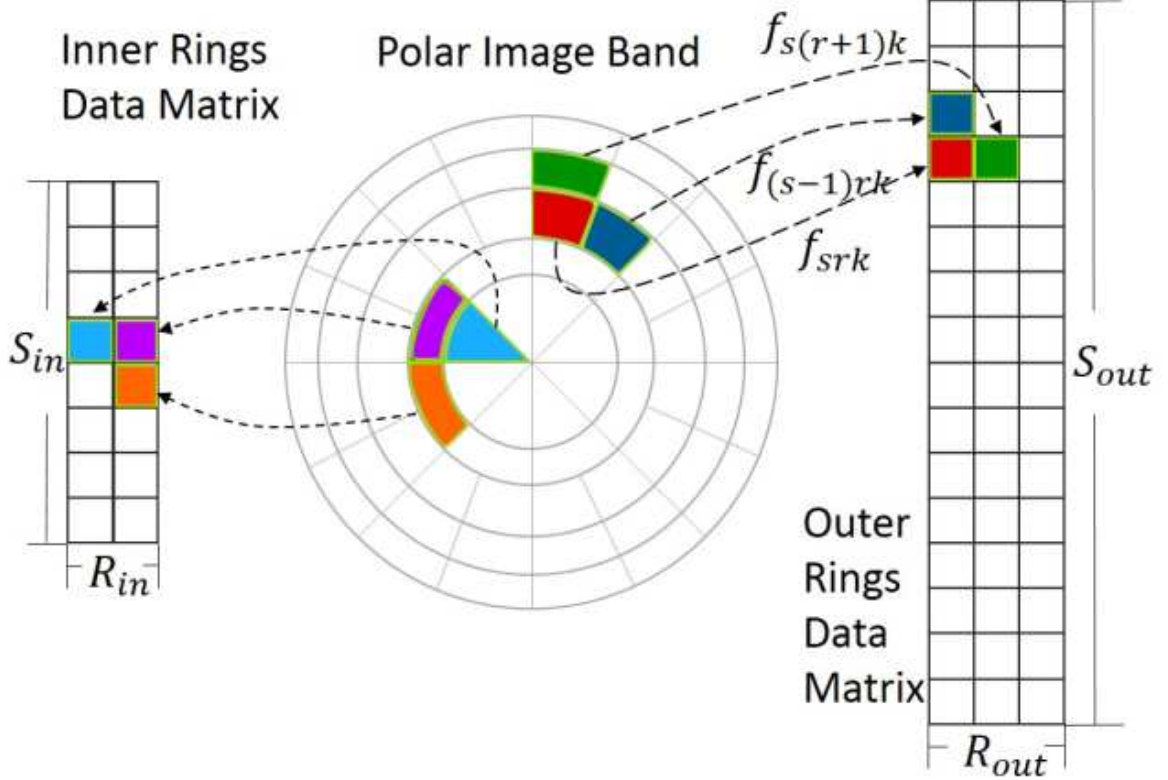


Figure 2.10: One polar image band is transformed into two rectangular matrices representing the inner and outer rings polar image pixels.

Then a Kronecker basis $\Psi = \Psi_1 \otimes \Psi_2 \otimes \Psi_3$ is applied to the matrix cubes, where $\Psi_1 \otimes \Psi_2$ provides the basis in the spatial domain and Ψ_3 is the basis in the spectral domain. Thus the polar data cube \mathbf{f} is represented as $\mathbf{f} = \Psi\theta$. In the simulation, we apply the Kronecker product of the 2D Wavelet in space and 1D discrete cosine transform (DCT) in spectrum as the basis [51], which has been shown as an efficient sparse basis in compressive spectral imaging. Instead of the DCT, other bases such as the Wavelet transform along the spectral axis could be applied [52-55]. A further

research could focus on optimizing the basis representation for polar spectral images. Then the sensing process can be expressed in Eq. (2.2). The signal reconstruction is then performed by solving the inverse problem of the under-determined linear system, where $\boldsymbol{\theta}$ is recovered to minimize a l_1 - l_2 cost function. This signal recovery problem is expressed as

$$\hat{\boldsymbol{\theta}} = \arg \min_{\boldsymbol{\theta}} \|\mathbf{g} - \mathbf{A}\boldsymbol{\theta}\|^2 + \lambda \|\boldsymbol{\theta}\|_1, \quad (2.26)$$

where λ is a regularization constant. In the simulation, the gradient projection for sparse reconstruction (GPSR) algorithm [56] is applied. In Matlab R2011b and a computer with the Intel(R) Core(TM) i7 CPU and 6.00GB RAM, the reconstruction algorithm takes approximate 447 seconds to recover a 16-band data cube with 128^2 spatial resolution in 600 iterations. Note the reconstruction speed can be significantly improved by performing code optimization, applying parallel computing or simply alternating the reconstruction algorithm.

2.3 Polar Coded Aperture Geometry Design

The polar coded aperture rotates together with the proposed imaging system, providing a set of block-unblock coded measurements to the detector. Thus the scene is sampled according to the polar geometry of the rotating aperture, resulting in polar shaped image pixels. The geometry design of the polar coded aperture aims at improving the image sensing strategy.

Similar structures of polar images have been proposed with the name of “log-polar image” in the field of computer vision [57,58]. The concept of polar pixels has also been applied in CT [59], SPECT [60,61], Compton SPECT [62], and PET [63]. Our design of the polar coded aperture takes the advantages of the spokes-rings structure, as shown in Figures 2.11 (a) and (b). This structure transforms the image rotation motion directly into a circularly shift of the polar pixels. The proposed imaging system aims at obtaining a uniform spatial resolution across the scene. Uniformly sensing is achieved by designing the spaces between rings, resulting in a projection where the same pixel size is attained across the image.

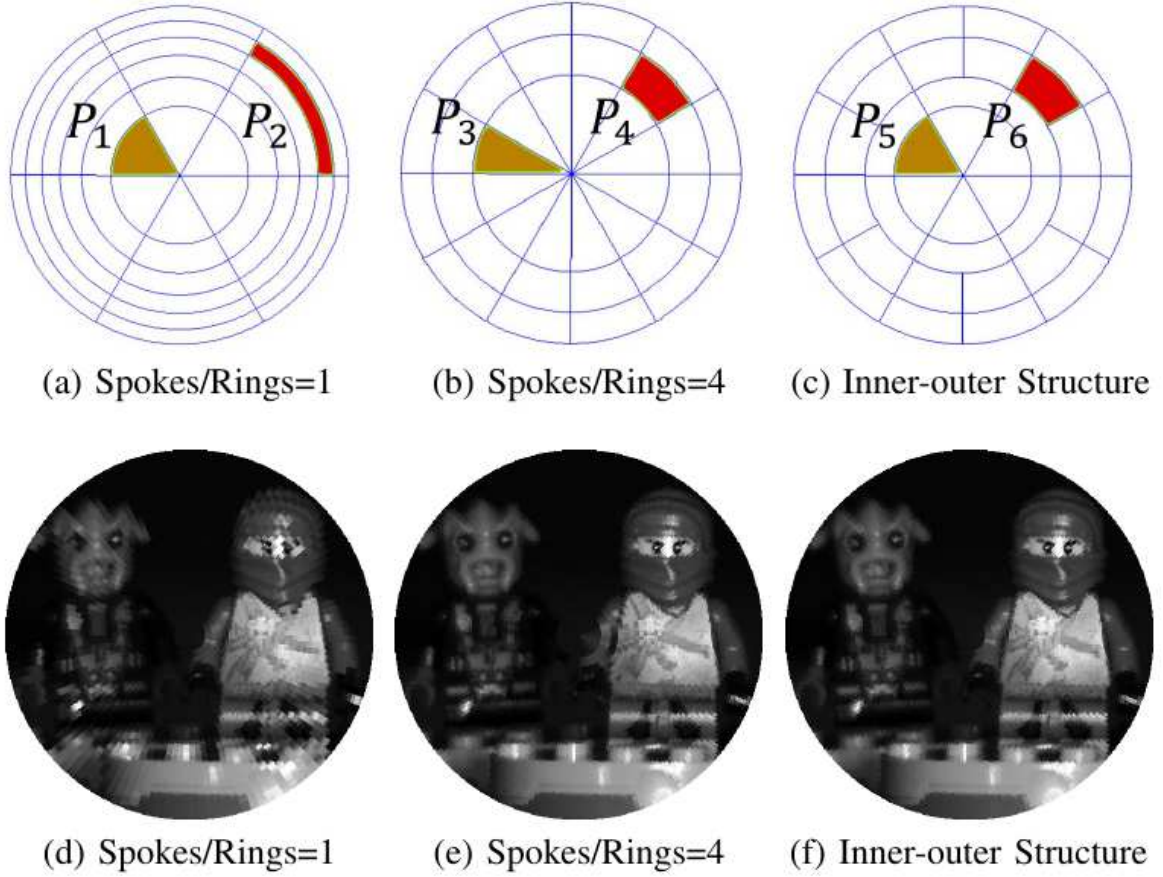


Figure 2.11: (a)-(c) show different polar aperture geometry designs with the shapes polar pixels being analyzed: (a) and (b) show the spoke-ring aperture structure with $S/R = 1$ and $S/R = 4$, respectively; (c) shows the inner-outer rings design. (d)-(f) are the examples of polar images with the corresponding polar pixels geometry in (a)-(c), respectively.

Denote R and S as the number of rings and spokes, respectively. Figures 2.11 (a) and (b) show the influence of the spoke-ring ratio S/R to the image quality: Higher density of rings leads to good image quality in the inner rings, while higher density of spokes leads to good image quality in the outer rings. To determine the optimal spoke-ring ratio S/R , an analysis of the pixel shape is shown in Figure 2.11 (a)-(b), where the pixels P_2 and P_3 are highly unbalanced in the lengths of their rings and spokes, resulting in a poor image quality. On the other hand, pixels P_1 and P_4 have similar rings and spokes lengths, resulting in a more balanced sensing along both dimensions which is desired in the geometry design. Denote the widths between the rings and the spokes in $(s, r)^{\text{th}}$ pixel as a_{sr} and b_{sr} , respectively, as shown in Figure 2.12, where s

indexes the spokes and r counts the rings. The design principle is to achieve a minimum difference between a_{sr} and b_{sr} for each pixel. Thus, a sum of the squared differences between a_{sr} and b_{sr} across all s and r is calculated as a cost function, expressed as

$$\text{Cost} = \sum_r \sum_s (a_{sr} - b_{sr})^2. \quad (2.27)$$

Then the cost values are computed for different S/R ratio, as displayed in Figure 2.13.

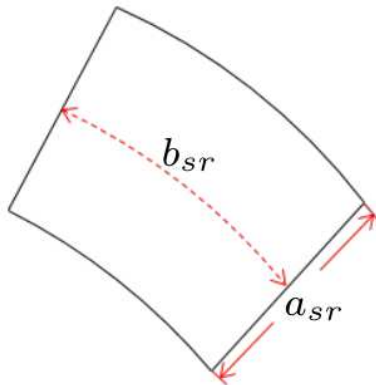


Figure 2.12: The shape of a polar pixel with rings distance a_{sr} and spokes distance b_{sr} .

$S/R = 4$ provides the minimal cost value. However, since the cost function only minimizes an average value, polar images with $S/R = 4$ still have unbalanced pixel shapes in the inner rings as shown in Figure 2.11 (b). Instead, the aperture with $S/R = 1$ provides more balanced pixel shapes in the inner rings as shown in Figure 2.11 (a). However, it suffers from unbalance pixel shapes in outer rings, resulting in a higher value of the cost function. The aperture with a fixed ratio of S/R can not provide good image quality in all spatial positions of the scene. Thus, a new geometry design of the polar aperture is proposed to have an inner-outer ring structure that is shown in Figure 2.11 (c). The new design keeps the spokes-rings structure with $S/R = 4$ in the outer rings, while reducing the number of the spokes in the inner rings to improve the overall image quality. The number of spokes in the inner rings is half of the spokes number in the outer rings, denoted as $S_{in} = 0.5S_{out}$, which results in a higher density of rings in the inner rings and a higher density of spokes in the outer rings. As shown in Figure 2.11 (d)-(f), the image quality is improved with the new design.

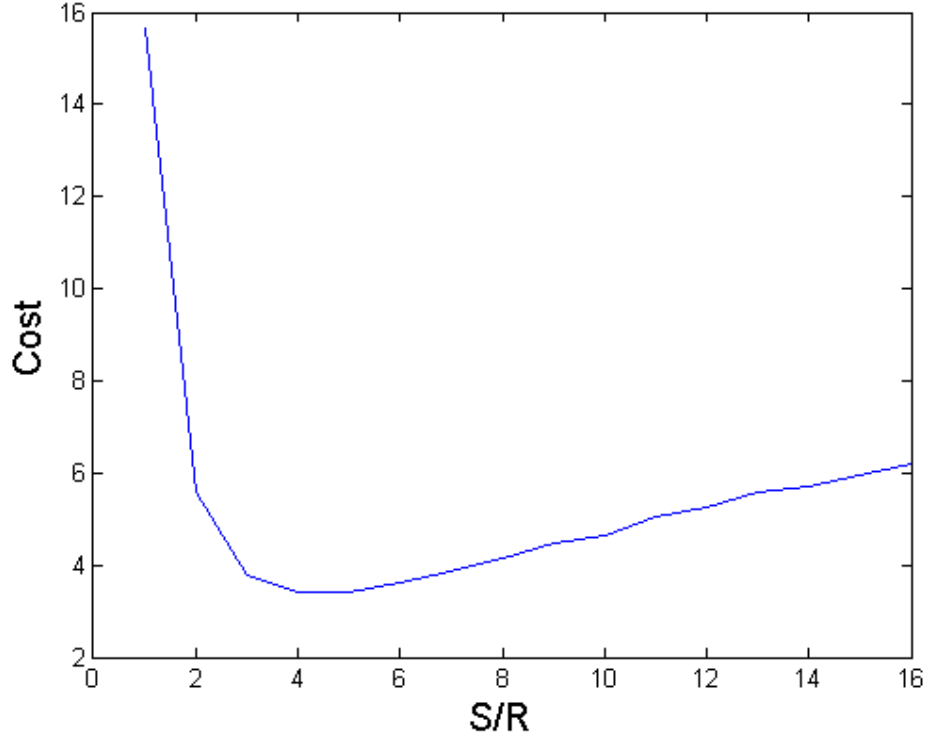


Figure 2.13: Plot of the cost function value changing with the spoke-ring ratio S/R varying from 1 to 16.

The inner-outer ring structure can be further designed by determining the inner-total rings ratio, defined as $\varepsilon = R_{in}/(R_{in} + R_{out})$. A proper value of ε is desired such that the cost function expressed in Eq. (2.29) is minimized. Figure 2.14 shows the cost function value changing with the variable ε when the numbers of inner spokes S_{in} are 128 and 256 respectively, with the constrain that the total number of polar coded aperture pixels remains S_{in}^2 . The values for ε between 0.2 to 0.3 result in smaller cost values, with the minima at $\varepsilon = 0.27$ for both $S_{in} = 128$ and $S_{in} = 256$ cases, with corresponding $R_{in} = 20$ and $R_{in} = 40$, respectively.

This result is verified by showing an image quality comparison with 6, 20, and 60 inner rings (with the corresponding $\varepsilon = 0.09, 0.27$ and 0.64), as shown in Figure 2.15. In this comparison, the number of pixels are fixed as $S_{in}^2 = 128^2$. With two regions on the eyes and chest of the toy zoomed, it is clear that the image sampled by a $R_{in} = 20$ polar aperture obtains better image quality in both areas.

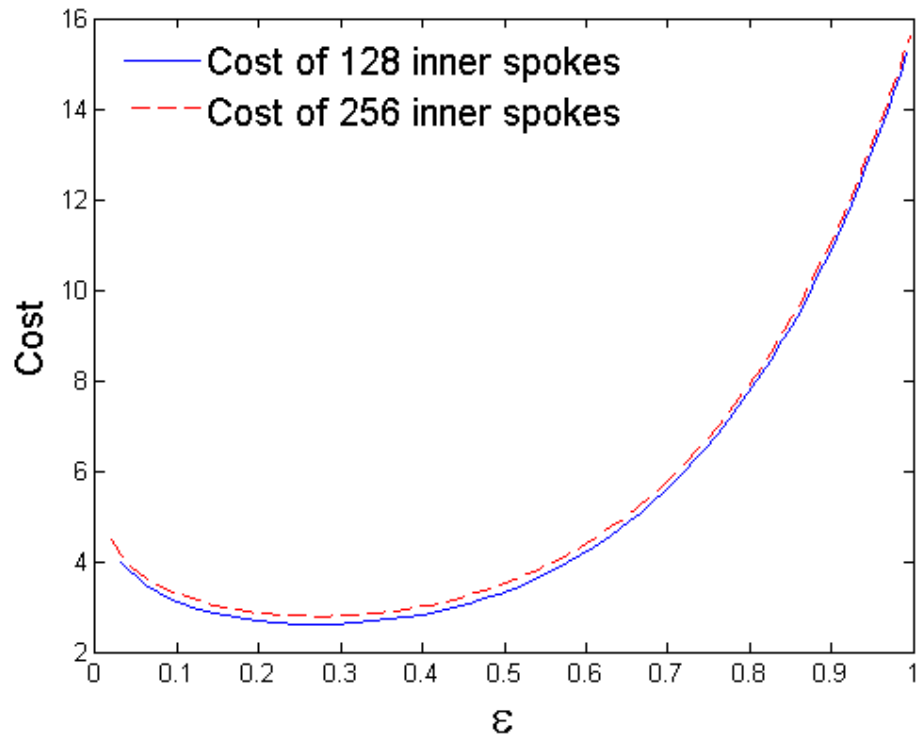


Figure 2.14: Plots of the cost function value changing with the inner-total rings ratio $\epsilon \in [0, 1]$ in both 128 inner spokes and 256 inner spokes coded apertures.

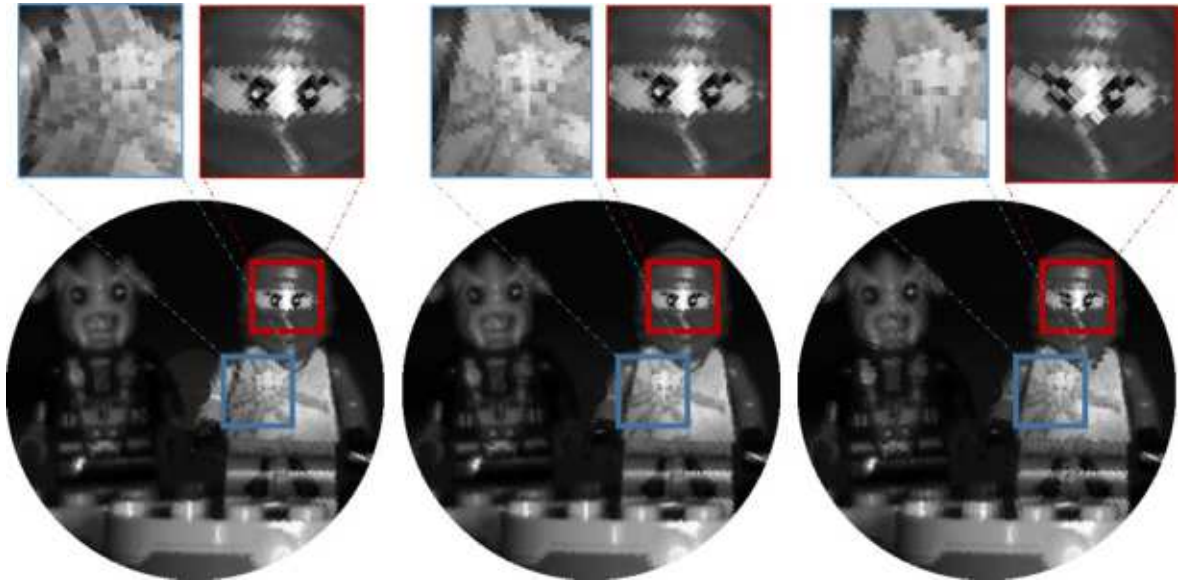


Figure 2.15: Comparison of image quality with 6 (left), 20 (middle) and 60 (right) inner rings with the polar pixel number restricted to be 128^2 . Better image quality with 20 inner rings is observed in both zoomed regions.

2.4 Computer Simulations

2.4.1 Polar Data Cube Acquisition and Measurements Simulation

To further study the proposed imaging system, computer simulations are performed with a polar spectral data cube acquired in the laboratory. A wide-band Xenon lamp is used as the light source and a visible monochromator is applied to capture spectral bands on a $9.9\mu\text{m}$ CCD camera. In this way, a $256\times 256\times 16$ data cube is obtained. Then, the acquired data cube is transformed into a polar data cube with 20 inner rings and 54 outer rings by software. The numbers of spokes are 128 and 256 in the inner and outer rings, respectively. Fig 2.16 shows the 9 polar spectral image bands selected from the total $L = 16$ bands. The center wavelengths of each spectral channel are uniformly distributed in the range from 451nm to 661nm.

In the simulation, the polar coded aperture has $R_{in} = 20$ inner rings and $R_{out} = 54$ outer rings. $S_{in} = 128$ and $S_{out} = 256$ spokes are uniformly spaced in the inner rings and outer rings, respectively. A random binary code with 50% open is applied on the polar coded aperture. The continuous variable circular bandpass filter is simulated with the center wavelengths ranging from 476nm to 635nm. The bandwidth is assumed to be 80nm. Meanwhile, a $N^2 = 32^2$ FPA sensor is utilized to capture the compressed projections. Then the compressive sensing ratio (CS ratio) of K snapshots measurements is defined as

$$\kappa = \frac{KN^2}{VL}, \quad (2.28)$$

where $V = S_{in}R_{in} + S_{out}R_{out}$.

By applying Eq. (2.21), 64 snapshots measurements are simulated, where the CS ratio is $\kappa = 25\%$. In order to show the simulation process, Figure 2.17 (a) displays the RGB images of the spatial and spectral modulated polar data cube before being projected on the FPA. The RGB images demonstrate the aperture coding and CVF spectral modulation to the scene. The spatial resolution of each RGB image is 128^2 . The corresponding simulated compressed projections are displayed in Figure 2.17 (b),

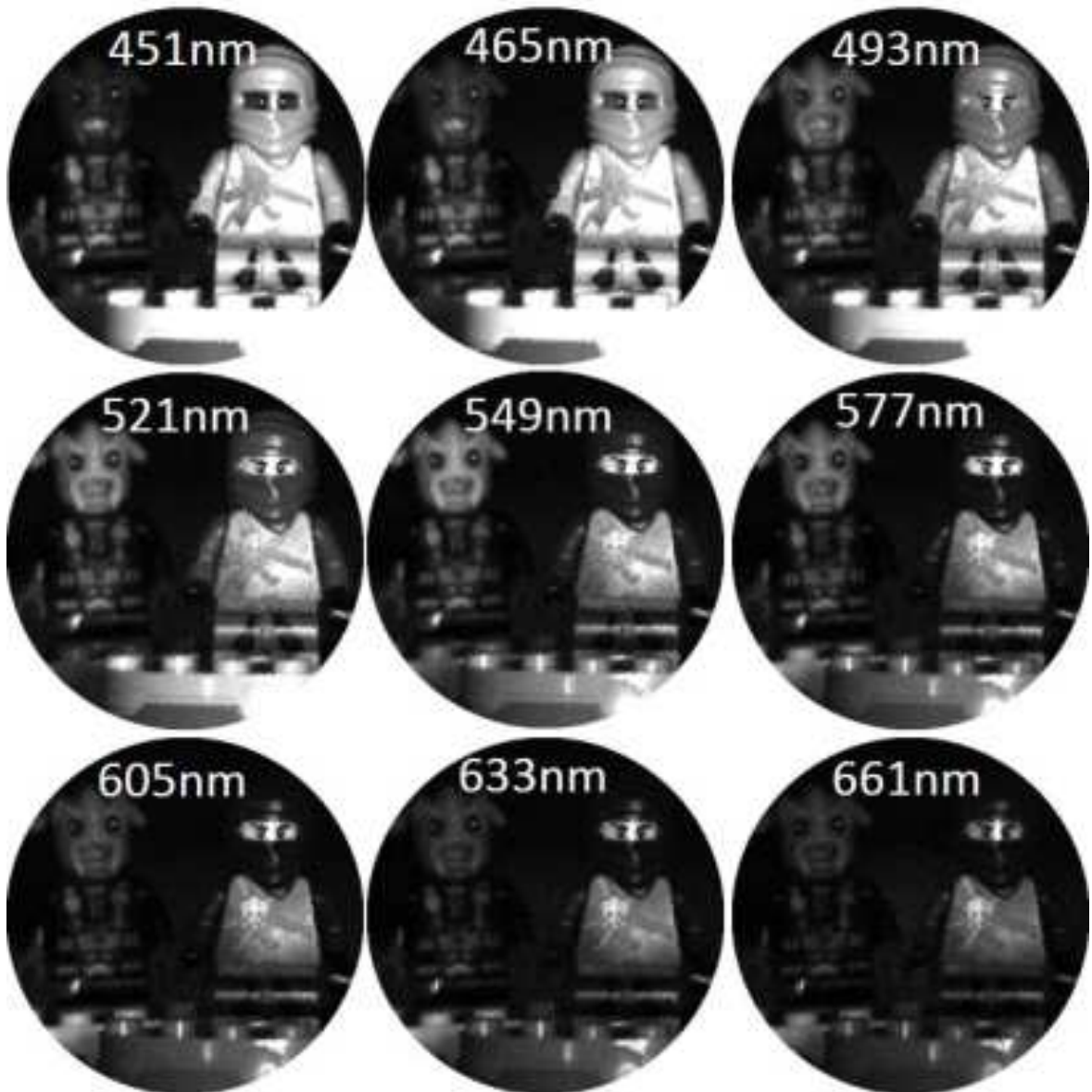


Figure 2.16: 9 spectral image bands selected from the total 16 bands are displayed. The center wavelength of each band is indicated. Two image points are selected for the spectral reconstruction comparisons.

demonstrating the spatial and spectral integration on the low resolution monochromatic FPA. The spatial resolution of these FPA projections is 32^2 .

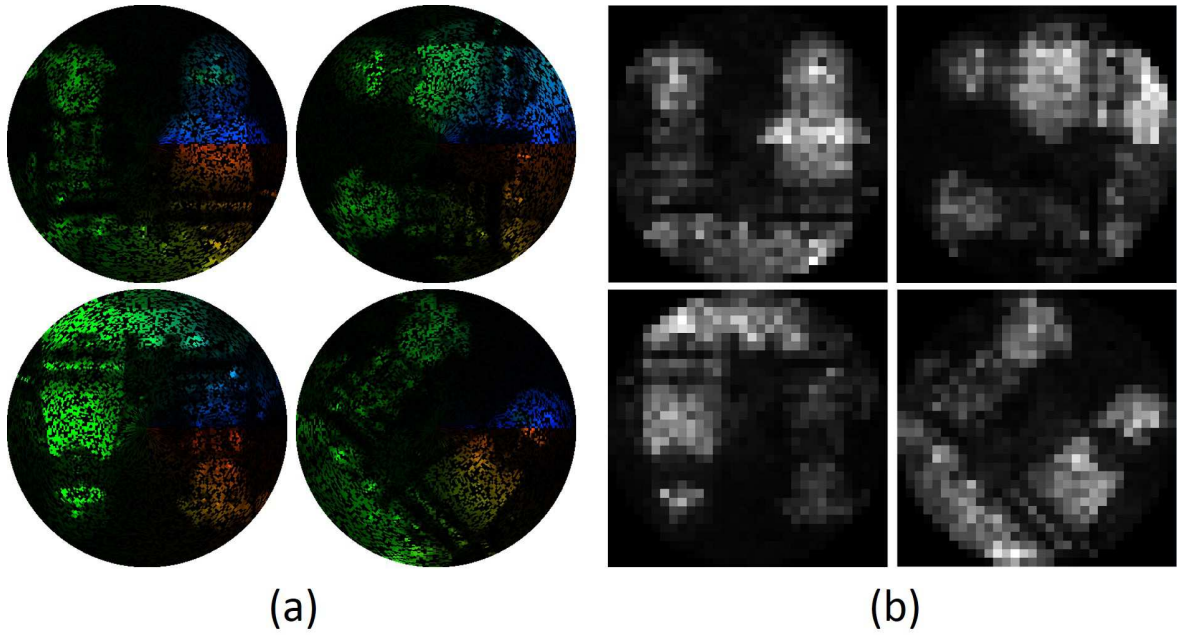


Figure 2.17: (a) shows the RGB images of the spatial and spectral modulated polar data cube before projected on the FPA detector. (b) shows the corresponding compressed FPA projections. 4 snapshots selected from the total 64 snapshots are displayed.

2.4.2 Reconstruction with Simulated Measurements

The reconstruction procedure applies the GPSR algorithm to solve the $\ell_1 - \ell_2$ function described in Eq. (2.28), where the representation basis utilizes a 2D Wavelet basis and a 1D Cosine basis in the spatial and spectral domains, respectively. Peak signal to noise ratio (PSNR) is calculated for each reconstructed spectral channel.

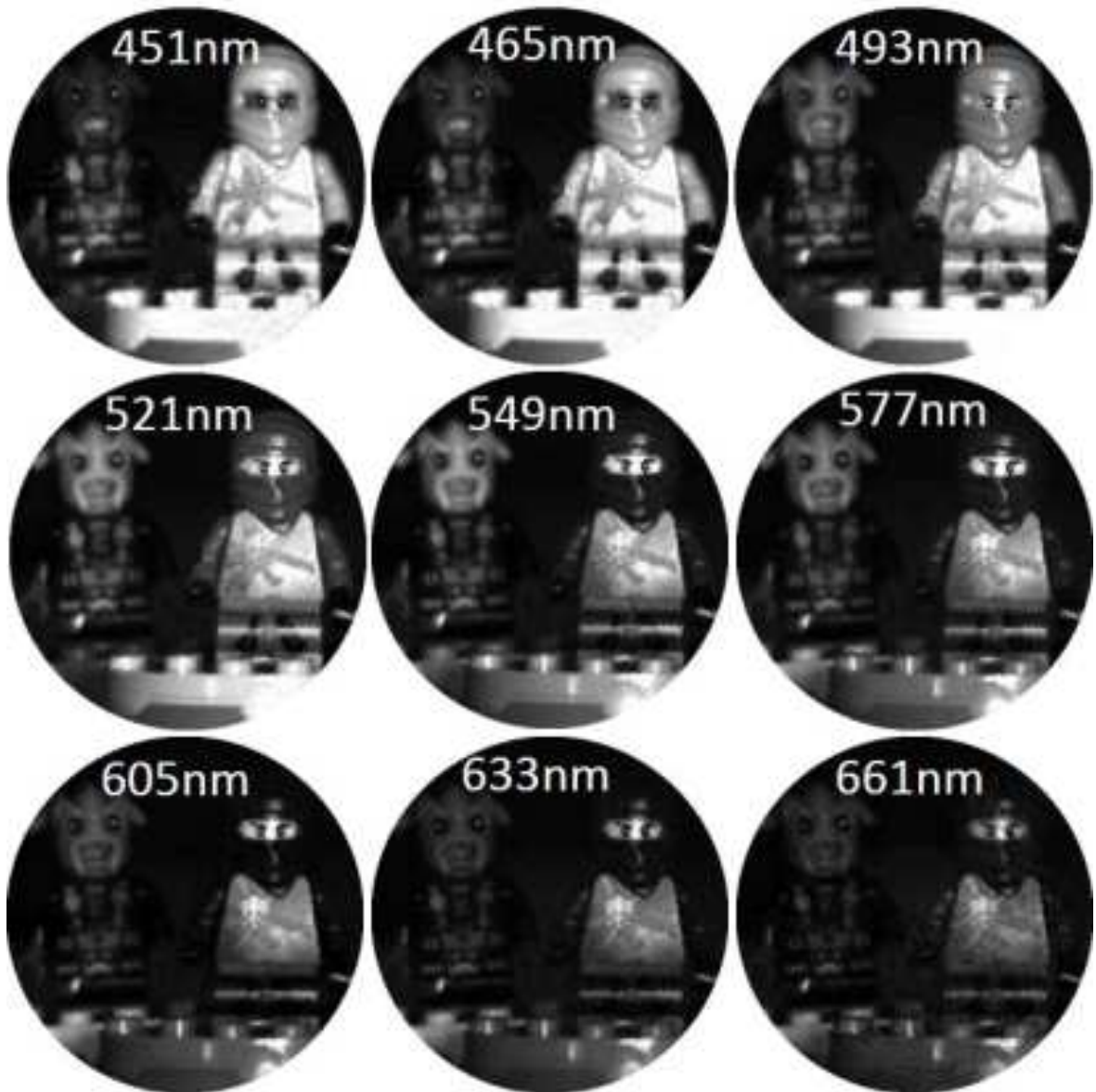


Figure 2.18: 16 spectral image bands are reconstructed from 64 snapshots compressed measurements with $\kappa = 25\%$ CS ratio, where 9 image bands are displayed. The average PSNR is 32dB.

Figure 2.18 shows 9 image bands selected from the reconstructed 16 spectral bands. The average PSNR is 31.8dB. Good image quality is observed in the reconstructed spectral bands. With a larger number of snapshots captured, more information of the polar data cube is acquired, with a higher reconstruction accuracy expected. Thus, simulations are performed with different numbers of snapshots applied in the

reconstruction. The PSNRs of the reconstructions are calculated and displayed in Figure 2.19. The simulation results verify the performance improvement by increasing the number of snapshots. Note that the maximum number of snapshots is limited by the number of spokes in inner rings, which has a CS ratio of 50%. The spokes-rings coded aperture structures with $S/R = 1$ and $S/R = 4$ have similar reconstruction performance compared with the inner-outer ring coded aperture in Figure 2.19. This is not surprising since the geometry design of the polar coded aperture aims at better image quality instead of better reconstruction performance. The reconstruction quality could be improved by further optimizing the aperture code patterns.

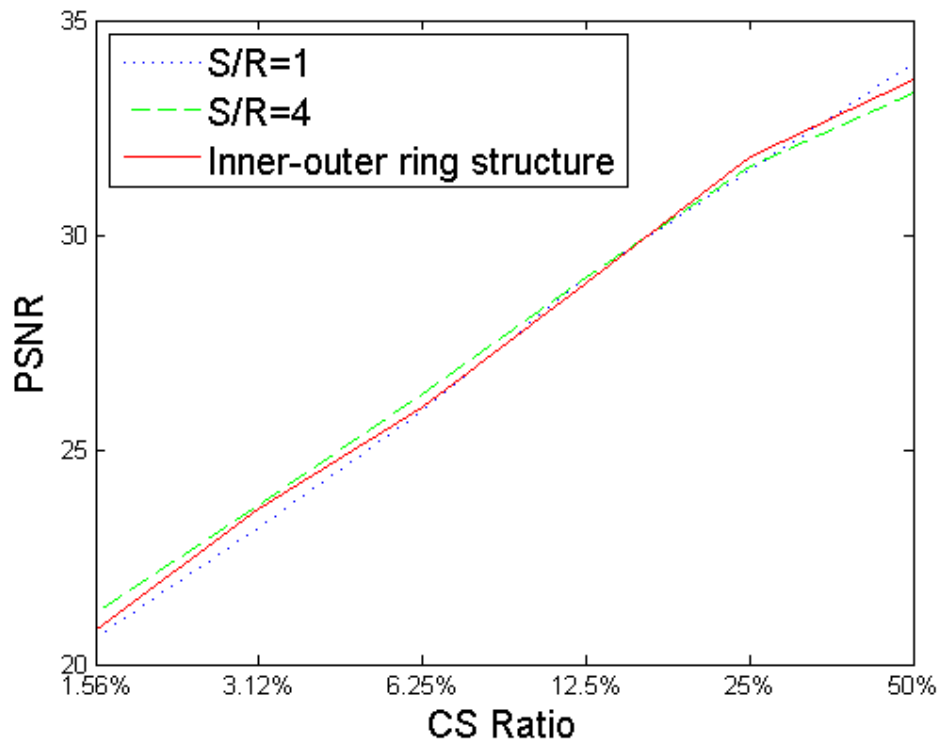


Figure 2.19: Average PSNRs are calculated for different polar coded aperture geometry designs with the number of snapshots ranging from 4 to 128. The corresponding CS ratio ranges from 1.56% to 50%.

Note that a random coded aperture with 50% open can generally produce better reconstruction in polar coded aperture compressive sensing imaging. In this simulation, the performance decreases by 0.6dB PSNR if the transmittance is decreased to 30%.

When the transmittance increases to 80%, a PSNR reduction of 0.8dB is observed. The FPA resolution influences the reconstruction quality. A higher resolution FPA performs slightly better, due to the additional spatial measurements per snapshot and better spectral bands differentiation. For example, the reconstruction from 8 shots in a 64^2 FPA is 0.6dB better than the reconstruction from 128 shots in a 16^2 FPA. However, we should also point out that the reconstruction performance is determined by all hardware configurations including the FPA resolution, the CVF bandwidth and the coded aperture patterns. In addition, higher resolution FPAs are typically more costly, particularly in the IR bands.

Sensor noise can also influence the reconstruction performance. Here we define the signal-to-noise ratio (SNR) in the sensor as the ratio between the variance of the sensor measurements and the variance of sensor noise, $\text{SNR} = 10\log_{10}\text{Var}(\mathbf{g})/\text{Var}(\mathbf{n})$, where \mathbf{n} represents the noise. When Gaussian white noise resulting in 30dB, 20dB and 10dB SNR is added to the measurements, the resulting PSNR decreases 2dB, 5dB and 8dB, respectively. The optimal choice of the regularization parameter τ in Eq. (2.28) tends to be larger with stronger noise, indicating that more effort is needed in ℓ_1 minimization for a smooth image recovery. The robustness can be improved by employing alternative optimization algorithms with noise reduction.

2.4.3 Influence of the Bandpass Filter Bandwidth

The bandwidth and the range of the center wavelengths of the continuous variable bandpass filter have a great impact on the values of the spectrum modulation c_{srk}^ℓ , which eventually influence the sensing matrix \mathbf{H} and the reconstruction quality. Generally, if the bandwidth of the bandpass filter is too narrow, not enough of the spectral information is compressively sensed, causing poor reconstructions. Meanwhile, if the bandwidth is too wide to provide distinct modulation for different spectral bands, the proposed imager will fail in the spectral reconstruction.

To study this influence, a data cube with 128 spectral bands is applied in the measurements simulation procedure, where the high spectral resolution results in a

more precise simulation of the continuous variable bandpass filter. Simulations are performed with a varying ratio $\gamma = b_w/(\lambda_{max} - \lambda_{min})$ between the bandwidth b_w and the center wavelengths range $\lambda_{max} - \lambda_{min}$, while keeping the total transmitted wavelength range $[\lambda - b_w/2, \lambda + b_w/2]$ fixed. 8, 16 and 32 spectral bands are reconstructed respectively. PSNRs are calculated with γ ranging from 0.02 to 1 as shown in Figure 2.20. With the extreme values of $\gamma = 0.02$ or $\gamma = 1$, poor reconstructions are

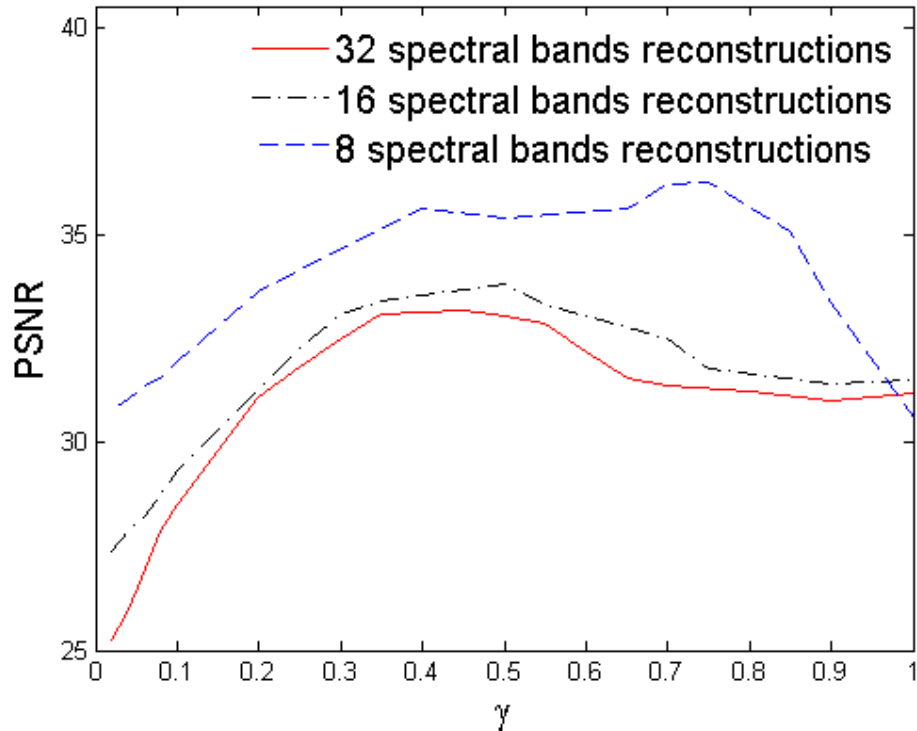


Figure 2.20: PSNRs of 8, 16 and 32 spectral bands reconstructions from 64 snapshots are displayed with γ varying from 0.02 to 1.

acquired as expected. However, the best values of γ gradually decrease from 0.75 to 0.35 when the number of recovered spectral bands increases from 8 to 32, indicating that a narrower bandpass filter is preferred when a higher spectral resolution is desired.

2.4.4 Hyper-Spectral Reconstruction

For further verification of the spectral reconstruction attained, simulations aim at accurate spectral reconstruction with a large number of spectral bands. A 128 bands

data cube is used with a spatial resolution of 32^2 polar pixels. The 580nm image band is shown in Figure 2.21 (a), where two image points are selected for spectral signature comparisons.

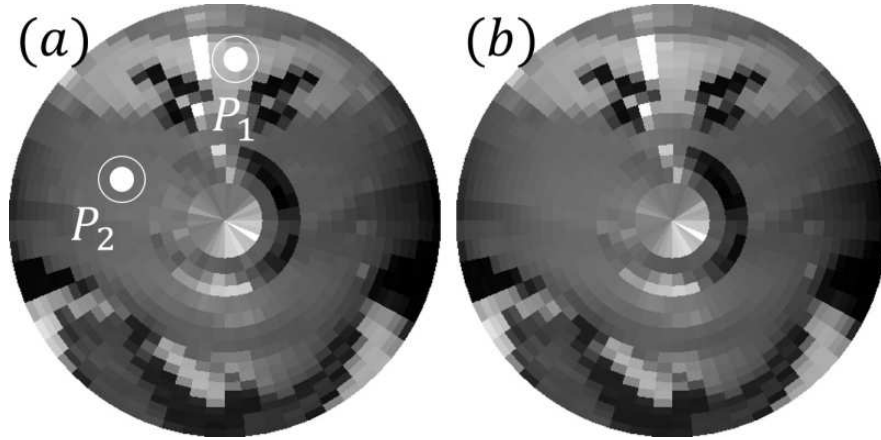


Figure 2.21: The original 580nm image plane (a) and its corresponding reconstruction (b) are displayed. 40dB PSNR is achieved with $\kappa = 25\%$. Two image points are selected for spectral signature reconstruction comparisons.

With a 32^2 resolution FPA detector, 32 snapshots are simulated, where the CS ratio defined in Section IV. A is $\kappa = 25\%$. As discussed above, the reconstruction of a larger number of spectral bands requires a continuous variable filter with a narrower bandwidth. For 128 spectral bands reconstruction, a 11.6nm bandwidth is selected and applied in the simulation, with the corresponding $\gamma = 0.1$. The reconstruction achieves an average of 40dB PSNR, with the reconstructed 580nm image plane displayed in Figure 2.21 (b). The reconstruction of spectral signatures in 128 bands are displayed in Figure 2.22. The spectrum region between 571nm and 590nm containing 20 bands is zoomed for a detailed comparison. The spectral reconstructions of both points are quite close to the original spectral signatures, showing an accurate hyper-spectral recovery.

2.5 Continuous Imager Rotation Model

For the proposed imager to be mounted on spinning devices, a more precise sensing model is developed by considering the continuous rotation motion. When the

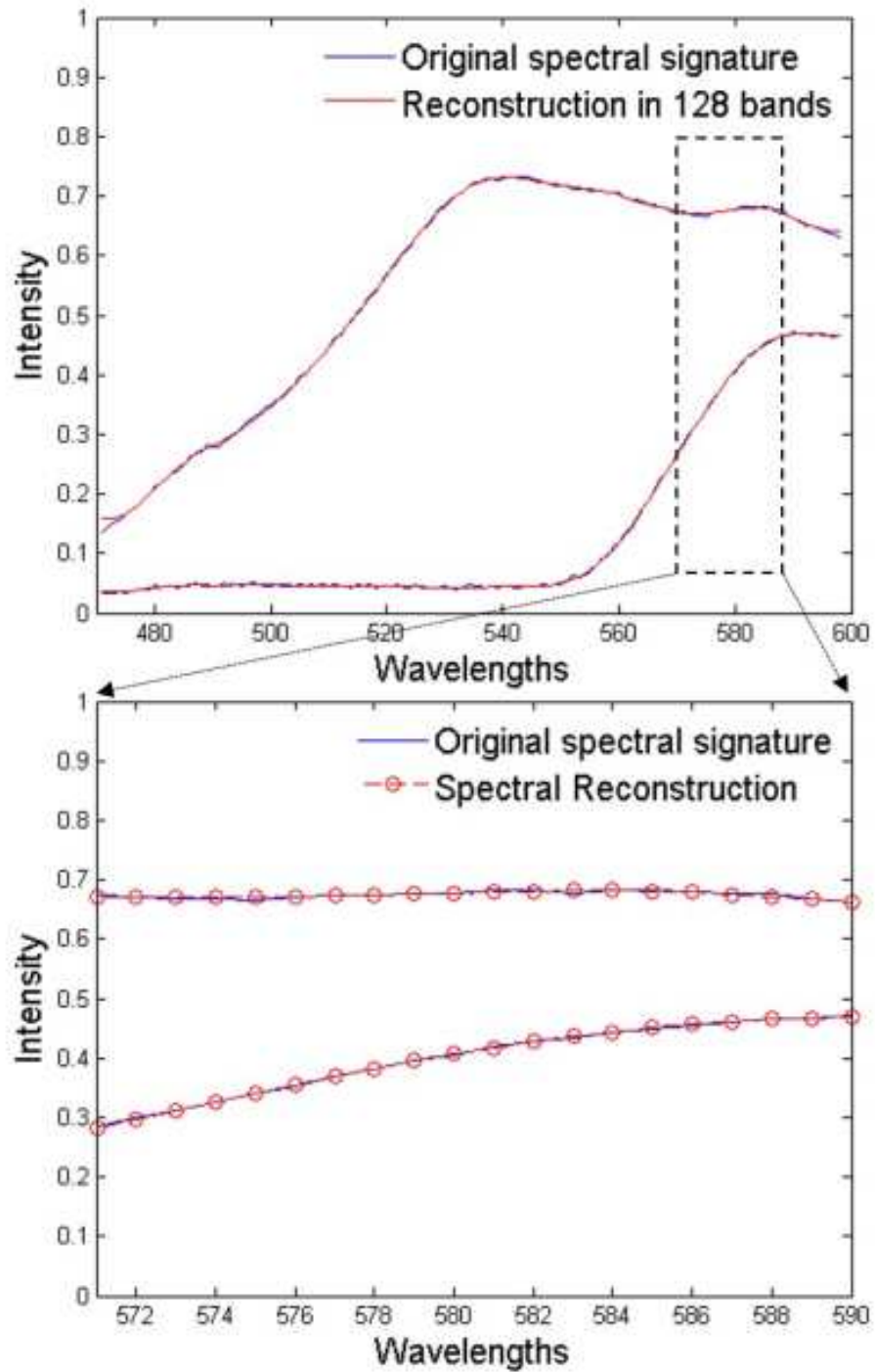


Figure 2.22: 128-band spectral reconstructions are compared with the original spectral signatures of two image points. The reconstructions of 20 bands from 571nm to 590nm are zoomed for further comparisons.

continuous rotation is taken into account, the polar pixels in the data cube shears circularly during the integration time (or the shutter time) τ_s , as shown in Figure 2.23.

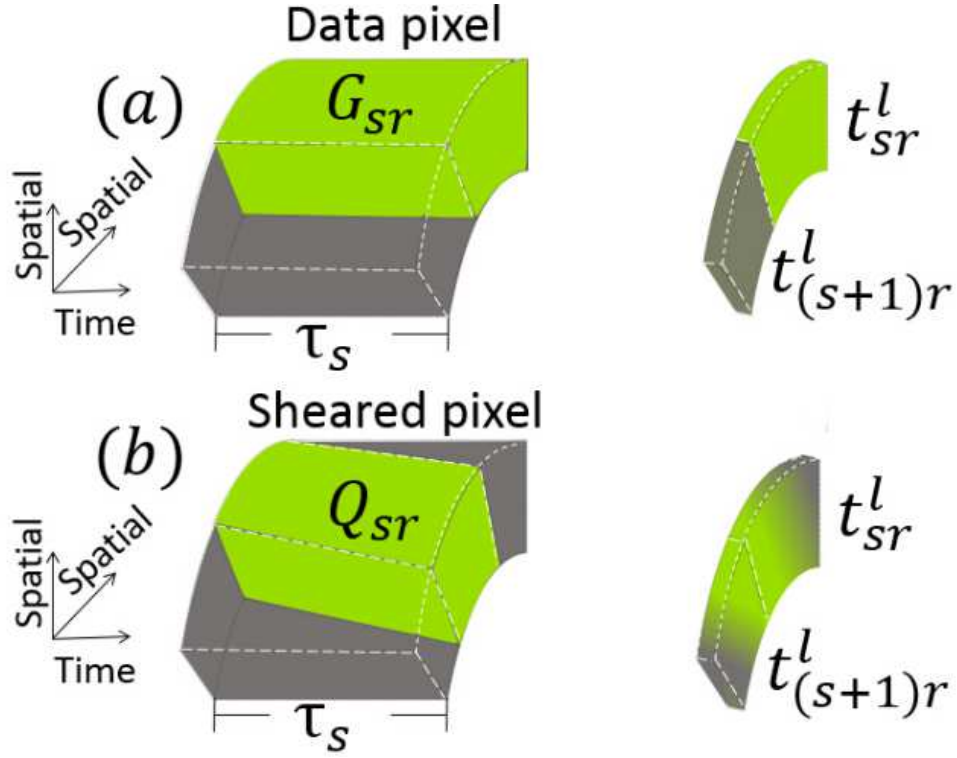


Figure 2.23: (a) shows a data pixel entering the polar coded aperture with no transformation, when the discrete approximation of the imager rotation is applied. (b) displays a circularly sheared data pixel hitting two adjacent polar aperture pixels, when the continuous rotation motion of the imager is considered.

From the figure, denote the region of the original polar pixel during the time τ_s as G_{sr} ; and denote the sheared pixel region during τ_s as Q_{sr} . Then the proportions of the $(s, r)^{\text{th}}$ shear data pixel entering into the polar coded aperture pixels are calculated as

$$\beta_{sru} = \left(\iiint_{Q_{sr} \cap G_{(s+u)r}} \rho d\rho d\varphi dt \right) \left(\iiint_{Q_{sr}} \rho d\rho d\varphi dt \right)^{-1}, \quad (2.29)$$

where u indexes the adjacent polar aperture pixels hit by the $(s, r)^{\text{th}}$ sheared data pixel. The sum of the proportions satisfies $\sum_u \beta_{sru} = 1$ for each sheared data pixel.

Then the discrete sensing model in Eq. (2.21) is changed to a more precise model as

$$g_{mn}^\ell = \sum_r \sum_s \sum_k \sum_u w_{srmn}^\ell t_{sr}^\ell c_{srk}^\ell \beta_{sru} f_{srk}, \quad (2.30)$$

where the imager is assumed to rotate at a constant speed and the shutter time τ_s is assumed to be constant for each snapshot. Thus, the proportions β_{sru} are unchanged during distinct snapshots. The sensing matrix \mathbf{H}^ℓ in Eq. (2.22) becomes

$$\mathbf{H}^\ell = \mathbf{W}^\ell \mathbf{P}^\ell \mathbf{B}, \quad (2.31)$$

where the rotation matrix \mathbf{B} contains the proportions β_{sru} for each data pixel. Since each spectral band has the same rotation procedure, \mathbf{B} consists of L diagonal blocks. Each block has the same entries, with the dimensions of $V \times V$. To visualize \mathbf{H}^ℓ , the test data cube used in displaying Figure 2.5 and Figure 2.7 is applied here. Then the corresponding \mathbf{H}^ℓ in the continuous rotation model is displayed in Figure 2.24.

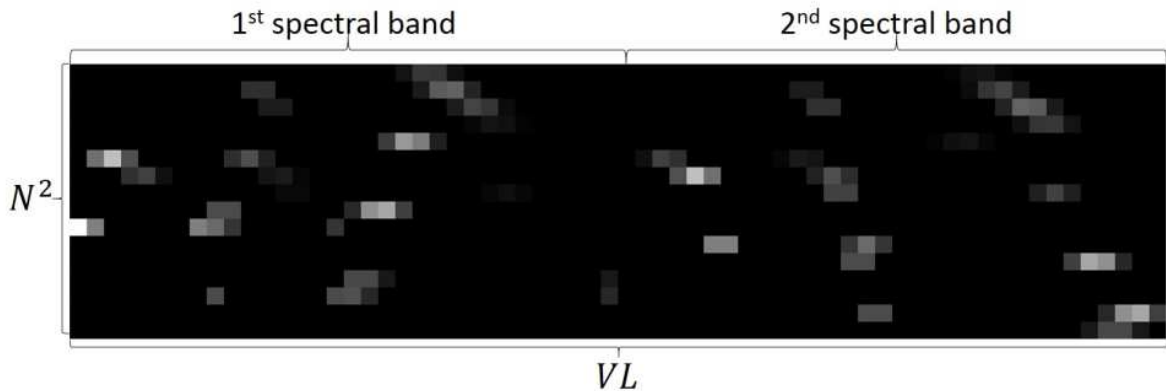


Figure 2.24: Sensing matrix in the continuous rotation model \mathbf{H}^ℓ for a $S_{in} = 8$, $S_{out} = 16$, $R_{in} = 2$, $R_{out} = 1$, $L = 2$ data cube and an $N^2 = 4^2$ FPA.

Denote the rotation period of the imager as τ_r . Assuming K snapshots are desired, the shutter time τ_s should have an upper bound in order to achieve the desired number of snapshots. The acceptable value range of the shutter time is $[0, \tau_r/K]$. Then a normalized shutter time is defined as

$$\eta = \frac{K \tau_s}{\tau_r}, \quad (2.32)$$

where $\eta \in [0, 1]$. In the following experiment, 64-shot measurements are simulated by Eq. (2.32), applying the continuous rotation model. A comparison between the reconstructions with discrete approximation model and the continuous rotation model is desired. PSNRs are calculated in both reconstructions, as shown in Figure 2.25.

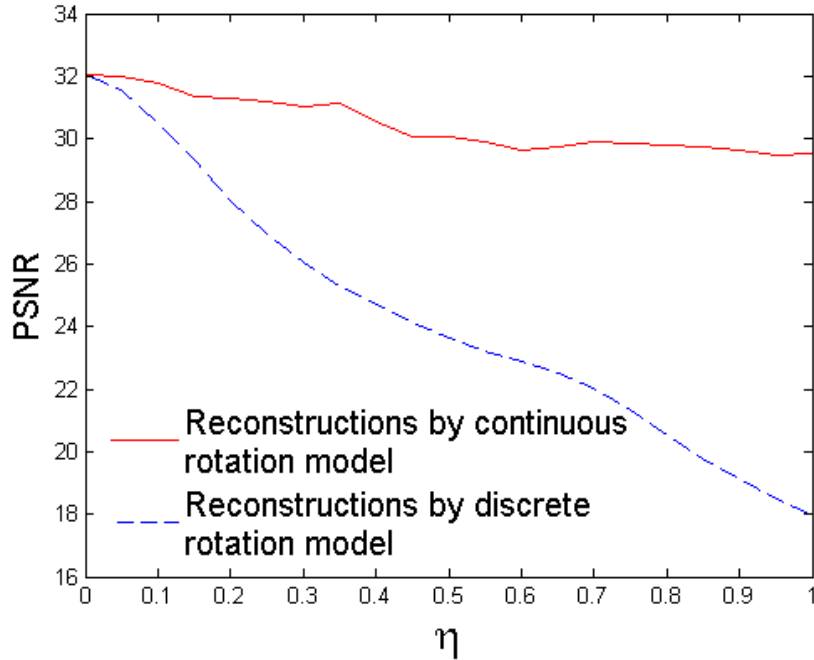


Figure 2.25: PSNR comparison between discrete rotation model reconstruction and the continuous rotation model reconstruction. 64 continuous rotation compressed projections are simulated with the normalized shutter time η increasing from 0 to 1.

From this experiment, A slight PSNR decrease is observed with the reconstructions by the continuous rotation model when η increases from 0 to 1; while the discrete rotation model suffers from a PSNR decrease with an increasing η . This is because the discrete rotation model fails to model the imager rotation during each FPA integration period, leading to $\mathbf{g} - \mathbf{Hf} \neq \mathbf{0}$. The modelling error increases with larger value of η , reducing reconstruction performance. A further comparison of reconstruction quality between the two approaches is shown in Figure 2.26, where simulations with $\eta = 0.5$ are performed. The reconstructed image using the discrete rotation model shown in Figure 2.26 (b) is blurred, with the rotation motion contained. On the other hand,

Figure 2.26 (a) shows a sharp reconstructed image by utilizing the continuous rotation model.

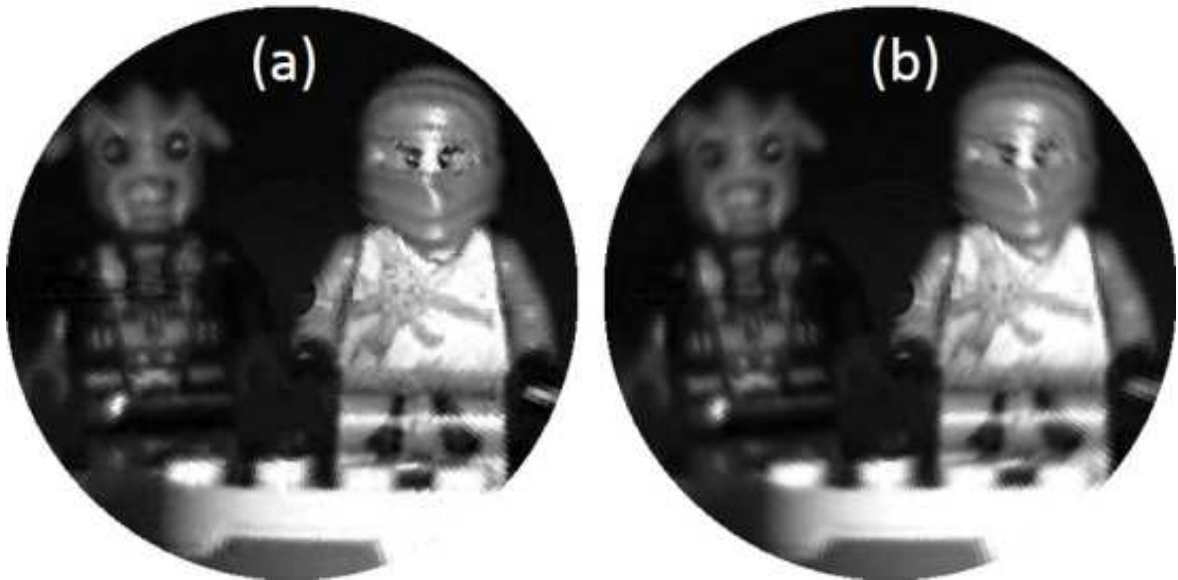


Figure 2.26: (a) shows the 4th spectral image band reconstructed by applying the continuous rotation model, with 30.1dB PSNR; (b) displays the same spectral band recovered by utilizing the discrete rotation model with the corresponding PSNR 23.6dB.

2.6 Conclusion

This chapter describes a compressive spectral imaging system mounted on rotating equipment, such as munitions. The scene is spatially coded by a polar coded aperture and spectrally modulated by a continuous variable circular bandpass filter. The rotations generate various spatial and spectral modulations. Multiple compressive coded projections are thus captured on the FPA. An inverse algorithm is then applied to reconstruct a spatial spectral data cube. Computer simulations showed accurate spatial and spectral reconstructions when using only a fraction of the full amount of measurements. Design parameters, such as the aperture code geometry and CVF bandwidth, were explored and optimized to enhance image quality. The imager's versatility as a hyper-spectral camera was demonstrated with simulations reconstructing up to 128 spectral bands. A continuous rotation model was developed and simulated, successfully correcting for image blur observed in the discrete model. Although the application in

guided munitions requires further research with additional practical considerations, the computational models and the simulation results imply a promising result in the real implementation of the proposed compressive sensing imager.

Chapter 3

OPTIMIZATION AND EXPERIMENTAL DEMONSTRATION OF A COMPRESSIVE POLAR CODED APERTURE SPECTRAL IMAGER

Compressive polar coded aperture spectral imaging was introduced in the previous chapter, where a circular variable filter is used for spectral modulation while a randomly distributed polar coded aperture is the key component providing random blocked-unblocked spatial coding to the scene. This chapter develops an optimization framework for the polar coded aperture patterns to construct a better conditioned measurement matrix. The designed polar coded apertures are fabricated on a photo-mask through lithography. The experimental demonstration is then provided based on a testbed implementation of the imaging system. It is shown that the optimized coded apertures significantly improve the reconstruction quality in both computer simulations and experiments.

3.1 Introduction

Coded aperture compressive spectral imaging has attracted a large amount of attention in recent years [15,16]. Dispersive elements are typically applied for spectrum separation, while a square shaped block-unblock coding mask performs spatial modulation. Multiple snapshots can be captured by employing a digital micro-mirror device (DMD), where 50% blocked random coding patterns are typically applied [17]. The reconstruction performance of a compressive spectral imager is improved through a careful selection of optical elements as well as optimizing the measurement matrix in the compressive sensing process. In coded aperture spectral imagers, this leads to coded aperture optimization [20,23,64-66].

In the previous Chapter a polar coded aperture compressive spectral imager was proposed. Different from conventional compressive spectral imagers, it applies a circular variable filter (CVF) for spectral modulation. The CVF spectral response continuously changes along the angular position of the filter. When mounted on spinning devices such as a munition, this imager sequentially captures a number of compressive coded measurement shots on its low resolution sensor array during a 2π rotation. A novel polar-shaped block-unblock coded aperture is used to perform compressive sensing on rotating imagers. Although low resolution sensors are used, the spatial resolution of the imager is determined by the coded aperture. While rotating, the proposed imager performs a dynamic spatial and spectral modulation to the scene. This makes it possible to perform multi-snapshot compressive sensing. Although efforts have been made to improve the reconstruction performance by the selection of optical elements, such as varying the CVF bandwidth, the optimization of the compressive sensing measurement matrix has not yet been considered. The previously proposed imaging system contains a 50% random polar aperture code which is sub-optimal. Moreover, only mathematical modeling and computer simulations were performed without any experimental implementation.

The contribution of this chapter is twofold: First, we propose a coded aperture optimization algorithm to construct a better conditioned measurement matrix. This improves the reconstruction performance of the polar coded aperture spectral imaging system. Then, a proof-of-concept optical experiment is conducted using the fabricated polar coded apertures.

A challenge of compressive sensing reconstruction is the inverse of an ill-conditioned sensing matrix, although sparsity constraints are applied to narrow down the solution space. Careful design of the sensing matrix will improve reconstruction quality. The optimization of a sensing matrix with element-wise flexibility was previously reported in [67-70]. In compressive imaging systems, the measurement matrix is usually highly structured, where the entries of the measurement matrix are limited to some discrete values. This is certainly the case when a block-unblock coded aperture is contained

in the imaging system, where the sensing matrix optimization converts into the design of binary aperture coding patterns. For these systems new optimization methods are needed. Several multi-frame coded aperture optimization algorithms have been proposed for different compressive spectral imaging systems [20,71,72]. These algorithms take advantages of multiple snapshots where a set of independent coded aperture patterns for different snapshots must be designed. In particular, complementary multi-snapshot coding patterns are developed where each image cube voxel is sensed exactly once during the sensing process. It is mathematically proven that this process of uniformly sensing the three dimensional scene produces a better-conditioned sensing matrix than using random patterns [20]. Complementary blue noise patterns are further designed in [71,72] which aim to achieve uniform sensing across each spectral image plane. Compared with these multi-snapshot aperture coding imaging systems, the design flexibility is further reduced in the rotating polar coded aperture design. Even though multiple snapshots are captured, the coding patterns of different snapshots are actually a rotated version of a static coding pattern. Furthermore, the complementary condition does not apply in this polar coded aperture spectral imaging system due to the large number of snapshots required. Thus in this chapter, we develop a new coded aperture design algorithm that can accommodate the constraints placed on the structure of the sensing matrix while considering both uniform sensing and coded aperture transmittance.

The designed aperture coding patterns are fabricated and implemented in laboratory testbed experiments. The coded photo-mask is placed on the image plane of the objective lens, and aligned to the sensor array through a relay lens. A precision rotation stage is involved to introduce the spinning motion to the system. The spectrum filtering effect of a CVF filter is emulated through the use of a set of visible bandpass filters. Spectral images are then recovered from experimental measurements by solving the inverse problem of the calibrated sensing matrix. A comparison of the reconstructions using random and optimized code patterns is displayed.

This Chapter is organized as follow. Section 3.2 demonstrates the optimization

procedure on the polar aperture code. Computer simulations are followed in section 3.3 to further evaluate the performance of the optimization algorithm. Section 3.4 describes the laboratory experiments, including the alignment and calibration process, as well as the measurement acquisition and spectral images reconstruction. Reconstruction results from the optimized code pattern and a random pattern are compared, demonstrating the effectiveness of the optimization algorithm.

3.2 Polar Coded Aperture Optimization

During the development of this polar coded aperture spectral imager, an analysis on the influence of the CVF filter bandwidth was performed. Specifically a higher spectral resolution requires a sharper CVF filter. The CVF bandwidth can then be optimized based on the expected numbers of spectral bands. To further improve the reconstruction quality of the proposed imaging system, efforts should be made to optimize the design of the sensing matrix $\mathbf{A} = \mathbf{H}\Psi$. Without further prior knowledge on the scene, it's usually difficult to define the quality of the sparsity basis Ψ . The structure of the measurement matrix \mathbf{H} is determined by the optical hardware. In this imaging system, \mathbf{H} is determined by the coded aperture structure, the aperture coding pattern, the CVF modulation, the sensor resolution and the number of measurement shots. Different designs on the structure of the polar coded aperture were developed, such as the spokes-rings ratio, and inner-outer rings ratio. These parameters have been optimized to improve the image quality. However in computer simulations, this optimization does not affect image recovery accuracy. The reconstruction quality was also analyzed in different sensor resolution and measurement shot settings. The design flexibility of \mathbf{H} remains in the aperture coding pattern design, i.e, the design of distributions of blocked and unblocked pixels in the coded aperture.

50% random binary coding patterns have been used in this polar coded aperture spectral imaging system because they are statistically incoherent with the sparsity basis. In practice, randomness usually generates variation in the reconstruction quality for many compressive spectral imaging systems [23,35]. One way to solve this problem

is through placing statistical constraints on the randomness. For example, blue noise binary coding [73,74] is shown to perform much better than white noise binary patterns in some compressive imaging systems [72]. The blue noise patterns tend to preserve the high frequency information in images and the sensing process tends to be more uniform across the scene. For multi-snapshot compressive imaging systems, complementary binary coding usually outperforms non-complementary random coding. This was first proved in [20], and further verified in [23,71,72]. Having complementary constraints in the design, a set of multi-shot aperture patterns satisfy a uniformly sensing constraint: each pixel or voxel in the scene is sensed exactly once in all collections of compressed measurements. On the other hand complementary coding affects the transmittance of the coded aperture since it is inversely proportional to the number of snapshots. This may result in a significant reduction of light throughput in the imaging system for a high number of snapshots. The polar coded aperture spectral imaging system falls into this category: a high number of snapshots (anywhere from 16 to 128 in previous simulations) is required for good reconstruction quality due to the spatial-spectrum super-resolution nature of the system. This encourages us to develop a new coded aperture design strategy that aims at uniform sensing while controlling the aperture transmittance.

Thus in this work, two coded aperture design criteria are considered. First, the data voxels should be uniformly sensed. Second, the FPA sensors should uniformly sense the data cube. The summation along the columns of the measurement matrix \mathbf{H} represents the sensing for each data voxel. The summation along the rows of \mathbf{H} represents the sensing across sensors. Thus the desired cost function breaks into two parts. The first part evaluates the non-uniformity of the sensed data voxels,

$$E_1 = \sum_{j=1}^{SRL} \left(\sum_{i=1}^{KN^2} \mathbf{H}_{ij} - m_1 \right)^2 = \sum_{j=1}^{SRL} \left(\sum_{\ell} \sum_{i=1}^{N^2} \mathbf{H}_{ij}^{\ell} - m_1 \right)^2, \quad (3.1)$$

where the data cube has the dimension of $S \times R \times L$. K snapshot measurements are captured on a $N \times N$ sensor array. \mathbf{H}_{ij}^{ℓ} is the element in the i^{th} row and j^{th} column of the ℓ^{th} snapshot sensing matrix. Here $m_1 = \text{median}(\sum_{i=1}^{KN^2} \mathbf{H}_i)$, where \mathbf{H}_i is the i^{th} row

of \mathbf{H} . The second part of the cost function measures the non-uniformity across the sensors, expressed as

$$E_2 = \sum_{i=1}^{KN^2} \left(\sum_{j=1}^{SRL} \mathbf{H}_{ij} - m_2 \right)^2 = \sum_{\ell=1}^K \sum_{i=1}^{N^2} \left(\sum_{j=1}^{SRL} \mathbf{H}_{ij}^{\ell} - m_2 \right)^2, \quad (3.2)$$

where $m_2 = \text{median}(\sum_{j=1}^{SRL} \mathbf{H}_j)$ and \mathbf{H}_j is the j^{th} column of \mathbf{H} . The cost function is then $E = E_1 + \tau E_2$, where the parameter τ has its value around SRL/KN^2 .

We apply the direct binary search (DBS) algorithm [75,76] to solve this minimization problem. DBS algorithm has been proven to be an efficient algorithm in solving binary matrix related optimization problems [71]. This iterative algorithm scans every pixel in the coding pattern and performs toggling and swapping operations between each binary pixel and its eight neighbors. It evaluates the changes of the cost function for each operation and only keeps the certain operation that results in the highest reduction of the cost function. These sequential operations guarantee the convergence of the cost function to its local minimum. However, slow computing speed becomes the main drawback. The cost function value, or more efficiently, the changes of the cost function value need to be calculated for each valid toggle and swap operation. Thus the algorithm can be highly accelerated by simplifying the cost function calculation. In the following paragraphs, a simplified cost function is derived and an efficient DBS algorithm is proposed.

The matrix \mathbf{W}^{ℓ} represents the polar-rectangular transformation. Its entry \mathbf{W}_{ij}^{ℓ} represents the percentage of the j^{th} polar pixel in coded aperture covered by i^{th} sensor. It's assumed that the sensor array is large enough to sense all polar pixels. Thus the elemental summation in each column is 1, $\sum_{i=1}^{N^2} \mathbf{W}_i^{\ell} = \mathbf{1}$. Then,

$$\begin{aligned} \sum_{\ell=1}^K \sum_{i=1}^{N^2} \mathbf{H}_{ij}^{\ell} &= \sum_{\ell=1}^K \sum_{i=1}^{N^2} \mathbf{W}_i^{\ell} \mathbf{P}_j^{\ell} = \sum_{\ell=1}^K \left(\sum_{i=1}^{N^2} \mathbf{W}_i^{\ell} \right) \mathbf{P}_j^{\ell} \\ &= \sum_{\ell=1}^K \mathbf{1} \mathbf{P}_j^{\ell} = \sum_{\ell=1}^K \sum_{c=1}^{SR} \mathbf{P}_{cj}^{\ell}. \end{aligned} \quad (3.3)$$

The matrix \mathbf{P}^{ℓ} is a concatenation of L diagonal matrices, where L is the number of

spectral bands. Thus,

$$\begin{aligned}
E_1 &= \sum_{j=1}^{SRL} \left(\sum_{\ell=1}^K \sum_{c=1}^{SR} \mathbf{P}_{cj}^{\ell} - m_1 \right)^2 \\
&= \sum_{k=1}^L \sum_{r=1}^R \sum_{s=1}^S \left(\sum_{\ell} t_{sr}^{\ell} c_{srk}^{\ell} - m_1 \right)^2.
\end{aligned} \tag{3.4}$$

Therefore, E_1 can be calculated directly from the spectral filtering c_{srk}^{ℓ} and the aperture code t_{sr}^{ℓ} . Matrix \mathbf{W}^{ℓ} has no influence on E_1 . Thus the matrix multiplication $\mathbf{W}^{\ell} \mathbf{P}^{\ell}$ is unnecessary, simplifying the calculation.

Imager rotation occurs between each snapshot. Relative to the imager, the polar voxels of the scene are circularly shifting between snapshots. This leads to a permutation in the columns of the measurement matrix for each snapshot. Mathematically the ℓ^{th} snapshot measurement matrix \mathbf{H}^{ℓ} can be calculated from permutation on column indexes j of the $(\ell - 1)^{\text{th}}$ snapshot measurement matrix $\mathbf{H}^{\ell-1}$. Thus the summations along columns of the measurement matrices in two different snapshots are the same, i.e., $\sum_{j=1}^{SRL} \mathbf{H}_{ij}^{\ell} = \sum_{j=1}^{SRL} \mathbf{H}_{ij}^{\ell-1}$. Thus the second part of the cost function can be simplified as

$$\begin{aligned}
E_2 &= K \sum_{i=1}^{N^2} \left(\sum_{j=1}^{SRL} \mathbf{H}_{ij}^1 - m_2 \right)^2 = K \sum_{i=1}^{N^2} \left(\sum_{j=1}^{SRL} \mathbf{W}_i^1 \mathbf{P}_j^1 - m_2 \right)^2 \\
&= K \sum_{i=1}^{N^2} \left(\mathbf{W}_i^1 \left(\sum_{j=1}^{SRL} \mathbf{P}_j^1 \right) - m_2 \right)^2.
\end{aligned} \tag{3.5}$$

Defining the vector $\mathbf{p} = \sum_{j=1}^{SRL} \mathbf{P}_j^1$, gives

$$\begin{aligned}
E_2 &= K \sum_{i=1}^{N^2} \left(\mathbf{W}_i^1 \mathbf{p} - m_2 \right)^2 \\
&= K \|\mathbf{W}^1 \mathbf{p} - m_2\|_2^2,
\end{aligned} \tag{3.6}$$

where a matrix-vector multiplication $\mathbf{W}^1 \mathbf{p}$ replaces the calculation of the matrix multiplication $\mathbf{W}^{\ell} \mathbf{P}^{\ell}$ K times.

Besides simplifying the cost function, the optimization algorithm itself can be designed more efficiently for faster computation. As the DBS algorithm performs local searches sequentially across all coded aperture pixels, only a small portion of pixels are

affected by each local search. However, computing E_1 and E_2 requires operations on all aperture pixels, resulting an inefficient computation strategy. Instead of computing E_1 and E_2 for each swap and toggle operation, an efficient algorithm should compute the updates of E_1 and E_2 , only involving the affected pixels in the recalculation.

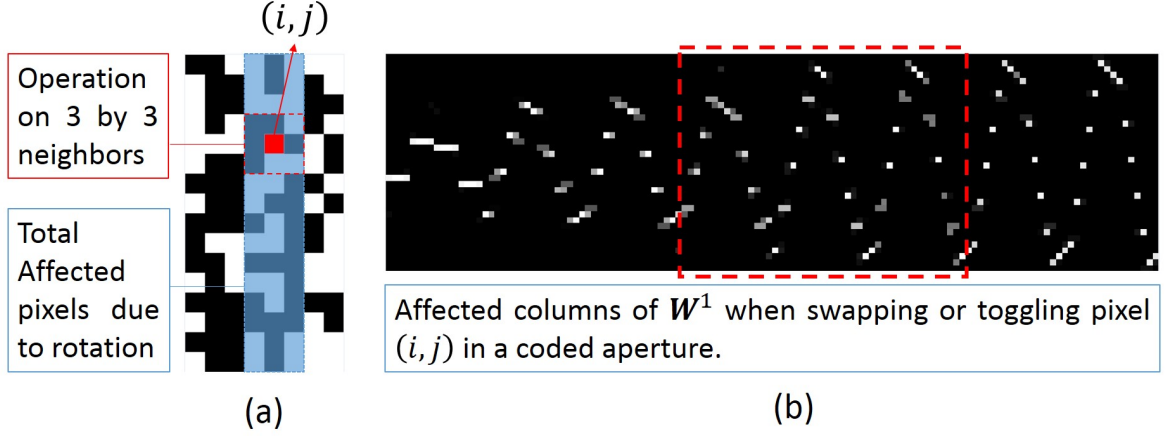


Figure 3.1: (a) shows the affected region by swapping and toggling operations to one pixel. The corresponding affected columns in \mathbf{W}^1 is shown in (b).

As an example, a polar coded aperture with 8 rings and 16 spokes are organized in a matrix $\mathbf{T} \in \mathbb{R}^{16 \times 8}$ as shown in Figure 3.1 (a). The toggling and swapping operations to the red pixel affect its neighbors in a 3x3 region during a single snapshot. the rotation of the polar coded aperture during multiple snapshots is transferred into the circular shift of \mathbf{T} along its vertical dimension. Thus, a region as large as 16x3 marked in blue is affected during the entire measurement process. Denote this affected region as Ω . Then the affected values in E_1 is

$$(E_1)_\Omega = \sum_{k=1}^L \sum_{r, s \in \Omega} \left(\sum_{\ell} t_{sr}^{\ell} c_{srk}^{\ell} - m_1 \right)^2. \quad (3.7)$$

Denote $(E_1)'_{\Omega}$ as the first part of the cost function value in region Ω after one swapping or toggling operation. Then E_1 is updated as

$$E'_1 = E_1 - (E_1)_\Omega + (E_1)'_{\Omega}. \quad (3.8)$$

The calculation of E_2 focuses on the computing of $\mathbf{W}^1 \mathbf{p}$. Note each column of \mathbf{W}^1 represents the sensing process for the corresponding aperture pixel \mathbf{T}_{sr} . Thus the

affected columns in \mathbf{W}^1 are easily picked out via the pixel region Ω , as shown in Figure 3.1 (b). The indexes of these columns are collected in a vector \mathbf{u} . Denote $\mathbf{W}_{\mathbf{u}}^1 = \{\mathbf{W}_i^1 | i \in \mathbf{u}\}$ as the matrix containing all the affected columns of \mathbf{W}^1 , and $\mathbf{p}_{\mathbf{u}}$ as the collection of the corresponding elements in \mathbf{p} . Then the affected second part of the cost function is

$$(E_2)_{\mathbf{u}} = K \|\mathbf{W}_{\mathbf{u}}^1 \mathbf{p}_{\mathbf{u}} - m_2\|_2^2. \quad (3.9)$$

Similarly, denote $(E_2)'_{\mathbf{u}}$ as the corresponding update of $(E_2)_{\mathbf{u}}$ after one swapping or toggling operation. Then E_2 is updated as

$$E'_2 = E_2 - (E_2)_{\mathbf{u}} + (E_2)'_{\mathbf{u}}. \quad (3.10)$$

With the updated E'_1 and E'_2 , the cost function value E' is updated with the weighted sum. The corresponding toggling or swapping operation is kept when $E' < E$ and the cost function reaches the greatest reduction. A new iteration begins after the algorithm operations on all coded aperture pixels. The algorithm terminates when no operation is accepted during the previous iteration, indicating that a local minimum has been obtained.

It should be pointed out that this optimization algorithm is sensitive to the initial binary pattern for the following two reasons: First, the DBS is an iterative algorithm searching for a local minimum. Secondly the median values m_1 and m_2 are calculated based on the initial sensing matrix \mathbf{H} . More specifically, the median values are related with the transmittance of the coded aperture, where transmittance of a binary coded aperture is defined as $\sum_{i,j} \mathbf{T}_{ij} / SR$ with a range from 0 and 1. A random binary coded aperture with 50% open has a transmittance of 0.5. A lower transmittance coded aperture leads to a sparser sensing matrix with smaller m_1 and m_2 values. This provides us the flexibility to control the transmittance of the optimized coded aperture by treating the transmittance of the initial coded aperture as a parameter. Thus the optimization algorithm should be run a number of times, initialized with random coded apertures with varying amounts of transmittance. This will result in optimized patterns

with various levels of transmittance, which can then be downselected by measuring simulated reconstruction performance.

3.3 Computer Simulations

A polar data cube with 16 spectral bands are used in the simulations. The coded aperture has 20 inner rings with 128 inner spokes and 54 outer rings with 256 outer spokes. 64 snapshot measurements are simulated by the discrete rotation model with 75% compression. The corresponding \mathbf{W}^1 and \mathbf{P} are calculated and used for coded aperture optimization. Figure 3.2 shows a comparison of the initial random coded aperture with 0.12 transmittance and the code pattern after optimization, where a white dot represents an unblock polar pixel and the black pixels are blocked.

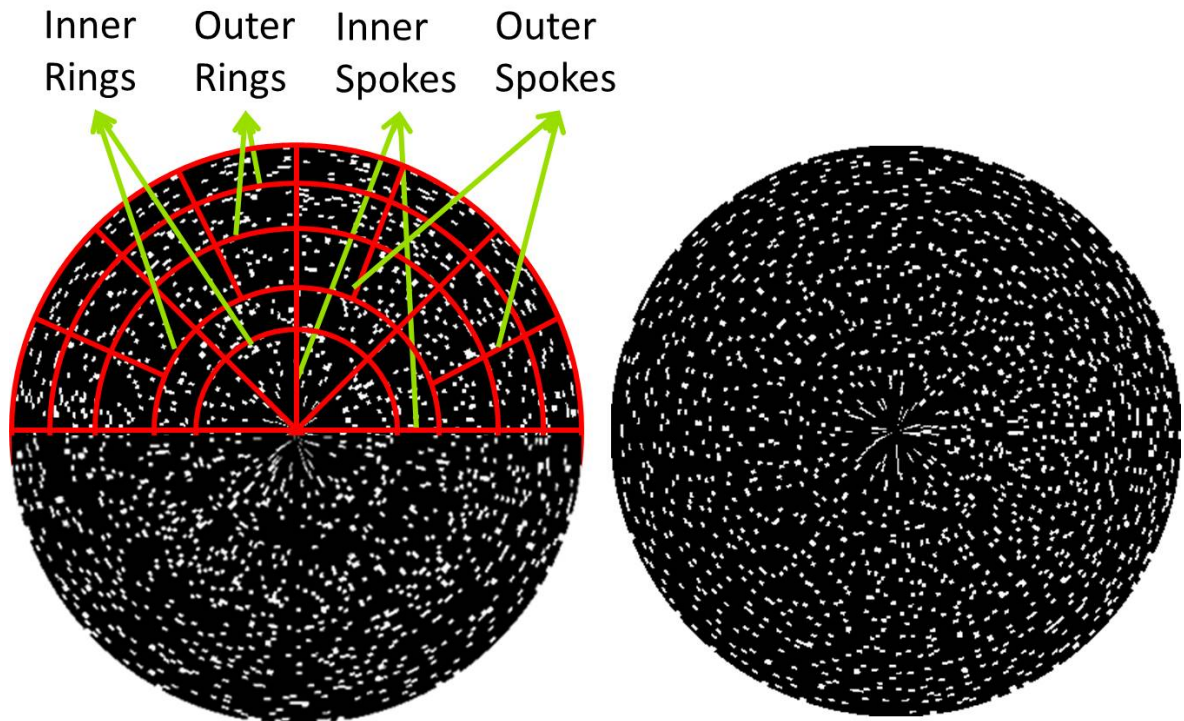


Figure 3.2: The optimized coded aperture (right) is compared with the initial random coded aperture (left) with 12% unblock pixels.

Note that the optimized coded aperture has the unblocked pixels more separated than the random one, indicating that uniform sensing is achieved. This result also aligns with other work showing that blue noise coding patterns improve reconstruction

quality. For further verification, Figure 3.3 shows the probability distribution of image cube voxels and sensors in the sensing process with both the initial random code and the optimized pattern. The two sub-figures in the upper row show the histograms of the number of sensors sensing one data voxel, while the other two histograms in the lower row count the number of voxels sensed by one sensor. The histogram comparison shows a significant improvement in the uniformity of both the data voxels and the sensors after the optimization process.

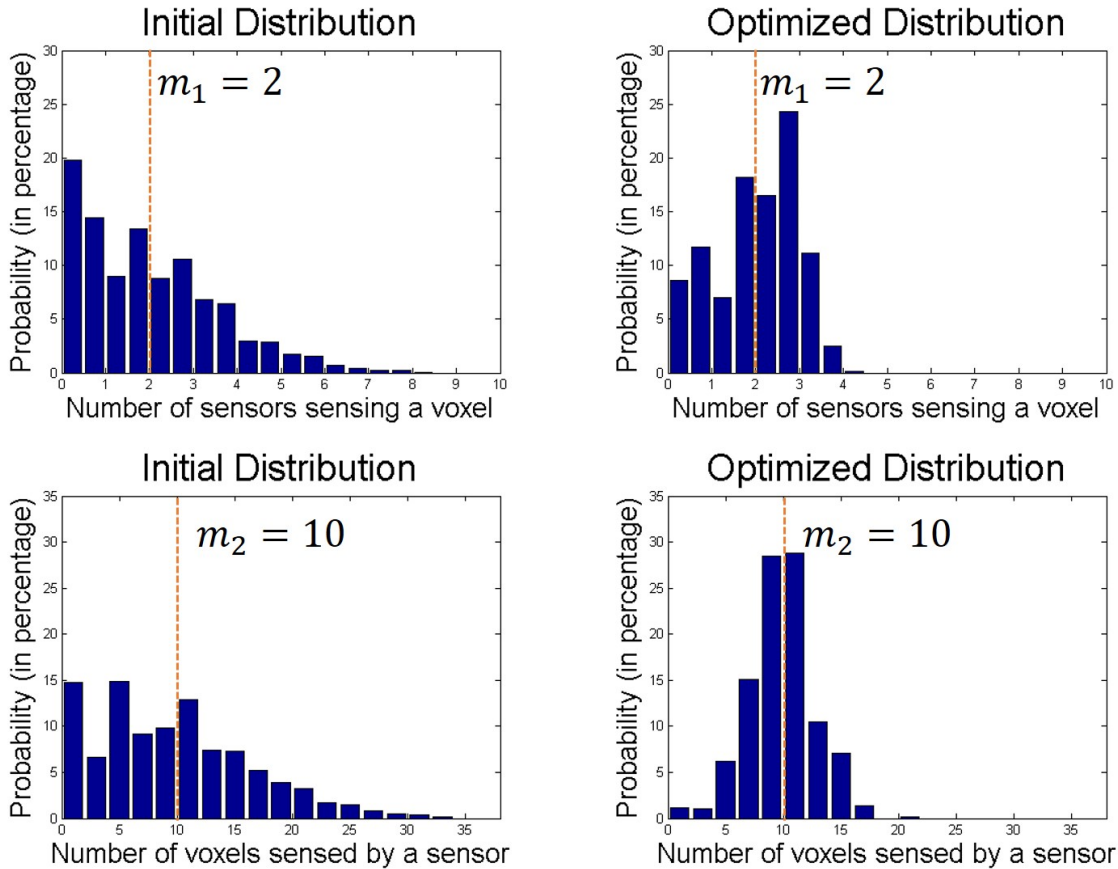


Figure 3.3: Comparison of the statistics before (left column) and after (right column) optimization. Upper row shows the histogram of the number of sensors sensing one voxel. Lower row shows the histograms of the number of voxels sensed by a certain sensor.

To quantify the improvement of the measurement matrix, singular value decomposition (SVD) is performed on both random and optimized measurement matrices. For better comparison, the top 500 singular values are normalized and plotted in Fig. 3.4. The singular values of the optimized measurement matrix decays much slower

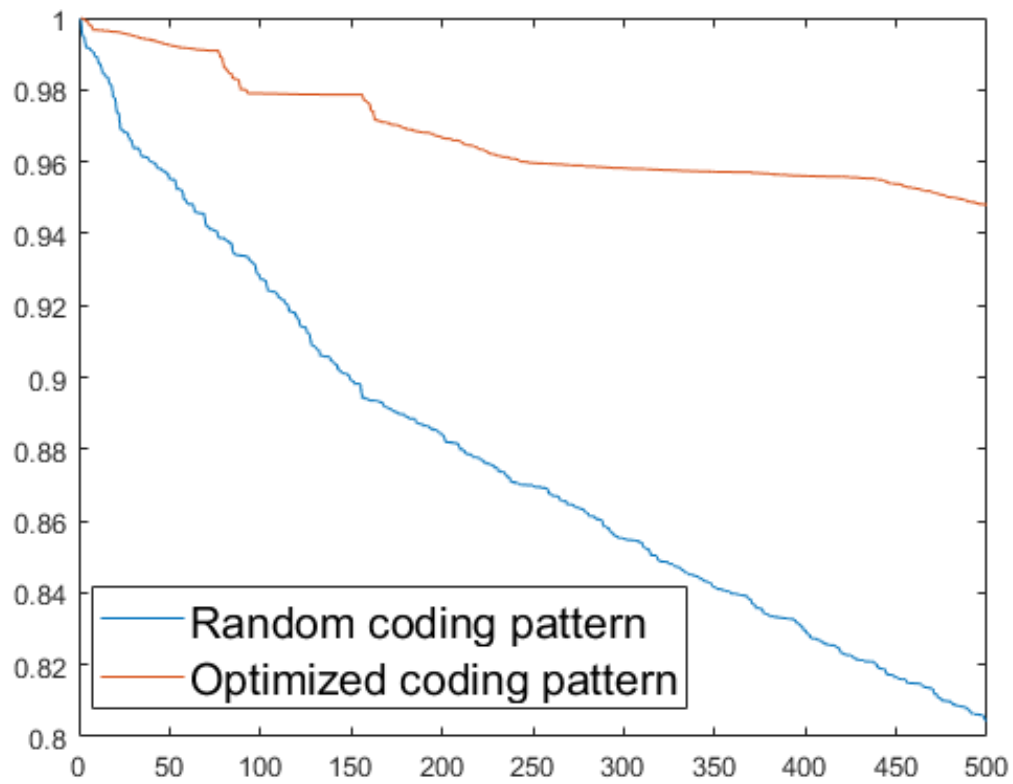


Figure 3.4: Singular values of the measurement matrices before and after optimization are plotted. Coded aperture optimization leads to a better conditioned measurement matrix.

than the non-optimized one. This indicates that our polar coded aperture optimization results in a better-conditioned measurement matrix. For these top 500 singular values, the condition numbers are 1.24 before optimization, and 1.05 after optimization.

For further performance evaluation of the proposed coded aperture optimization approach, reconstructions are performed from simulated measurements. To analyze the influence of aperture transmittance, a set of random coded apertures with transmittance ranging from 0.06 to 0.4 are used as the initial patterns for optimization. Simulations are performed for all optimized code patterns with the corresponding peak-to-noise ratio (PSNR) calculated as shown in Fig. 3.5. Based on the research in the last chapter, 0.5 transmittance is optimal for the random codes. Thus the performance of the random aperture code with 0.5 transmittance is plotted as the baseline. The PSNR of the random aperture code is the average of five repeated simulations. Optimized patterns with different initial transmittance all show reconstruction improvement compared with random patterns. The optimized coded aperture with a 0.12 initial transmittance is chosen for the best performance. Since the initial transmittance determines the median values m_1 and m_2 in the optimization process, the resulting transmittance of the optimized coding maintains the same as the initial one. For this 64 snapshot simulation, the optimal transmittance suggested by complementary coding is $1/64$. Notice that our new resulting transmittance 0.12 is much larger.

Random coded apertures with both 0.12 and 0.5 transmittance are compared with the attained optimized aperture code. Figure 3.6 shows this comparison through computing the PSNR for each spectral band. Aligned with previous research, the random code with 0.5 transmittance outperforms the random patterns with lower transmittance. The optimized aperture code achieves an average PSNR increase of 1.8dB compared with 0.5-transmittance random coded aperture. Here we select the 6th spectral band with the PSNR difference of 1.7dB to show the average improvement. Then, the 10th spectral band is selected with 3.1dB PSNR increase to illustrate the highest reconstruction improvement.

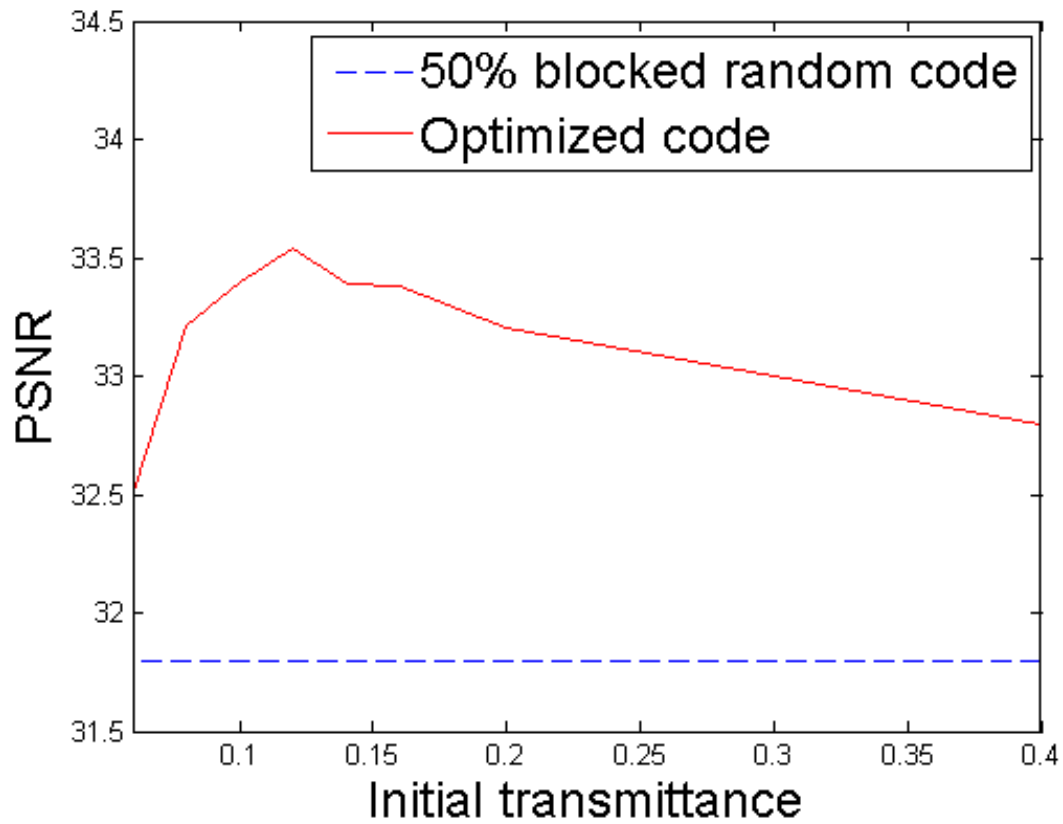


Figure 3.5: Reconstruction performance of a set of optimized aperture codes with initial transmittance ranging in $[0.06, 0.4]$. The performance of a 50% random code is plotted as a reference.

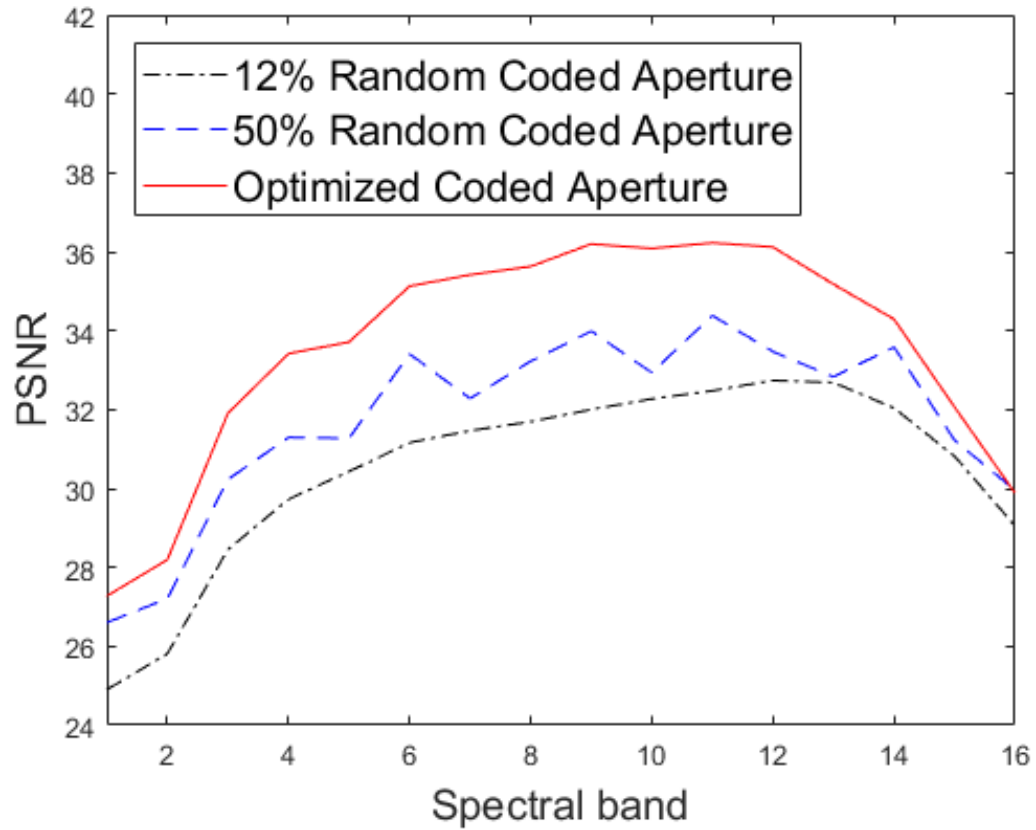


Figure 3.6: Simulations with 12% unblocked random code, 50% blocked random code and the optimized code are performed. PSNR values are computed for each reconstructed spectral image plane. Comparisons show a significant PSNR increase when the optimized coding is used.

Figure 3.7 shows the comparison of the 6th reconstructed spectral image plane. Since it is visually difficult to distinguish the reconstructions, the corresponding absolute error (AE) is calculated for each pixel and displayed in Fig. 3.7 (d) and (e). Figure 3.8 further shows the comparison of the 10th band reconstruction. The absolute errors are reduced significantly in this band.

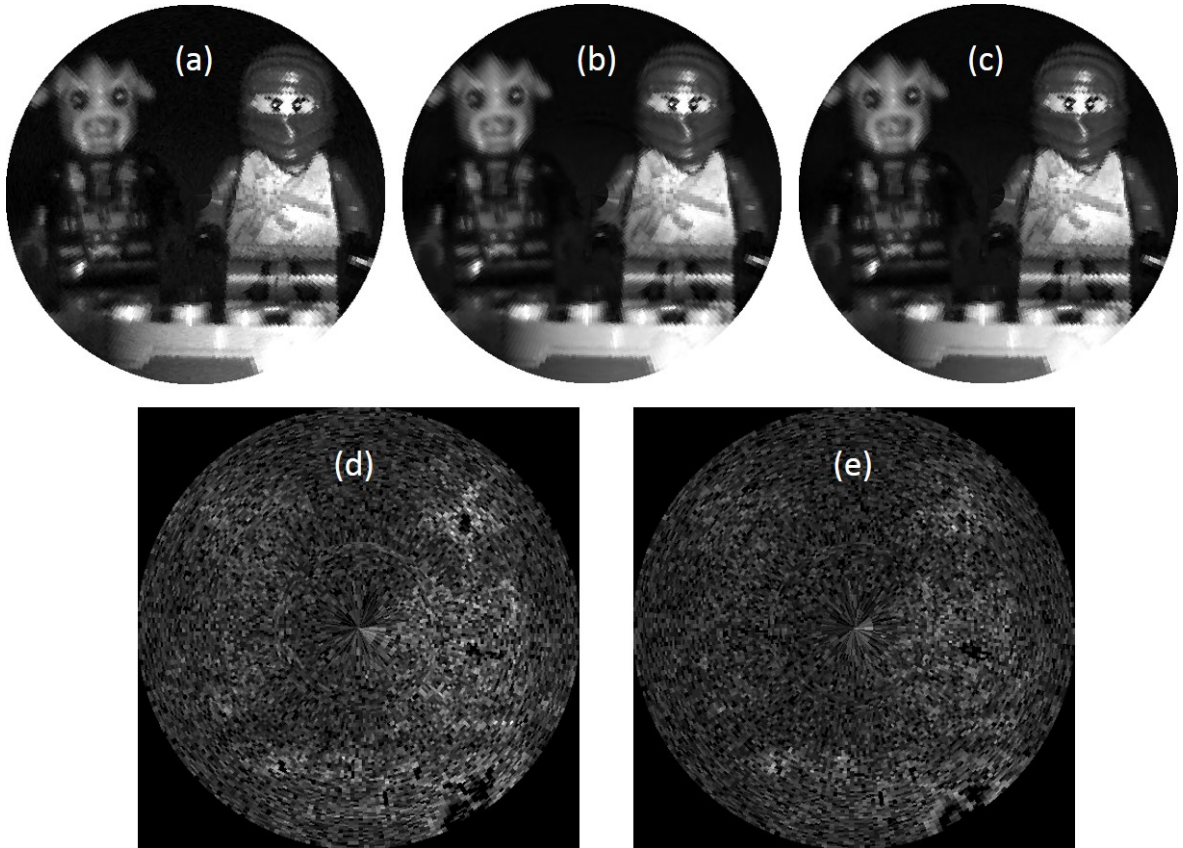


Figure 3.7: Comparison among the original 6th spectral band in (a), the reconstructed spectral band with random aperture code in (b) and the reconstructed image plane after optimization in (c). Their reconstruction absolute error image planes are shown in (d) and (e), respectively.

The optimization algorithm is also evaluated by performing simulations with different numbers of snapshots. Table 3.1 shows the comparison of reconstruction PSNR between the optimized code and a random code with 0.5 transmittance. Larger numbers of snapshots provide more flexibility to achieve uniformly sensing across the data cube voxels, leading to better optimization results. When 128 snapshots are measured, a 2.4dB PSNR improvement is achieved after optimization. However when less than 32

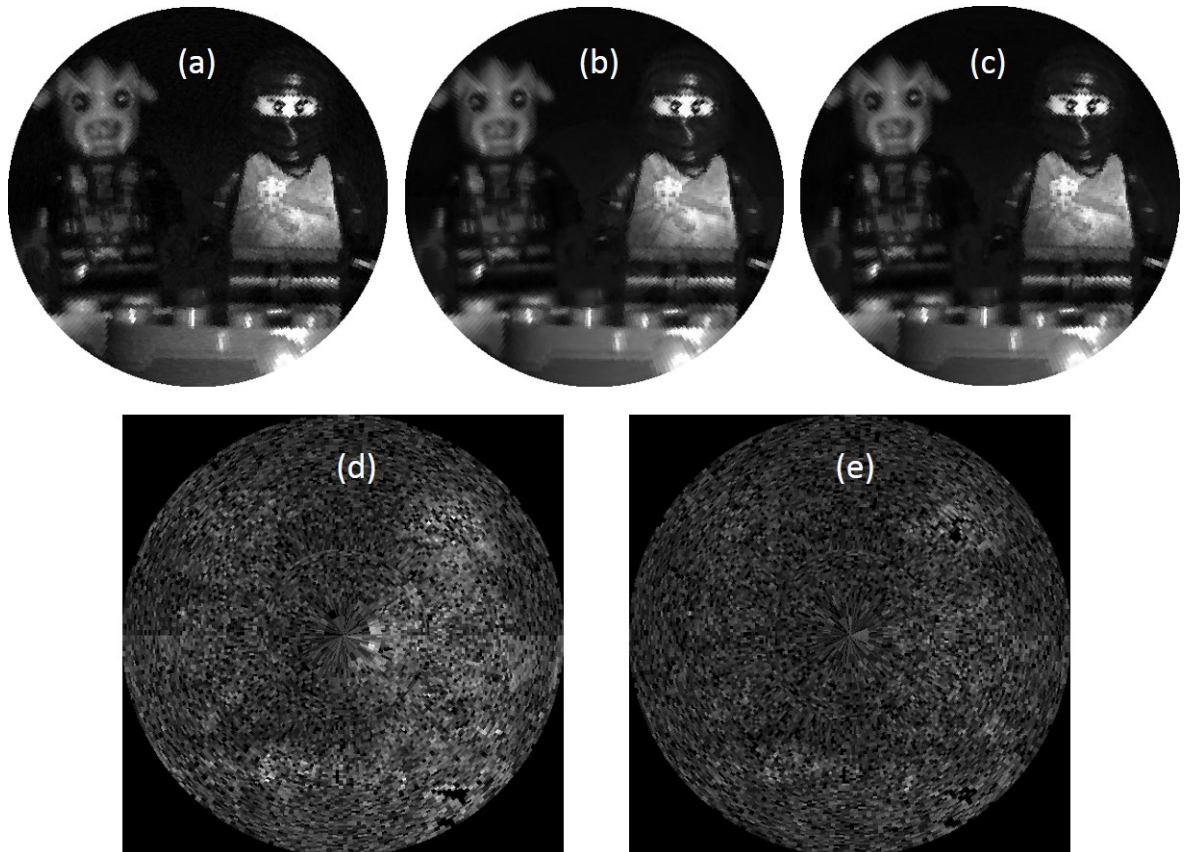


Figure 3.8: Comparison among the original 10th spectral band in (a), the reconstructed spectral band with random aperture code in (b) and the reconstructed image plane after optimization in (c). Their reconstruction absolute error image planes are shown in (d) and (e), respectively.

snapshots are used, no significant reconstruction improvement is observed. The performance variation with different numbers of snapshots is related to the flexibility of the aperture code design. A larger number of snapshots makes it easier for the algorithm to find an aperture pattern that obeys the uniform sensing criteria.

Table 3.1: PSNR comparison between random aperture code and optimized code reconstruction with different numbers of snapshots.

Number of shots	Compression	Random PSNR	Optimized PSNR	Improvement
32	87.5%	28.9dB	29.5dB	0.6dB
64	75%	31.8dB	33.5dB	1.7dB
128	50%	33.6dB	36.0dB	2.4dB

3.4 Experimental Validation

A 4inch photo-mask containing random and optimized polar coded apertures is designed and fabricated through lithography, as shown in Fig. 3.9. Each coded pattern is 5.0176mm by 5.0176mm containing a total of 128^2 polar pixels. In the experiments, this photo-mask is mounted on a M-VP-25XA Metric Precision Compact Linear Stage for vertical movement control. The vertical linear stage is then mounted on a Thorlabs LTS Long Travel Stage for horizontal movement control. A proof-of-concept experiment is then performed in laboratory.

The spectral imaging system is built in the laboratory. A one-inch achromatic doublet AC254-100-A-ML is used as the objective lens. Another achromatic doublet AC254-050-A-ML is used as a relay lens. The fabricated photo-mask is placed in the focal plane of the objective lens. The image of one coded aperture is then imaged by a Ximea MQ042RG-CM monochrome camera with 1280 by 1024 resolution and a pixel size of 4.8 micrometers, as shown in Fig. 3.10. The imaging system was proposed to be mounted on spinning munitions or other rotating platforms. However in the testbed experiments, rotating the imaging system is fairly difficult. Instead, we mount the imaging target on a Thorlab motorized rotation stage PRM1Z8 to emulate the system spinning as shown in Fig. 3.11. In the experiments, up to 64 rotations are performed during a 2π period. A Ximea monochrome imaging sensor array is used to

Fabricated coding mask

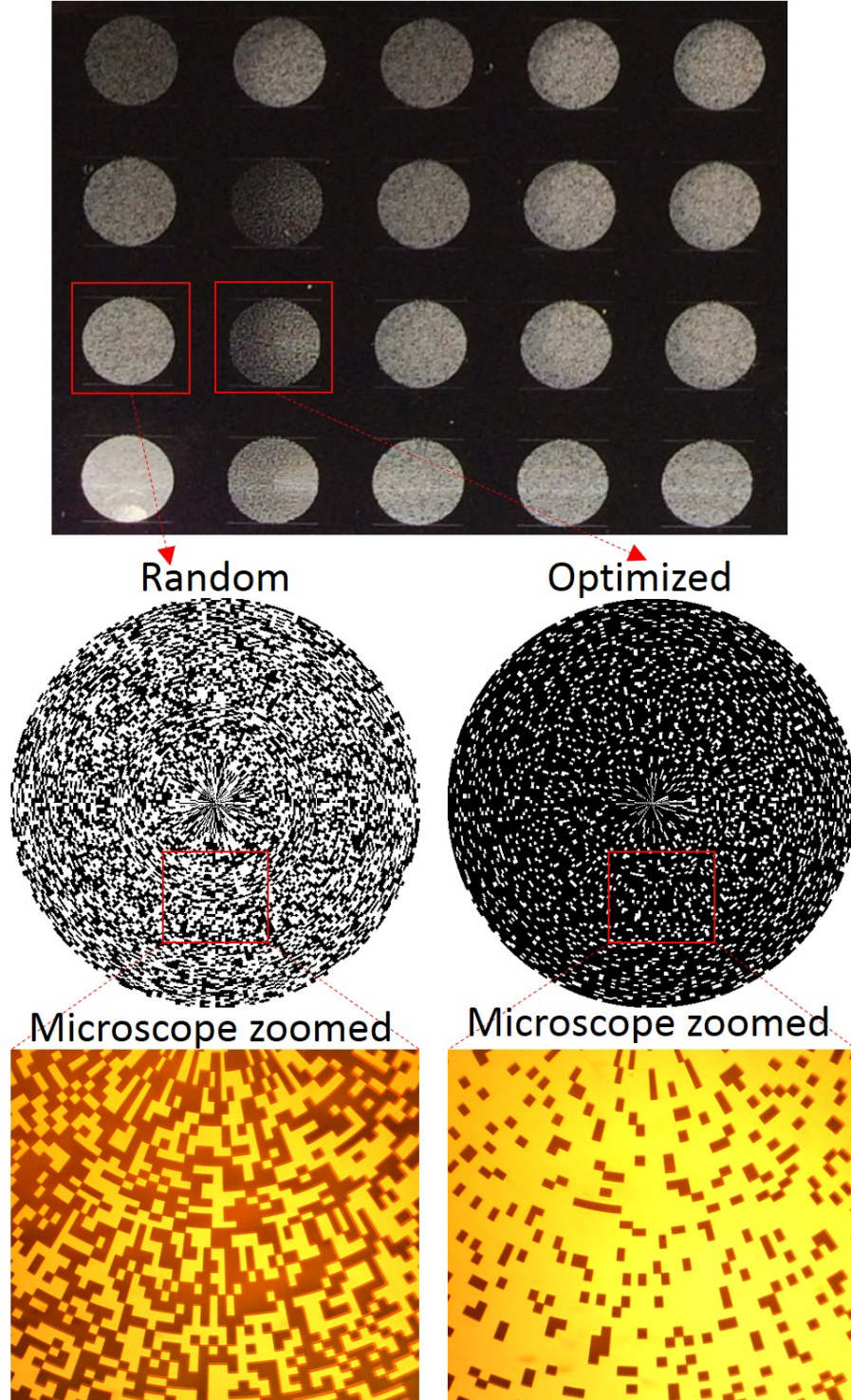


Figure 3.9: Designed photo-mask containing random and optimized polar coding patterns. Microscope zoomed images of two coding patterns are displayed.

capture the compressive measurements. Low resolution measurements are generated through a pixel grouping process after high resolution images are captured. In the experiments, we group every 16 by 16 sensor pixels to reduce a 512×512 captured image to a 32×32 measurement shot. Note that this process is only for the purpose of validating the spatial super-resolution capability of the proposed imaging system. In practice, one can always pair the existing imaging sensor with a higher resolution polar coded aperture for super-resolution purpose. Finally the circular variable filter is emulated using Edmund 10nm-wide visible bandpass filters.

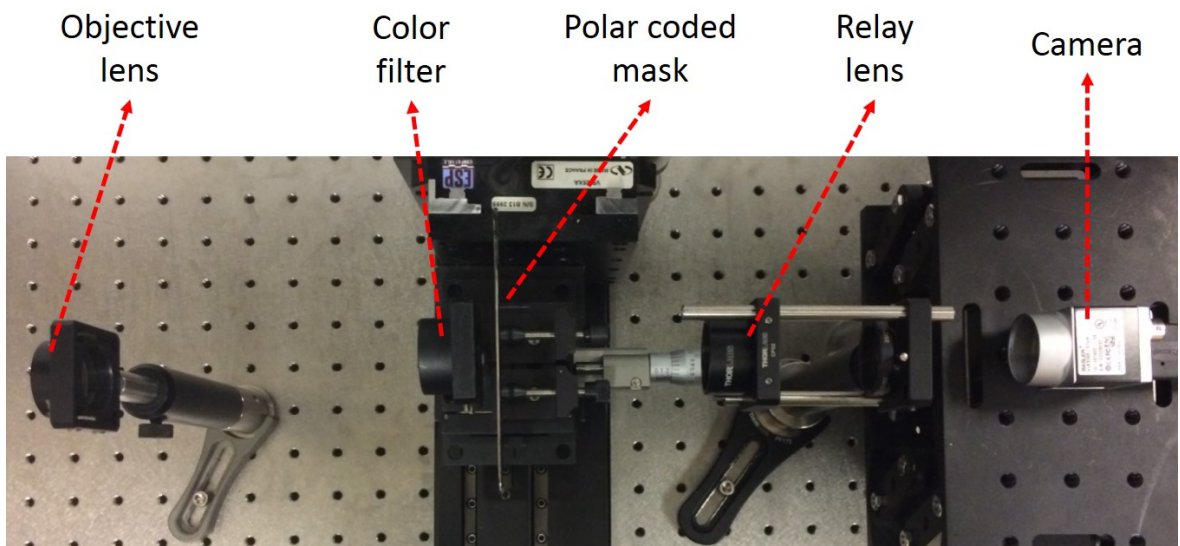


Figure 3.10: Polar coded aperture compressive spectral imaging system consists of an objective lens, a polar coded aperture on a photo-mask, a CVF emulated with bandpass color filters, a relay lens and a monochrome sensor array.

Optical alignment is critical to coded aperture imaging systems. The alignment becomes even more important when a rotation motion is involved during measurement collection. To address this, two electrical-controlled nano-positioners are used to alter the coding patterns on the photo-mask, and align each pattern with the sensor array. The rotation of the target is characterized through the measurement of the relative position of the rotation center to the sensors. This is performed through tracing the movement of several object points during a 2π rotation. In order to emulate the

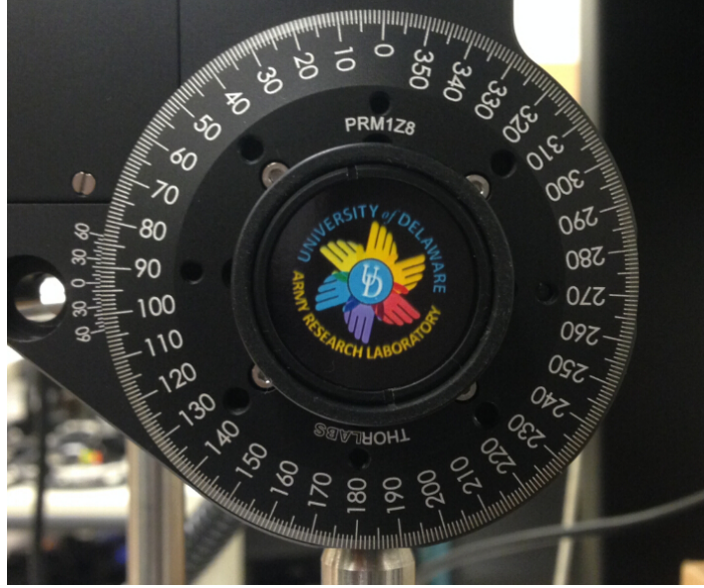


Figure 3.11: Target mounted on a motorized rotation stage.

spinning of the imaging system, this rotation center was aligned to the center of each polar coding pattern.

Another critical procedure in compressive imaging systems is the calibration of the entries of measurement matrix \mathbf{H} . The calibration includes illuminating a white board with monochrome illuminations in the visible range. The images of the polar coded aperture are first captured on the sensor, then mapped back into polar pixels. Figure 3.12 shows a comparison of the calibrated polar pattern with the ideal binary coding. The goal of this calibration is to account for the optical misalignment, lens distortion and vignetting compensation. The polar patterns, as well as the spectral response of the system, are used to construct the forward matrix \mathbf{H} for the experimental imaging system which is required to reconstruct the spectral image cube.

The measurement acquisition process is automated through a computer. The camera captures the encoded compressed images of the target during its 64 rotations in a 2π period. The images are collected and sub-sampled into a set of low resolution (32×32) measurements. Then these low resolution measurements are used to reconstruct the spectral images through solving the inverse problem of its sensing matrix. Figure 3.13 shows the target and 4 low resolution snapshot measurements.

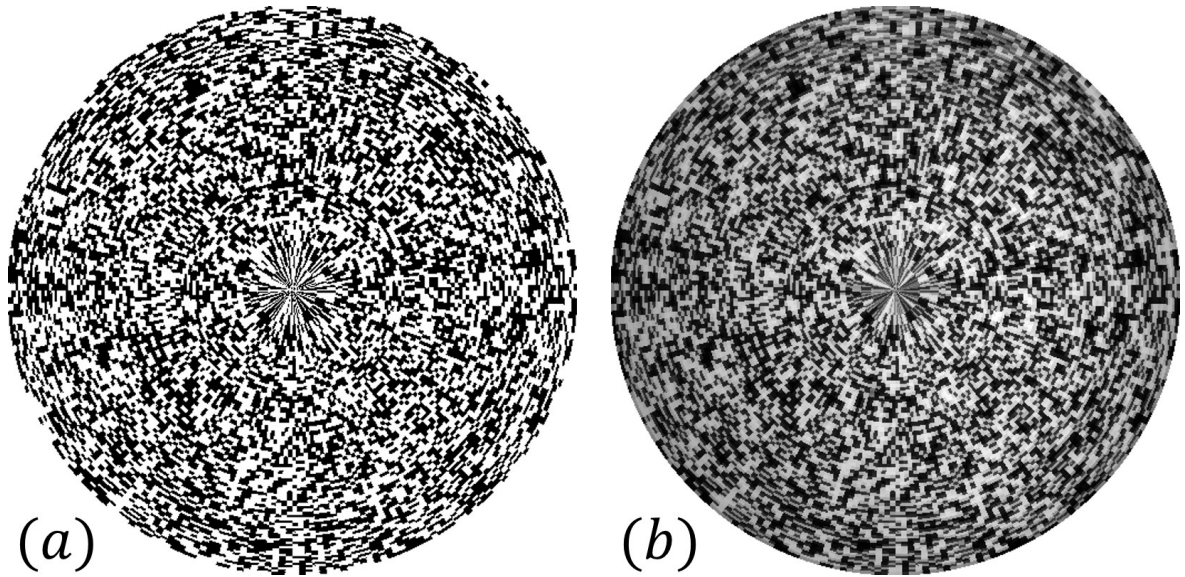


Figure 3.12: (a) The ideal binary polar pattern with 128^2 polar pixels. (b) The calibrated polar pattern from the experimental imaging system. Optical distortion and vignetting compensation is considered by using the calibrated coding pattern in the reconstruction.

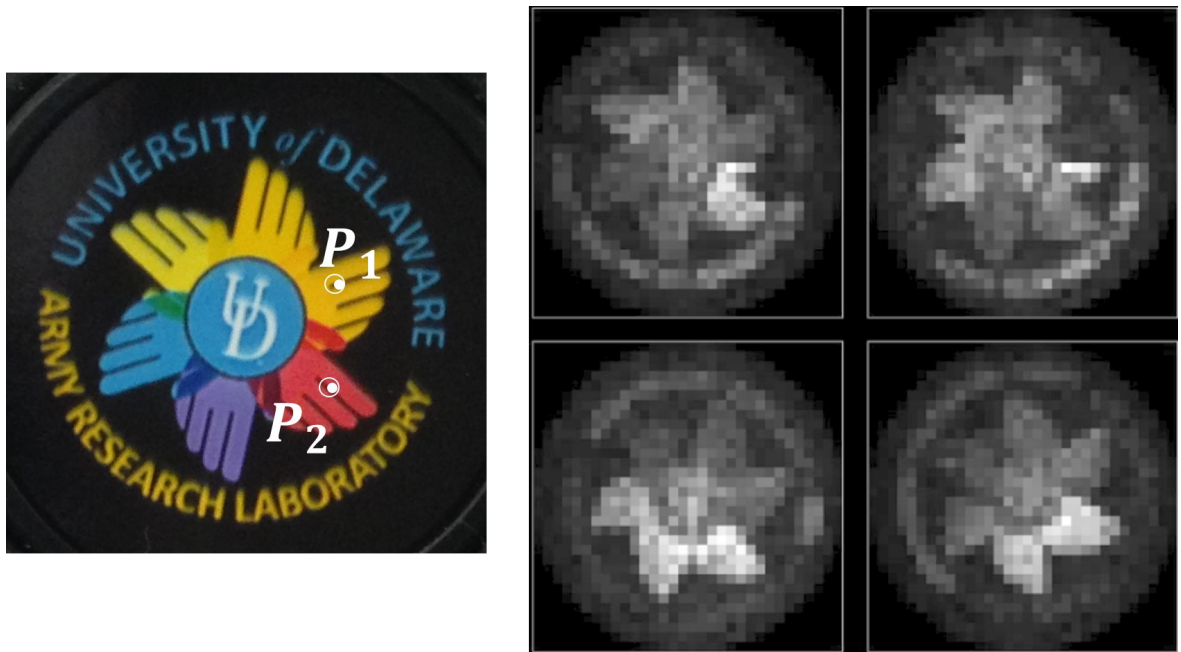


Figure 3.13: An RGB image of the imaging target is shown in the left figure. The right figures are four low-resolution measurement images captured and down-sampled from the experimental imaging system.



Figure 3.14: A total 16 spectral image bands are reconstructed from 64 low resolution measurements. The spectral range is from 500nm to 650nm. 9 of the 16 spectral bands are selected for display.

Here we reconstruct 16 spectral bands with a 128^2 pixel spatial resolution. For a comparison, both 50% random coding and the optimized pattern are tested. Figure 3.14 shows 9 of the total 16 spectral bands reconstructed from random encoded compressed measurements. The spectral variation of the colored hands is clearly shown and the words “Army Research Laboratory” can be recognized in most of the bands. The UD logo in the center can be somewhat recognized with distortion, indicating the performance in the center pixels is less than the outer pixels. This could be a result of the misalignment of the rotation center and inaccuracy during the mapping from square sensor pixels to polar coding pixels.

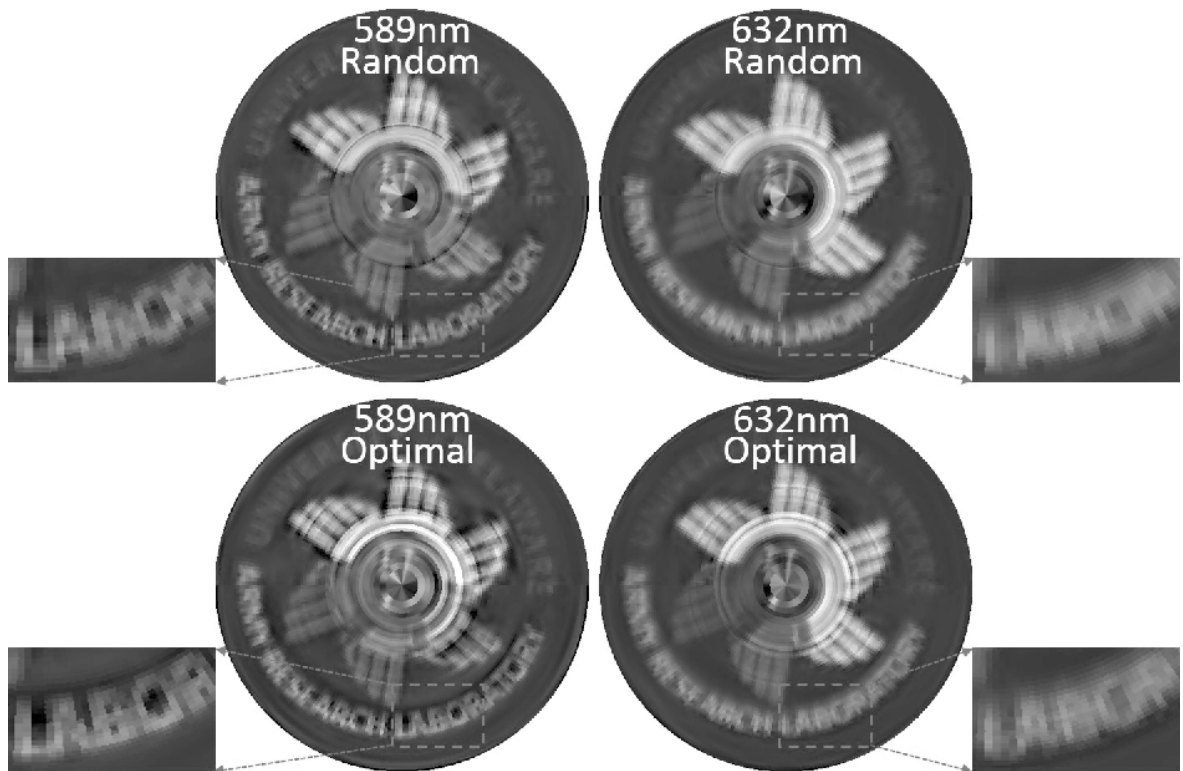


Figure 3.15: Comparison of random (top) and optimized (bottom) reconstructions. Letters “LABOR” are enlarged for a detailed comparison. The optimized coding pattern resolves letters “BOR” more clearly than random coding patterns in both bands.

Figure 16 shows a comparison between two reconstructed spectral bands from random and optimized encoded measurements. The optimized coding pattern performs better at resolving details, such as words. In this example, the letter “B” is better

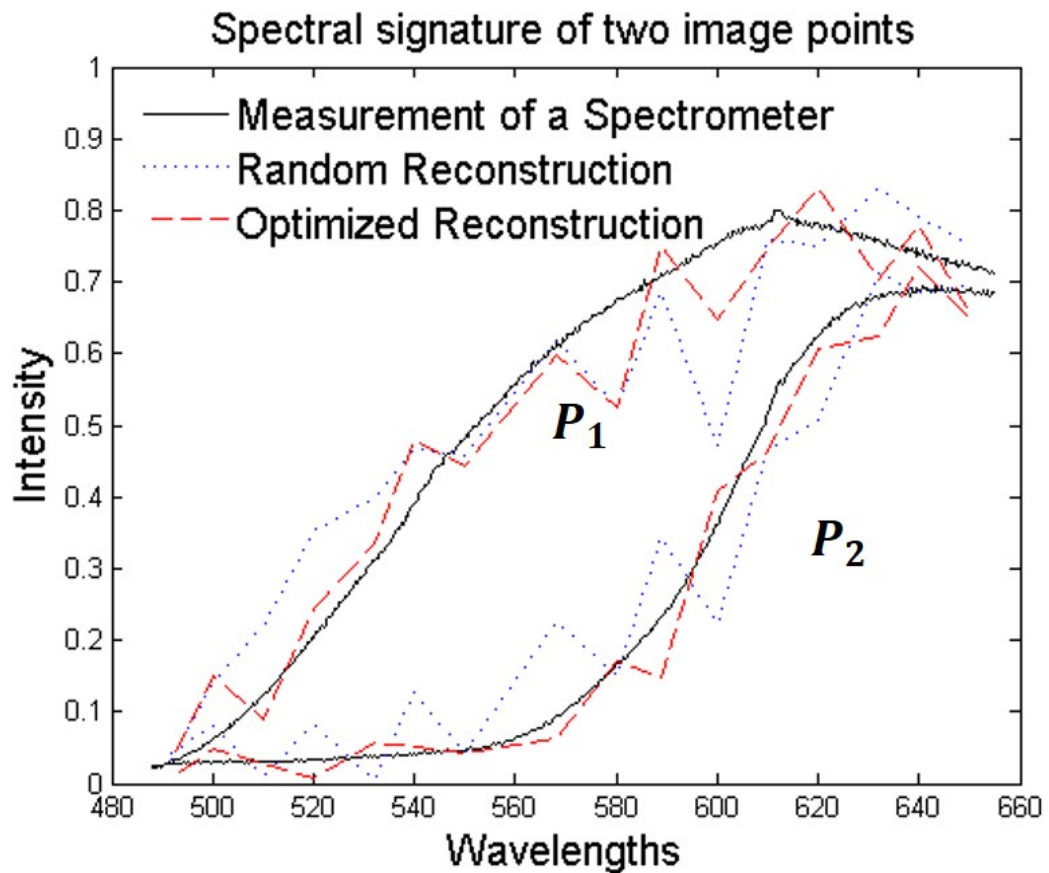


Figure 3.16: Spectral signatures of points P_1 and P_2 on the target shown in Fig. 3.15 are experimental measured through a spectrometer. The spectrometer measurements are then compared with the reconstructions using random and optimized coded apertures. The optimized spectral reconstructions fit the spectrometer measurements better.

resolved. The recovery of the spectrum is compared in Fig. 3.16 where the spectral signature of two image points P_1 and P_2 shown in Fig. 3.13 are selected for comparison. The spectral recovery from the optimized coding pattern follows the spectrometer measurements tighter. PSNR values are calculated for these two spectral signatures. The reconstructions from random coded measurements achieve 20dB in PSNR for point P_1 , and 25dB for P_2 . The optimized reconstruction for P_1 is improved to 23dB, while the PSNR of P_2 increases to 28.5dB.

3.5 Conclusion

The optimization framework for a polar coded aperture compressive spectral imaging system is developed through the design of the block-unblock coding pattern of a polar coded aperture. By performing the coded aperture optimization, uniform sensing is achieved across the image cube and the sensor array. The optimized binary coding breaks the complementary limitations with a control of light transmittance. Computer simulation shows the optimized coded aperture introduces a significant improvement in the reconstruction quality. The polar coded apertures are then fabricated on a photo-mask using lithography. A proof-of concept experiment is further conducted. The alignment and calibration procedures are described and spectral image planes are successfully reconstructed from experimental measurements. Better spatial and spectrum reconstructions are achieved using the optimized polar coded aperture.

Chapter 4

COMPRESSIVE SPECTRAL POLARIZATION IMAGING BASED ON A PIXELATED POLARIZER

In this chapter, a compressive spectral and polarization imager based on a pixelized polarizer and colored patterned detector is presented. The proposed imager captures several dispersed compressive projections with spectral and polarization coding. Stokes image planes at several wavelengths are reconstructed directly from 2D projections. Employing a pixelized polarizer and colored patterned detector enables compressive sensing over spatial, spectral, and polarization domains, reducing the total number of required measurements. Polarization and color coding patterns are specially designed to enhance PSNR in the reconstructed images. Experiments validate the architecture and reconstruction algorithms.

4.1 Introduction

Spectral imaging involves the sensing of a large amount of spatial information across a multitude of wavelengths. Spectral sensors enable the estimation of the physical properties of targets and the distribution of material components across the scene [77]. In addition, polarimetric imaging provides information about the surface features of targets, such as roughness and orientation [2]. Together, spectral polarization imaging (SPI) is achieved by measuring polarization images across the spectral wavelengths with applications in classification [78], remote sensing [2], and biomedical diagnosis [79].

The major challenge in SPI is the acquisition of the hyper-dimensional imaging data across spatial, spectral and polarization dimensions. Typical spectral and polarization imagers capture sequential measurements, such as scanning the scene in

each dimension [77], or switching colored filters [80] and rotating polarizers [81]. The long acquisition time and mechanical switching increase the acquisition noise and limit performance in a dynamic scene. Alternatively, division of focal plane (DoFP) [82-84] schemes are widely used in both spectral imaging and polarimetric imaging. In spectral imaging, colored mosaic focal plane array (FPA) detectors are used to capture the specific spectral wavelengths in each pixel [85]. In polarimetric imaging, micropolarizer arrays are used to acquire pixelated polarization intensity [86,87]. In DoFP methods, the spatial resolution is reduced in order to obtain both spectral and polarization signatures [88].

Compressive sensing, on the other hand, overcomes the resolution limitation of DoFP schemes by fully utilizing the FPA resolution. By using compressive sensing, far fewer samples are needed and consequently the sensing speed is increased significantly. The hyper-dimensional data cube can then be reconstructed from the compressive projections.

A single-pixel polarimetric imaging spectrometer was proposed recently, enabling acquisition of spatial, spectral and polarization information of the scene from compressive measurements [27]. This architecture utilizes a DMD as a spatial light modulator. A spectral polarization analysis is achieved by combining a rotating polarizer with a spectrometer. However, compressive sensing is only applied in the spatial domain, whereas full spectral and polarization information is obtained. Besides, thousands of sequential measurements are needed for decent reconstructions. As discussed in Chapter 1, other existing compressive spectral polarization imaging systems suffers from either low spectral resolution or insufficient polarization resolution [28,29].

In this chapter, a new compressive spectral polarization imaging architecture is presented. The proposed architecture, consisting of a rotating prism, a pixelized polarizer and colored detector, obtains spatial, spectral and polarization information of the scene from just a few compressive measurements. As described in Chapter 1, the polarization is mathematically represented by Stokes parameters, and we acquire Stokes

parameter images of the scene in multiple spectral channels. Utilizing an FPA detector, compressive sensing in the spatial, spectral and polarization domains is achieved, with reduced acquisition time. Furthermore, a rotating prism combined with a static polarization and color patterned detector enables new spectral and polarization coding in each snapshot, resulting in more efficient sensing strategies than the DMD-based coded aperture compressive sensing cameras.

In the proposed architecture illustrated in Fig. 4.1, the scene is first dispersed by the prism along its wavelength components. The wavelength dispersed scene is then encoded by polarization and colored patterns and finally integrated on the detector. In this way, a single 2D compressed measurement shot embodies spatial, spectral and polarization information. Multiple snapshots are captured by rotating the dispersive element if more accuracy in the polarization signatures is needed.

From the compressive measurements, a hyper-dimensional image cube is recovered by applying compressive sensing theory. This new architecture combines the advantages of DoFP with compressive measurements and reconstruction. The use of the polarized and colored FPA avoids switching colored filters or rotating linear polarizers during the measurement process, thus reducing the acquisition time. Compressive sensing theory guarantees the full utilization of the patterned FPA resolution. As we will show, the polarized and colored patterns are specially designed to improve the reconstruction accuracy. Laboratory measurements with an optical system are used to validate the proposed imager and algorithms to reconstruct spectral and polarization information of the scene.

This chapter is organized as follows: In Section 2, the mathematical model of the compressive sensing architecture is presented. In Section 3, code design is introduced followed by a reconstruction comparison from simulated measurements in Section 4. Multi-shot acquisition via prism rotation is described in Section 5. Finally, testbed experiments are presented in Section 6.

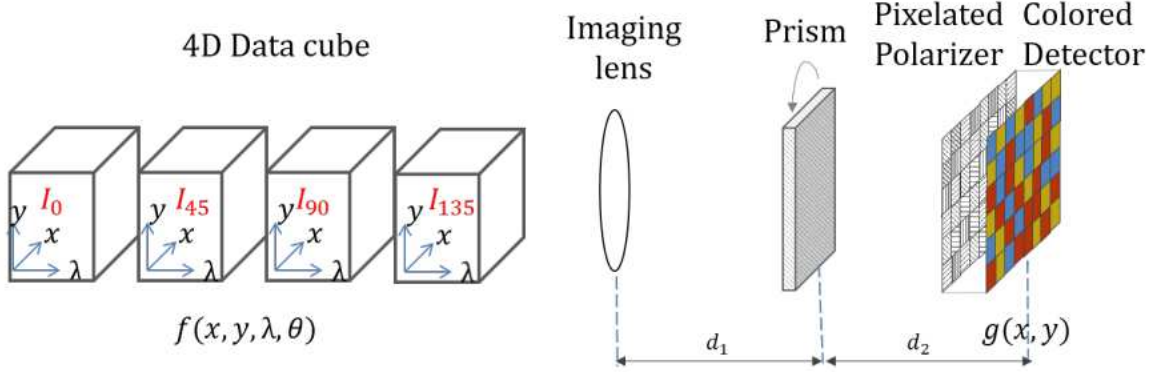


Figure 4.1: Proposed compressive spectral polarization imaging system consisting of an objective lens, a colored detector with micropolarizer array aligned, and a prism. Multi-snapshots are achieved by prism rotation.

4.2 Spectral Polarization Compressive Sensing System

The proposed spectral polarization compressive imaging architecture is shown in Fig. 4.1. The scene is represented as polarization intensity cubes with four angles of polarization (0° , 45° , 90° and 135°). A micropolarizer array [89] is a filter array composed of small aperture polarizers. Each micropolarizer consists of wire grid structures at one of the four angular orientations, as shown in Fig. 4.2. The colored filter FPA employs recent thin film coating technology, that encodes the scene in the spectral domain. While the use of a dispersive element further increases the spectral resolution.

We denote the scene as a 4D data cube $f(x, y, \lambda, \theta)$, where x and y represent the two spatial dimensions, λ is the spectral wavelength, and θ represents the angles of linear polarization. After dispersion by the prism along its spectral dimension, the 4D data cube is represented as

$$f_1(x, y, \lambda, \theta) = \iint \delta(x' - (x - d_x(\lambda)), y' - y) f(x, y, \lambda, \theta) dx' dy', \quad (4.1)$$

where $d_x(\lambda)$ is the dispersion distance along the x coordinate and δ denotes the Dirac delta function. After dispersion by the prism, the optical field is coded by the micropolarizer array and the colored filter array before being integrated at the FPA. The

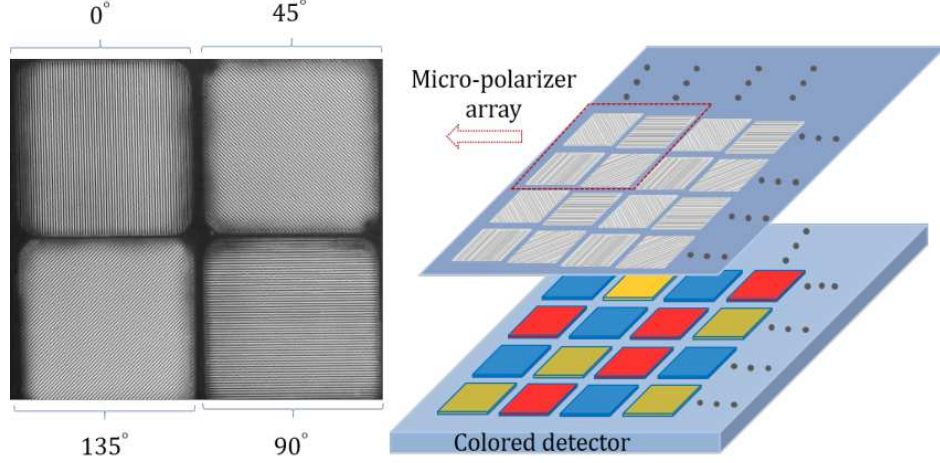


Figure 4.2: A micropolarizer array consisting of four angles of polarization is aligned to the colored detector with the same pixel pitch.

coded dispersed data cube prior to the FPA is represented as

$$f_2(x, y, \lambda, \theta) = U(x, y, \theta)T(x, y, \lambda)f_1(x, y, \lambda, \theta), \quad (4.2)$$

where $T(x, y, \lambda)$ is the spectral coding provided by the colored (lowpass, highpass, bandpass) filter array; and $U(x, y, \theta)$ is the polarization coding of the micropolarizer array. The micropolarizer array shares the same pixel size as both the colored filter array and the FPA. Ideally, both the T and U functions are binary, representing either blocking or unblocking a voxel in the 4D datacube. In practice, a calibration process is applied to account for the non-ideal optical elements.

Finally, the dispersed and coded scene is integrated on the FPA, forming a 2D projection $g(x, y)$ given by

$$\begin{aligned} g(x, y) &= \iint T(x, y, \lambda)U(x, y, \theta)f_1(x, y, \lambda, \theta)d\lambda d\theta \\ &= \iint T(x, y, \lambda)U(x, y, \theta) \\ &\quad f_0(x - d_x(\lambda), y, \lambda, \theta)d\lambda d\theta. \end{aligned} \quad (4.3)$$

The linear polarization information is fully represented by the first three Stokes parameters, which are obtained by sensing four linear polarization intensities. In the proposed sensing model, the scene is viewed as four linear polarization intensity cubes

indexed by $c = 0, 1, 2, 3$ indicating cubes with four polarization angles: $\theta_0 = 0^\circ$, $\theta_1 = 45^\circ$, $\theta_2 = 90^\circ$ and $\theta_3 = 135^\circ$, respectively. Thus, the discrete 4D datacube is given by

$$f_{ijkc} = \int_{\lambda_k}^{\lambda_{k+1}} \int_{j\Delta}^{(j+1)\Delta} \int_{i\Delta}^{(i+1)\Delta} f_0(x, y, \lambda, \theta_c) dx dy d\lambda,$$

where i and j index the pixels in x and y coordinates, Δ is the pixel pitch of the FPA, and $k = 1, 2, \dots, L$ indexes the L spectral channels. The number of spectral channels is determined by the dispersive element [18]. It follows that the $(m, n)^{th}$ pixel on the FPA detector is given by

$$\begin{aligned} g_{mn} &= \int_{n\Delta}^{(n+1)\Delta} \int_{m\Delta}^{(m+1)\Delta} g(x, y) dx dy \\ &= \int_{n\Delta}^{(n+1)\Delta} \int_{m\Delta}^{(m+1)\Delta} \iint T(x, y, \lambda) U(x, y, \theta) \\ &\quad f_0(x - d_x(\lambda), y, \lambda, \theta) d\lambda d\theta dx dy. \end{aligned} \quad (4.4)$$

Since the micro-polarizer array shares the same pixel size with the colored detector, the micro-polarizer array is discretized in terms of the PFA pixel pitch Δ , yielding

$$u_{mnc} = \int_{n\Delta}^{(n+1)\Delta} \int_{m\Delta}^{(m+1)\Delta} U(x, y, \theta_c) dx dy. \quad (4.5)$$

Similarly, the colored filter array is discretized as

$$t_{mnk} = \int_{\lambda_k}^{\lambda_{k+1}} \int_{n\Delta}^{(n+1)\Delta} \int_{m\Delta}^{(m+1)\Delta} T(x, y, \lambda) dx dy d\lambda. \quad (4.6)$$

With the discrete representations in Eq. 4.5 and Eq. 4.6, the $(m, n)^{th}$ pixel on the FPA in Eq. 4.4 is then expressed as

$$\begin{aligned} g_{mn} &= \sum_{c=0}^3 \sum_{k=0}^{L-1} \int_{\lambda_k}^{\lambda_{k+1}} \int_{n\Delta}^{(n+1)\Delta} \int_{m\Delta}^{(m+1)\Delta} T(x, y, \lambda) \\ &\quad U(x, y, \theta_c) f_0(x - d_x(\lambda), y, \lambda, \theta_c) dx dy d\lambda \\ &= \sum_{c=0}^3 \sum_{k=0}^{L-1} t_{mnk} u_{mnc} f_{m-k, n, k, c}. \end{aligned} \quad (4.7)$$

Now let the measurement in Eq. 4.7 be vectorized in \mathbf{g} . Similarly, let the c^{th} linear polarization cube be vectorized in \mathbf{f}_c . Then, the proposed imager output can be written as

$$\begin{aligned} \mathbf{g} &= [\mathbf{H}_0, \mathbf{H}_1, \mathbf{H}_2, \mathbf{H}_3] [\mathbf{f}_0^T, \mathbf{f}_1^T, \mathbf{f}_2^T, \mathbf{f}_3^T]^T \\ &= \mathbf{Hf}, \end{aligned} \quad (4.8)$$

where \mathbf{H}_c is the measurement matrix of the c^{th} polarization cube, which is determined by the polarized and colored array. The vector form of the polarizer array in the k^{th} channel is

$$\mathbf{u}_c^k = [u_{0,k,c}, \dots, u_{0,1+k,c}, \dots, u_{N-1,N-1+k,c}]^T. \quad (4.9)$$

Similarly, the vector form of the color array in the k^{th} channel is given by

$$\mathbf{t}_k = [t_{0,k,k}, \dots, t_{0,1+k,k}, \dots, t_{N-1,N-1+k,k}]^T. \quad (4.10)$$

It follows that the measurement matrix \mathbf{H}_c can be written as

$$\mathbf{H}_c = \begin{bmatrix} \text{diag}(\mathbf{u}_c^0 \circ \mathbf{t}_0) & \mathbf{0}_{N \times N^2} & \cdots & \mathbf{0}_{N(L-1) \times N^2} \\ & \text{diag}(\mathbf{u}_c^1 \circ \mathbf{t}_1) & \cdots & \\ & & \ddots & \\ \mathbf{0}_{N(L-1) \times N^2} & \mathbf{0}_{N(L-2) \times N^2} & \cdots & \text{diag}(\mathbf{u}_c^{L-1} \circ \mathbf{t}_{L-1}) \end{bmatrix}, \quad (4.11)$$

where $\mathbf{u}_c^k \circ \mathbf{t}_k$ is the element-wise product of \mathbf{u}_c^k and \mathbf{t}_k . For each polarization intensity cube, the spectral coding \mathbf{t}_k is the same. However, for each spectral channel, the polarization coding \mathbf{u}_c^k changes with the spectral channel index k .

In order to visualize the matrix \mathbf{H} , consider a data cube having a spatial resolution of 6 by 6 ($N = 6$) and 3 spectral channels ($L = 3$). The polarized and colored array is assumed to be ideal (containing only 0's and 1's). An example of the sensing matrix \mathbf{H} is displayed in Fig. 4.3. The white points represent 1's, while 0 entries remain black. To show the effect of the micropolarizer array on the matrix \mathbf{H} , the colored filters are assumed to be allpass filters.

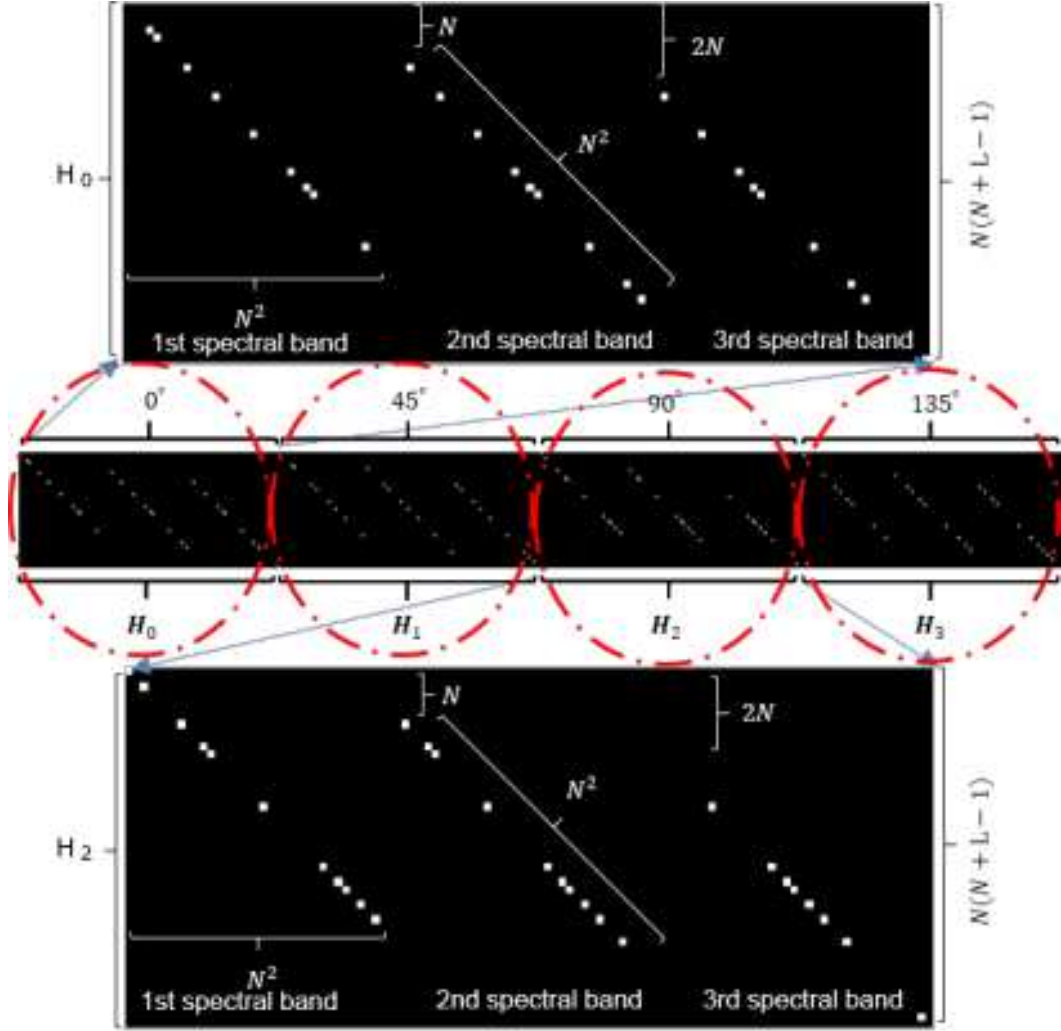


Figure 4.3: Illustrative example of the sensing matrix $\mathbf{H} = [\mathbf{H}_0, \mathbf{H}_1, \mathbf{H}_2, \mathbf{H}_3]$ for $N = 6, L = 3$. To show the influence of the micro-polarizer array \mathbf{u}_c^k , \mathbf{t}_k is assumed to be an all ones vector for each channel.

The relationship between the Stokes parameters and linear polarization intensities is explored in [90,91], where it is established that the intensity of light with the first three Stokes parameters, S_0 to S_2 , after passing through a θ° linear polarizer is given by

$$I_\theta = \frac{1}{2}S_0 + \frac{1}{2}\cos(2\theta)S_1 + \frac{1}{2}\sin(2\theta)S_2. \quad (4.12)$$

We denote each Stokes parameter cube as $s_p(x, y, \lambda)$, where $p = 0, 1, 2$ indexes the first three Stokes parameter cubes. Discretizing as before, each parameter cube can be

written

$$s_{ijkp} = \int_{\lambda_k}^{\lambda_{k+1}} \int_{j\Delta}^{(j+1)\Delta} \int_{i\Delta}^{(i+1)\Delta} s_p(x, y, \lambda) dx dy d\lambda, \quad (4.13)$$

where Δ is the pixel pitch of the FPA. With the vector representation of the first three Stokes parameter cubes \mathbf{s} , the vector representation of the c^{th} polarization intensity cube can be expressed as a linear transformation of \mathbf{s} given by

$$\mathbf{f}_c = \mathbf{E}_c \mathbf{s}, \quad (4.14)$$

where the $N^2 \times 3N^2$ matrix \mathbf{E}_c consists of three diagonal block matrices,

$$\mathbf{E}_c = [\text{diag}(\frac{1}{2}), \text{diag}(\frac{1}{2} \cos 2\theta_c), \text{diag}(\frac{1}{2} \sin 2\theta_c)]. \quad (4.15)$$

The four values of θ_c are indexed via $c = 0, \dots, 3$. Hence, the vectorized data cube \mathbf{f} is represented by

$$\mathbf{f} = \mathbf{E} \mathbf{s}, \quad (4.16)$$

where the matrix $\mathbf{E} = [\mathbf{E}_0^T, \mathbf{E}_1^T, \mathbf{E}_2^T, \mathbf{E}_3^T]^T$. Accordingly, the sensing process in Eq. 4.8 can be rewritten as

$$\mathbf{g} = \mathbf{H} \mathbf{f} = \mathbf{H} \mathbf{E} \mathbf{s} = \mathbf{G} \mathbf{s}, \quad (4.17)$$

where $\mathbf{G} = \mathbf{H} \mathbf{E}$ represents the sensing process from the Stokes parameter cube directly to a single measurement shot. Unlike the binary matrix \mathbf{H} , the entries of \mathbf{G} are $\frac{1}{2}$, 0 or $-\frac{1}{2}$. Figure 4.4 shows the ideal matrix \mathbf{G} corresponding to the matrix \mathbf{H} displayed in Fig. 4.3. In the figure, the value of $\frac{1}{2}$ is displayed in white; $-\frac{1}{2}$ is displayed in green; and the black background has the value of 0. Negative values occur when a 90° micropolarizer senses the second Stokes parameter cube. For 135° micropolarizers, the corresponding negative values occur when sensing the third Stokes parameter cube. Due to the azimuth angles of the polarizer, the intensity (S_0) reduces by half.

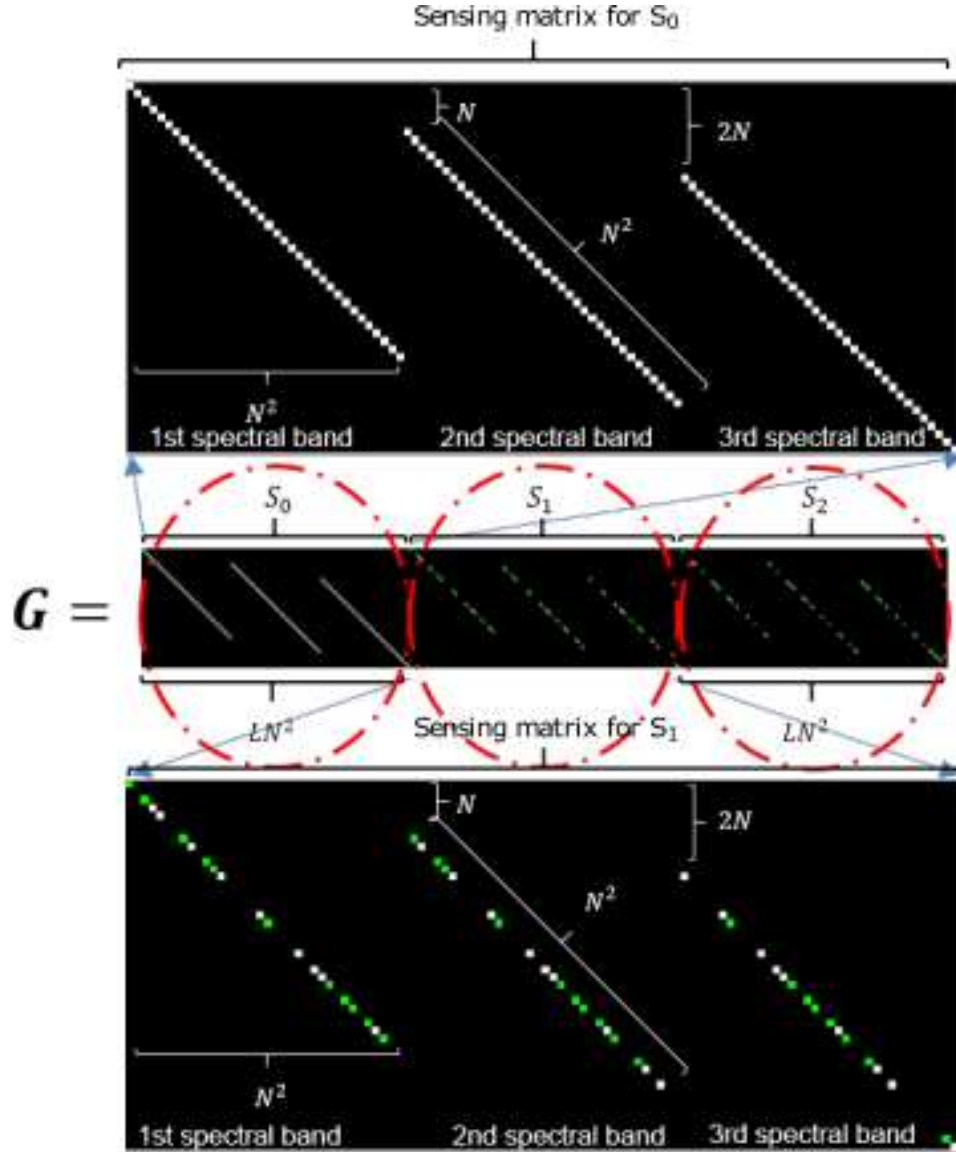


Figure 4.4: Illustrative example of matrix $\mathbf{G} = [\mathbf{S}_0, \mathbf{S}_1, \mathbf{S}_2]$ for $N = 6$, $L = 3$. The corresponding \mathbf{H} matrix is taken from Figure 3. White points have the values of $\frac{1}{2}$; green points have the values of $-\frac{1}{2}$; Black points are zero-valued entries.

To exploit the sparsity of the data cube, each Stokes parameter cube is represented by a three dimensional Kronecker basis $\Psi = \Psi_1 \otimes \Psi_2 \otimes \Psi_3$, where $\Psi_1 \otimes \Psi_2$ provides the basis in the spatial domain and Ψ_3 is the basis in the spectral domain

[18]. In this case $\mathbf{s} = \mathbf{\Psi}\boldsymbol{\theta}$, thus the sensing process can be expressed as

$$\mathbf{g} = \mathbf{G}\mathbf{s} = \mathbf{G}\mathbf{\Psi}\boldsymbol{\theta} = \mathbf{A}\boldsymbol{\theta}, \quad (4.18)$$

where $\mathbf{A} = \mathbf{G}\mathbf{\Psi}$ is the composite sensing matrix of the system. The signal is recovered by solving the inverse problem of the underdetermined linear system, that consists of recovering $\boldsymbol{\theta}$, such that the mixed l_1 - l_2 cost function is minimized. The reconstruction problem is given by

$$\hat{\boldsymbol{\theta}} = \arg \min_{\boldsymbol{\theta}} \|\mathbf{y} - \mathbf{A}\boldsymbol{\theta}\|^2 + \tau \|\boldsymbol{\theta}\|_1, \quad (4.19)$$

where τ is a regularization constant.

4.3 Design of The Micropolarizer and The Colored Filter Array

In a conventional compressive sensing scheme, random entries would be used to form the micropolarizer and colored filter array patterns. However, random binary codes tend to form clusters as shown in Fig. 4.5, which have a negative impact on reconstruction from limited shots.

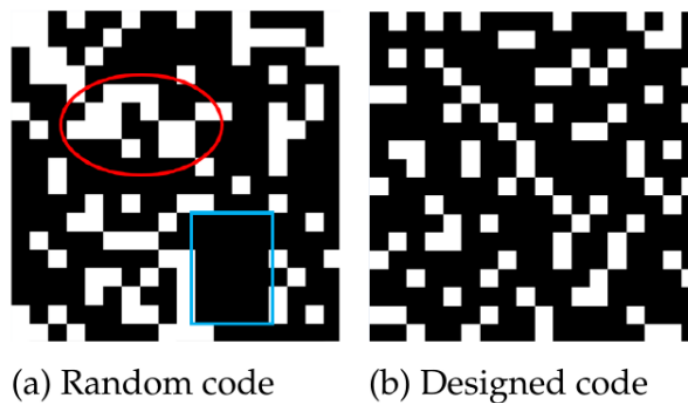


Figure 4.5: (a) A random code forms clusters. (b) The designed code reduces the clusters and achieves a more uniform sensing across the FPA.

Consider the realization of a random micropolarizer code in Fig. 4.5(a). Note that the circled area contains a high non-zero density of the micropolarizers, while, in the square area, no information for this polarization angle is sensed. It follows that poor reconstruction of the corresponding Stokes parameters is expected in the

squared area. This is typical of random realizations, and motivates the use of better code designs. As an alternative, we employ a criterion for coded pattern design that reduces the filter clusters in order to achieve a more uniform sensing across the FPA. In particular, we apply blue noise pattern synthesis [73,74] to design a binary coded array with even density in all parts of the array; an example is shown in Fig. 4.5(b). Four complementary matrices, one for each polarization angle, are designed simultaneously by selecting four blue noise patterns satisfying the constraint $\sum_{c=0}^3 u_{mnc} = 1$. This constraint aligns each PFA pixel (m, n) with a single micro-polarizer. With the same motivation, and using the same design procedure, the spatial distribution of the color filters is also represented with a set of complementary binary matrices.

4.4 Reconstruction Using Designed Coded Apertures

To study the proposed compressive sensing system, a 4D test data cube containing 4 polarization intensity cubes was obtained experimentally. In each polarization intensity cube, 8 spectral channels (500nm, 510nm, 530nm, 550nm, 580nm, 600nm, 620nm and 640nm), with 256 by 256 spatial resolution, are included. The test data cube was captured by switching eight bandpass filters combined with four azimuth angles (0° , 45° , 90° and 135°) of a linear polarizer (LPVISB100-MP2). Unpolarized illumination is applied. The polarization intensity image planes in four spectral channels are shown in Fig. 4.6, displaying a toy character covered by three pieces of polarizer film.

The linear polarization information is readily obtained using Eq. 1.1 to Eq. 1.3. The Stokes parameter imaging bands over four wavelengths are displayed in Fig. 4.7. The second and third Stokes parameters together represent the state of linear polarization. Note how the S_1 and S_2 image planes differ in the sunglasses, chest patterns and legs of the toy. With this 4D test data cube, the snapshot measurement can be simulated using Eq. 4.7 without additional noise. Assume the data cube has N^2 spatial resolution, L spectral channels and $P = 3$ Stokes parameters. The compressive sensing (CS) ratio is defined as $\kappa = KN_m/PN^2L$ with K snapshots captured, and

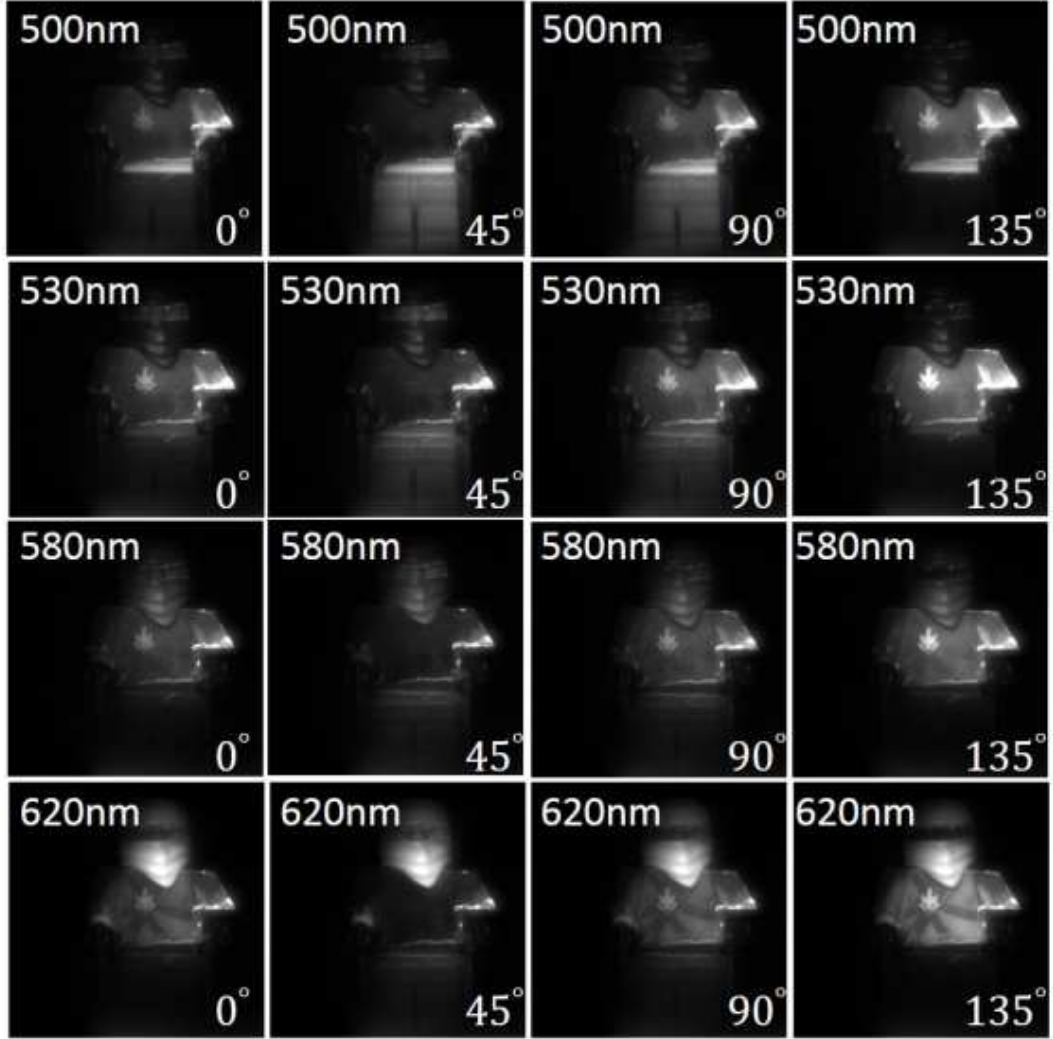


Figure 4.6: Test linear polarization intensity image planes in four spectral channels.

$N_m = (N + L - 1)N$ is the number of measurements in one snapshot. For a single-snapshot measurement in this case, the CS ratio is $\kappa = 4.3\%$.

Notice that, without applying a DoFP strategy, 32 snapshots are required including 4 rotations of a linear polarizer, combined with changing color filters 8 times, in order to obtain the 4D information of the scene. The polarization and color patterned detector, taking full advantage of the DoFP strategy, enables the acquisition of the same 4D information with a single snapshot. Note also that the DoFP, without applying compressive sensing, suffers from a resolution limitation. With an N^2

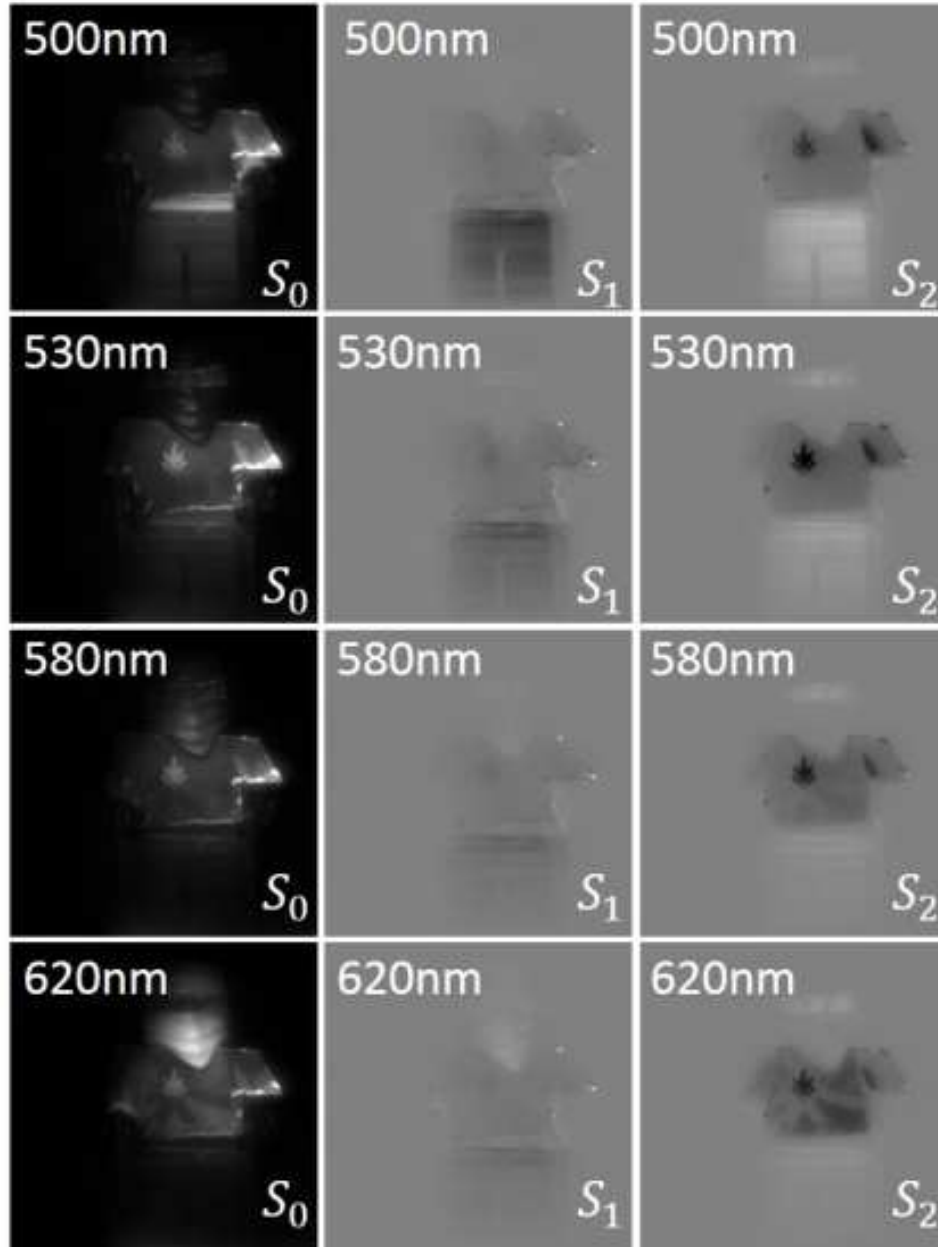


Figure 4.7: Ground truth of S_0 , S_1 and S_2 image planes. Each Stokes parameter image plane is displayed in four of eight spectral channels: 500nm, 530nm, 580nm and 620nm.

pixel detector, the spatial resolution is reduced to $N^2/32$ pixels for 4×8 spectral polarization image planes. With compressive sensing applied, the proposed imager can recover the 4D data cube with N^2 spatial resolution for each image plane, achieving full resolution. To exploit the sparsity of the scene, a 2D-Wavelet basis is applied in

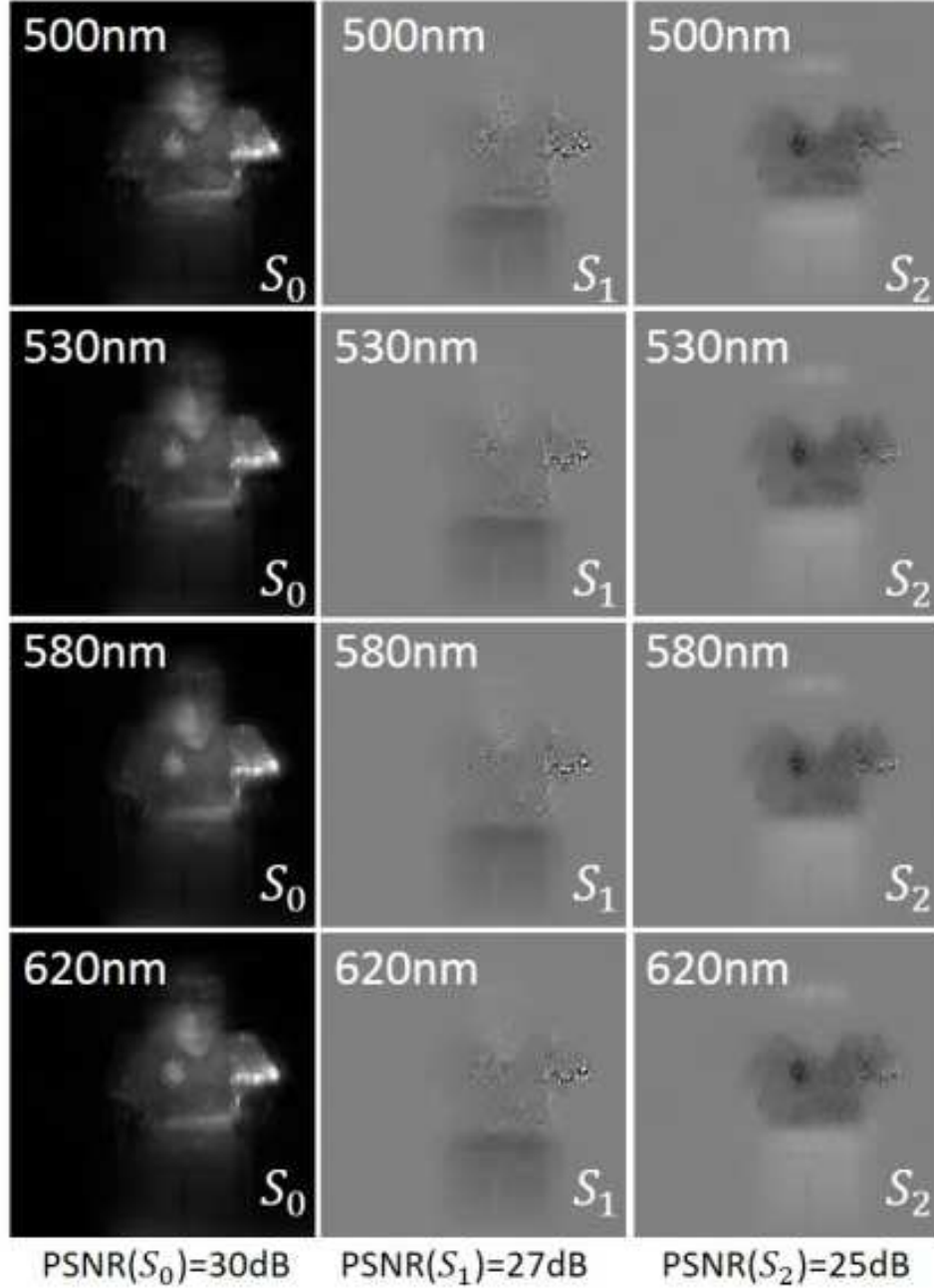


Figure 4.8: S_0 , S_1 and S_2 image planes reconstructed with single simulated shot random codes are displayed in four of eight spectral channels. The CS ratio is $\kappa = 4.3\%$. The average PSNRs for each Stokes image plane are also indicated.

the spatial domain, and the Cosine basis is used in the spectral domain for each Stokes image cube. The Stokes image planes in 8 spectral channels are reconstructed from the simulated measurement by solving Eq. 4.19 using the GPSR algorithm. PSNR

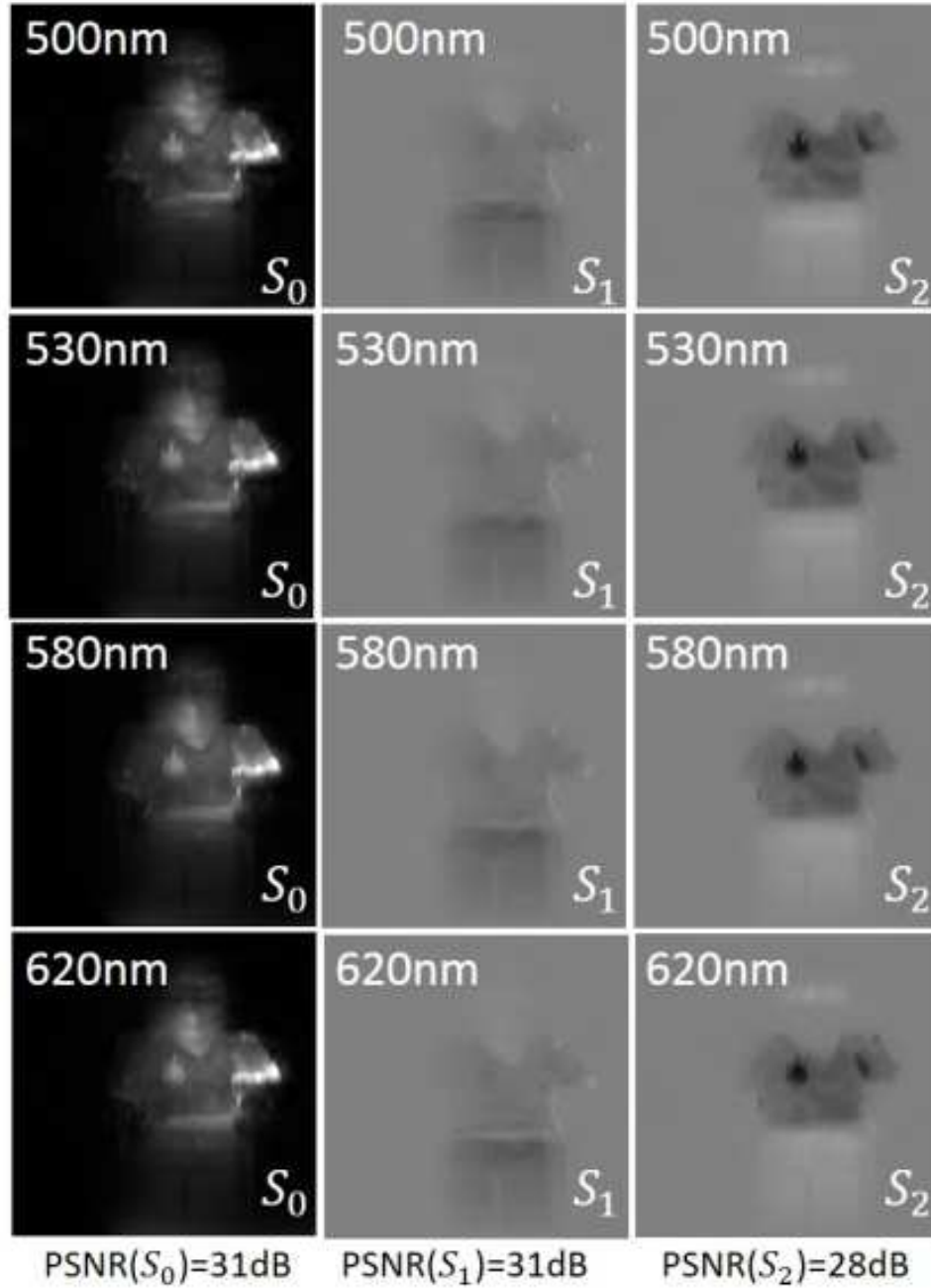


Figure 4.9: S_0 , S_1 and S_2 image planes reconstructed with a single simulated shot with designed codes are displayed in four spectral channels. The CS ratio is $\kappa = 4.3\%$. The average PSNRs for each Stokes image plane are indicated.

values of the reconstruction is calculated by comparing the image planes with the ground truth. Comparing with random compressive sensing codes, a 5 dB PSNR gain

is achieved using the blue noise code design. To visualize the reconstruction quality, the reconstructed Stokes image planes in 4 spectral channels are displayed in Fig. 4.8 and Fig. 4.9 for random and blue noise coded apertures, respectively. The results show significant improvement of reconstruction image quality with fewer artifacts.

4.5 Prism Rotation for Multi-shot Acquisition

The proposed compressive sensing imager has the ability to perform as a single-snapshot imager, with no moving parts. However, a single-snapshot compressive sensing imager typically suffers from an ill conditioned sensing matrix. Compressive sensing schemes typically rely on multiple snapshots to obtain satisfactory reconstruction quality, where each snapshot utilizes independent random coding [92]. Proposed multi-shot architectures involve moving elements, such as switching coded masks or applying a DMD. In our system new coding of the data cube is produced with prism rotation. With a single snapshot, the prism is fixed such that only horizontal dispersion occurs. Defining the single snapshot prism angle as 0° , vertical dispersion is achieved by rotating the prism to 90° or 270° . Experimentally, prism rotation was achieved by applying a precision cage rotation mount with micrometer drive (Thorlabs CRM1P). A new snapshot is taken with each prism rotation. In principle, the prism can be rotated to any angle such that any number of snapshots can be taken. In our experiments, the prism rotation is restricted to four angles: 0° , 90° , 180° and 270° .

With each rotation, spectral image planes are projected to different locations on the detector such that the same image plane is coded by different spectral polarization patterns, as shown in Fig. 4.10.

Computer simulations were performed with the multi-snapshot architecture. Four snapshots were simulated with a CS ratio of $\kappa = 17\%$. Reconstructions using the four snapshots with blue noise codes are displayed in Fig. 4.11. Compared with single snapshot reconstruction, a gain of 8dB in PSNR is observed when 4 snapshots are used in the reconstruction, demonstrating a significant performance gain.

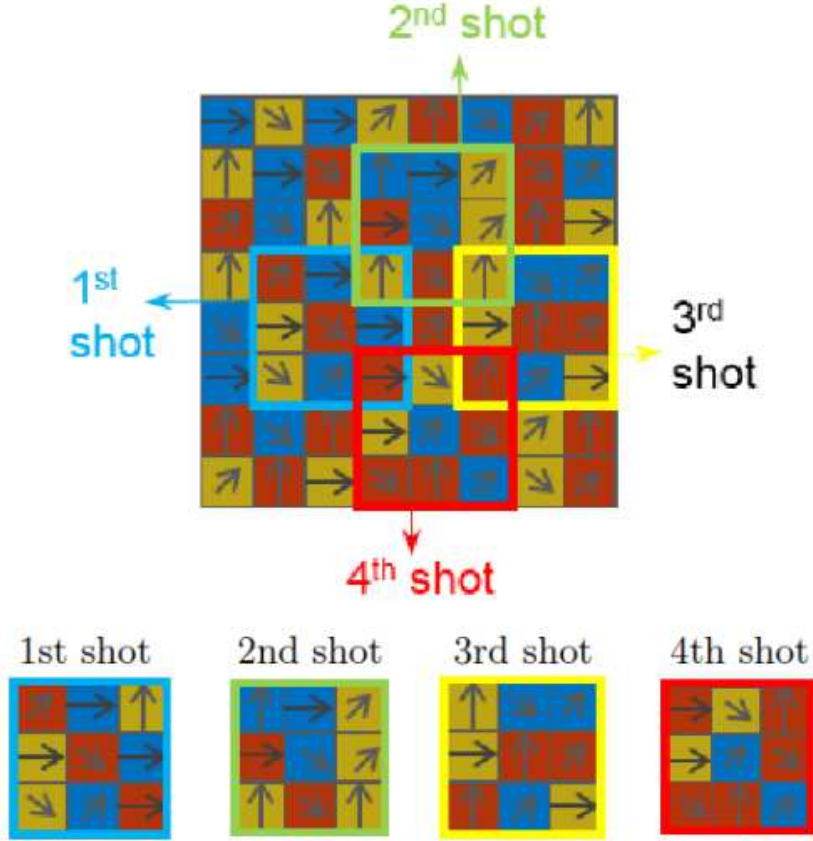


Figure 4.10: A spectral image plane is projected onto four different FPA locations, corresponding to the four prism rotation angles. This induces four different coding patterns.

As a comparison, an alternative method of generating 4-shot measurements is to replace the pixelated polarizer by a rotating linear polarizer in the imaging architecture, keeping the prism fixed. This 4-shot architecture also achieves a CS ratio of $\kappa = 17\%$ when 8 spectral channels are reconstructed. However, this rotating polarizer approach suffers from a fixed number of snapshots. It will fail to measure all three Stokes parameters with fewer than four snapshots, and it is unnecessary to capture more than four snapshots with duplicate information. Furthermore, during each snapshot measurement, a fixed spectral coding is applied with the same spatial and spectral information captured.

With the proposed prism rotation approach, one can select a proper number of snapshots with CS ratio ranging from $\kappa = 4.3\%$ to $\kappa = 17\%$. With each new snapshot

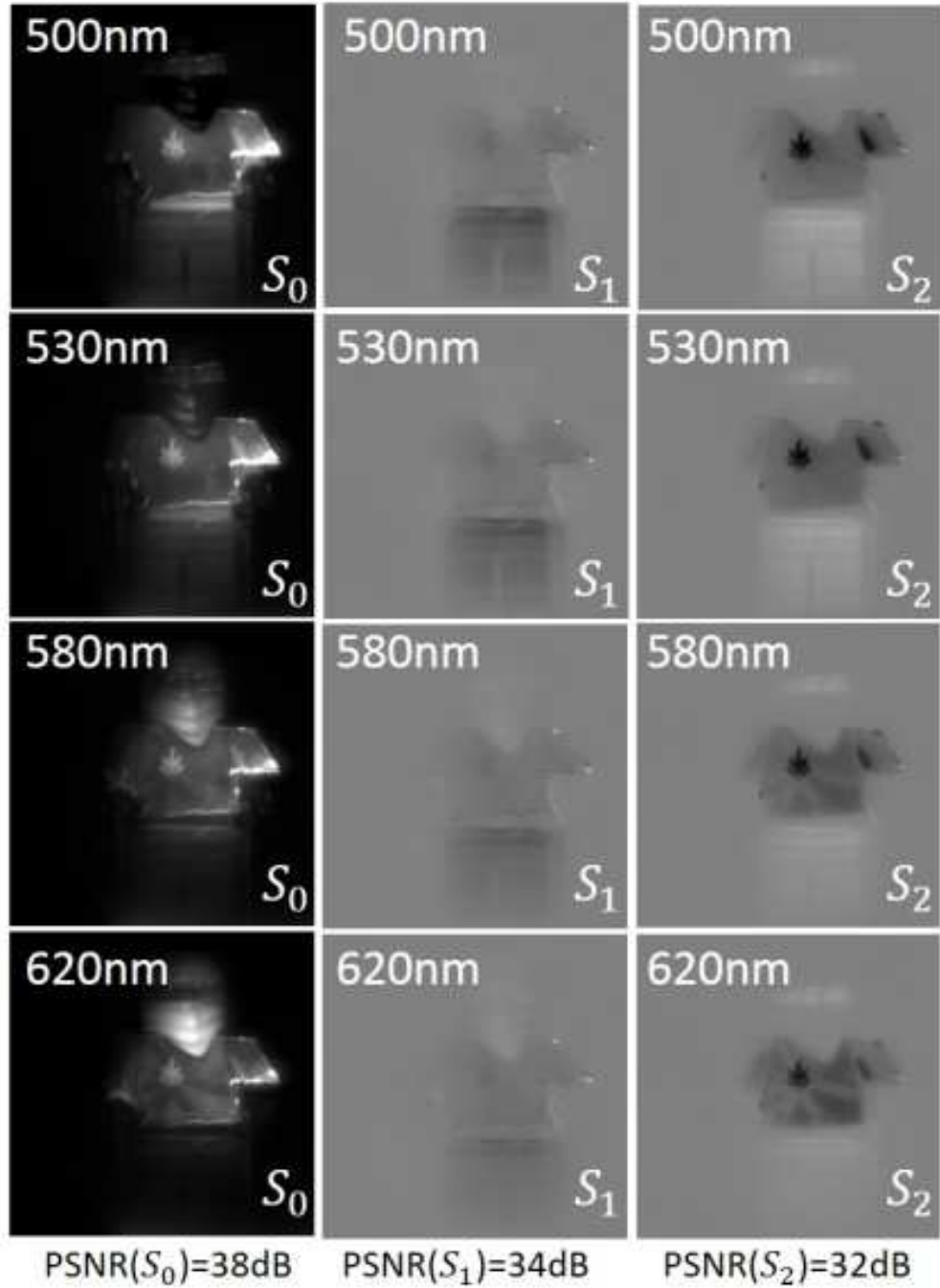


Figure 4.11: S_0 , S_1 and S_2 image planes reconstructed from 4 simulated snapshots are displayed in four spectral channels. The CS ratio is $\kappa = 17\%$. The average PSNRs for each Stokes image plane are indicated.

acquired, new spectral and polarization information is always obtained, significantly enhancing the spectral and polarization reconstruction quality.

4.6 Laboratory Experiments

4.6.1 Hardware Implementation and Calibration

In this section we describe a laboratory implementation and test of the proposed imaging system. The optical setup is shown in Fig. 4.12. Integrated CMOS polarization imaging sensors [93] and CCD polarization imaging sensors [94] have been extensively proposed in the literature, and DoFP polarimetry has been widely applied in polarization imaging [82,84,85]. An integrated spectral-polarization imaging sensor has also been proposed for spectral-polarization imaging [83]. For the initial experiments reported here, a relay optical system was constructed.

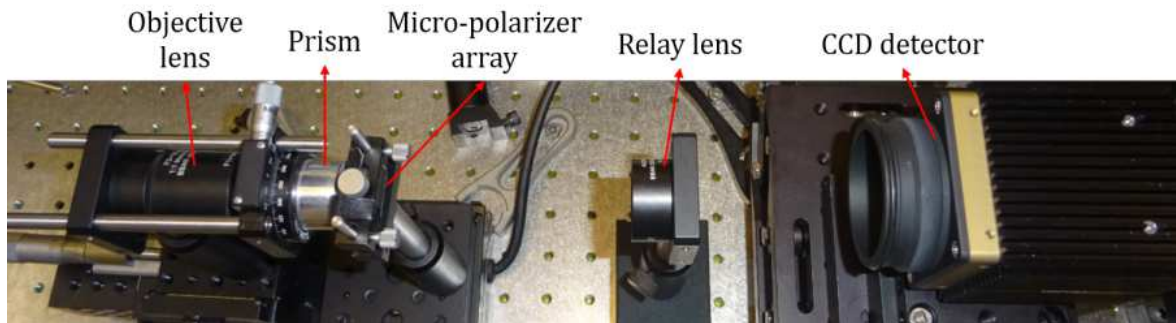


Figure 4.12: Laboratory implementation of the proposed architecture. Coded projections are acquired on a CCD camera.

A visible achromatic lens with 100 mm focal length (Thorlabs AC254-100-A-ML) is used for the objective lens. A custom double Amici prism with center wavelength 550nm is mounted on a rotating plate. A Moxtek periodic micropolarizer array with 7.4um pixel size is placed in the focal plane. A 50mm focal length lens is used to relay the micropolarizer array to a CCD camera (Imperx b2021) with 7.4um pixel size. A set of bandpass filters are used to capture several color filtered measurements on the FPA. To implement a random colored array, we randomly sampled the colored filter FPA measurements. Four snapshots are captured, one for each prism rotation angle. The CS ratios are $\kappa = 4.3\%, 8.6\%, 13\%, 17\%$ for $K = 1, 2, 3, 4$ snapshots, respectively.

Calibration was performed to estimate the measurement matrix \mathbf{H} accurately. First, we consider calibration of the prism rotation. The prism rotation axis differs

slightly from the center of the optical path, resulting in small shifts in the projection for different snapshots. This distance is measured by illuminating the target with 550nm monochromatic light, corresponding to the center wavelength of the Amici prism. Thus, no dispersion occurs during each rotation. The offsets are then calculated from the projection locations on the FPA.

Second, the spectral response of the imager needs to be measured in order to have an accurate spectrum reconstruction. The spectral responses of the bandpass filters used in the experiments were measured using a point spectrometer (Ocean Optics USB2000+). Similarly, the spectral responses of the CCD camera and the linear polarizer (used in first two experiments) are also taken into consideration. The vector representation \mathbf{t}_k in Eq. 4.10 is modified with the spectral response of the imaging system, that then changes the values in matrix \mathbf{H}_c expressed in Eq. 4.11.

Third, calibration of the periodic micro-polarizer array is needed for the Stokes parameter reconstruction. The misalignment between the micro-polarizer array and the FPA detector was measured by adding a linear polarizer in front of a white target. The linear polarizer, combined with the micro-polarizer array, produces periodic patterns on the FPA. Multiple periodic patterns are captured with several rotations of the linear polarizer. Misalignment between the micro-polarizer array and the camera is then acquired by calculating the proportions of 0° , 45° , 90° and 135° linear polarization intensities in each FPA pixel. The vector representation \mathbf{u}_c^k in Eq. 4.9 is then modified. Gray scale coding is obtained rather than the ideal binary coding. Finally, the matrix \mathbf{H}_c in Eq. 4.15 is modified based on the spectral and polarization calibration in order to match the experimental sensing process.

4.6.2 Experimental Results

Three experiments are presented to verify the capability of the proposed imager. In the first experiment, a linear polarizer is fixed after the target, constructing a linear polarized scene. This experiment aims at verifying the ability to recover the spectral information and the linear polarization angle contained in the scene. The ability to

reconstruct Stokes parameter images with various polarization angles is further verified in the second experiment, where a linear polarizer is placed after the target with variant azimuth angles. Finally, a third experiment is performed without a linear polarizer in the optical setup, aiming at recovering a scene with large fields of uniform, strong polarization.

During the first experiment, the linear polarizer is fixed at 0° azimuth angle. Four snapshots are captured with 0° , 90° , 180° and 270° prism rotations, respectively. The reconstructions of S_0 images in 8 spectral bands from 505nm to 650nm are displayed in Fig. 4.13 (b)-(i). Clear images in all 8 spectral channels are recovered.

Given the target is 0° linear polarized, then theoretically, the intensity of the S_1 images and S_0 images should be identical, and the intensity of S_2 images should be 0 in all the spectral bands. This is experimentally verified in Fig. 4.14.

The spectral performance of the proposed architecture is tested by comparing the reconstructed spectral signatures to the reference measurement from a point spectrometer (Ocean Optics USB2000+). In this experiment, spectral signatures of two selected points (P_1 and P_2) from the scene (shown in Fig. 4.13 (a)) are compared and displayed in Fig. 4.15.

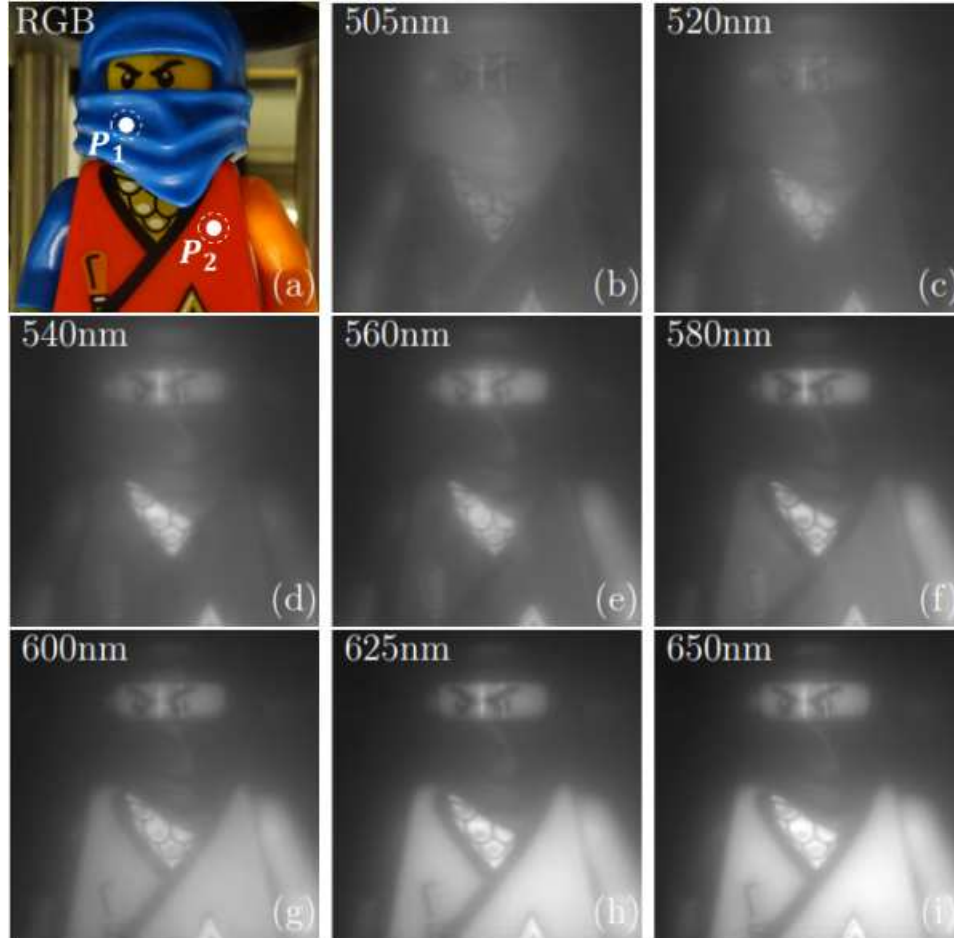


Figure 4.13: (a): The target is captured by an RGB camera. Two points P_1 and P_2 are selected for spectral signature comparison. (b)-(i): Reconstructed S_0 image planes are displayed at all 8 spectral wavelengths from 505nm to 650nm.

As the number of snapshots increases, better spectral reconstruction is expected. With three or four snapshots, the imager can provide higher accuracy. Small errors sources arise in characterizing the sensing matrix and the point spectrometer measurement noise. We demonstrate that the overall calibration error can be reduced as the number of shots increases.

The second experiment aims at validating the ability of the proposed imager to recover Stokes images of the object with different polarization angles. As such, the azimuth angles of the linear polarizer are changed. The intensities of S_1 and S_2 images follow the change with the azimuth angle of the linear polarizer. For instance,

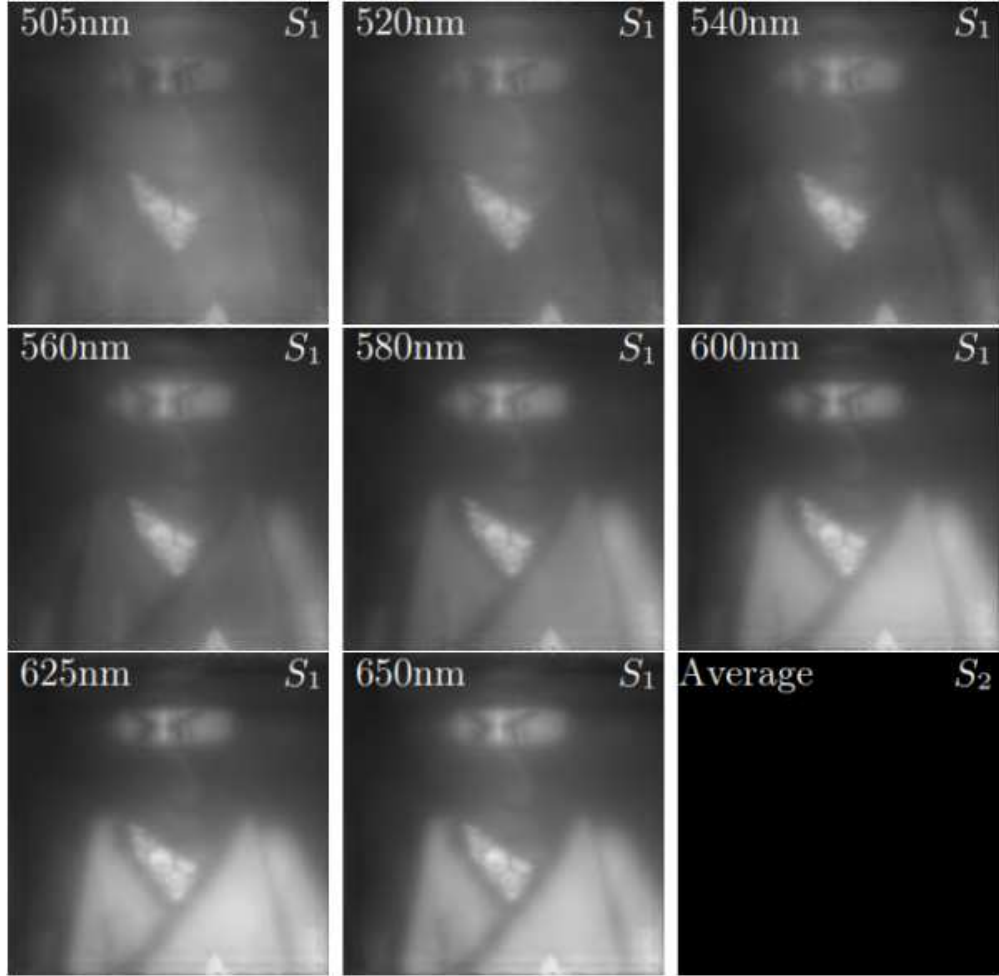


Figure 4.14: Reconstructed S_1 image planes at 8 spectral wavelengths and the average reconstruction of S_2 image plane. The S_1 image planes have the same intensities as reconstructed S_0 images because in this experiment the target is 0° polarized. Also, as expected, the average S_2 image plane has zero intensity.

the S_1 image has 0 intensity with a 45° polarized target, while the corresponding S_2 image reaches its highest intensity. Similarly, the S_1 image has a negative and strong intensity when the target is 90° polarized, and 0 intensity should be observed in the corresponding S_2 image. The S_1 and S_2 images in 620nm are displayed in Figs. 4.16 and 4.17, respectively. The intensities of the reconstructed S_1 and S_2 images follow the expected changes described above.

In the third experiment, a scene containing large fields of uniform, strong polarization is captured. As shown in Fig. 4.18 (a), the scene contains a toy combined

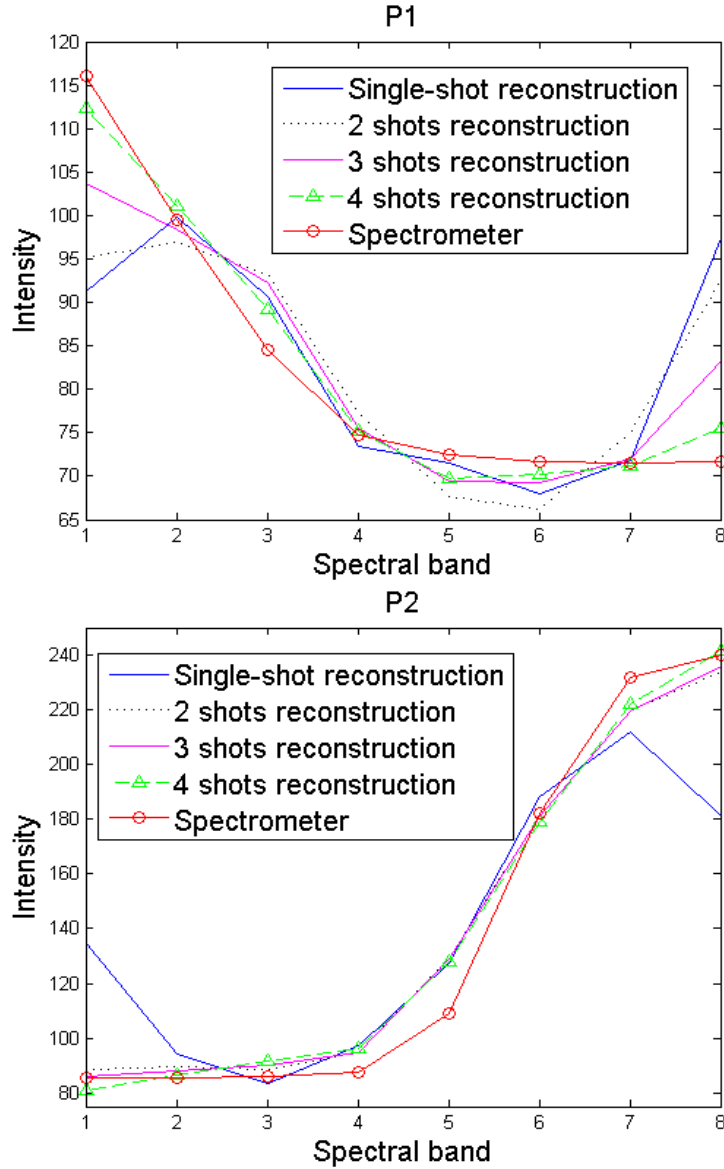


Figure 4.15: Spectral reconstructions of two selected points are compared with a spectrometer measurement.

with three pieces of polarizer film: One is cut into a sword shape, held in the right hand of the toy. The other two cover the eyes and legs of the toy, respectively. The reconstructed S_0 image planes for 8 spectral channels are displayed in Fig. 4.18 (b)-(i). Reduced intensity is observed in the areas covered by the polarizer films. Those areas become apparent in the reconstructed S_1 image planes shown in Fig. 4.19. In particular, the polarizer film covering the eyes of the toy shows high positive intensity in

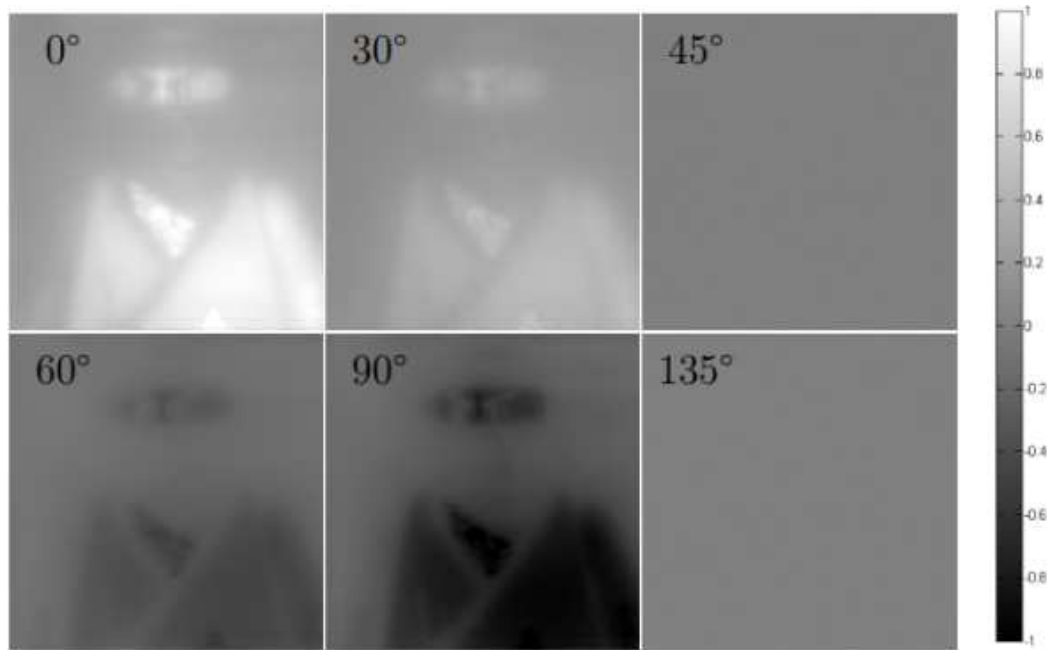


Figure 4.16: Reconstructed S_1 image planes at 600nm are shown for different polarization angles. The intensity of S_1 images changes with the azimuth angle of the linear polarizer.

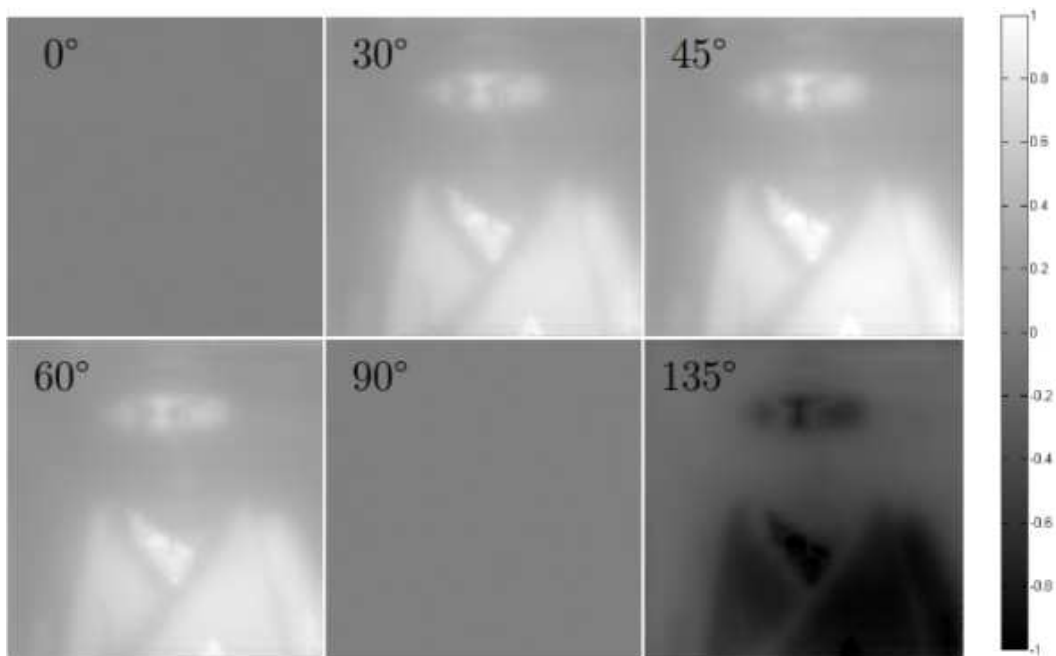


Figure 4.17: Reconstructed S_2 image planes at 600nm are shown for different polarization angles. The intensity of S_2 images changes with the azimuth angle of the linear polarizer.

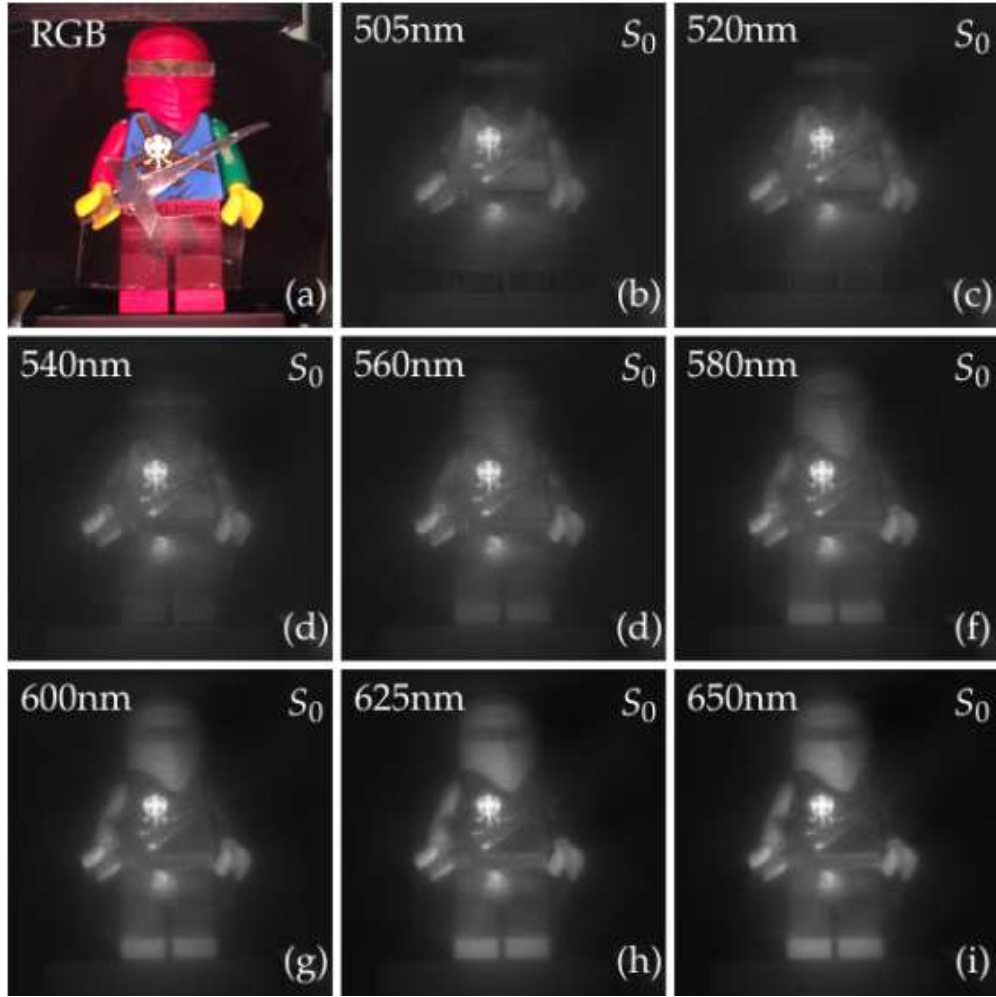


Figure 4.18: (a): The target is captured by an RGB camera. (b)-(i): Reconstructed S_0 image planes are displayed at all 8 spectral wavelengths from 505nm to 650nm.

S_1 image planes, while the polarizer film covering the legs introduces strong negative intensities. The sword shaped polarizer film has strong negative intensity in S_2 image planes displayed in Fig. 4.20 (a)-(h). Fig. 4.20 (i) shows the angle of polarization calculated at 625nm. The angle information is displayed in pseudo color. The polarizer films covering the eyes and legs of the toy have an average of 5° and 94° linear polarization, respectively. The sword shaped polarizer film has an average of 122° linear polarization.

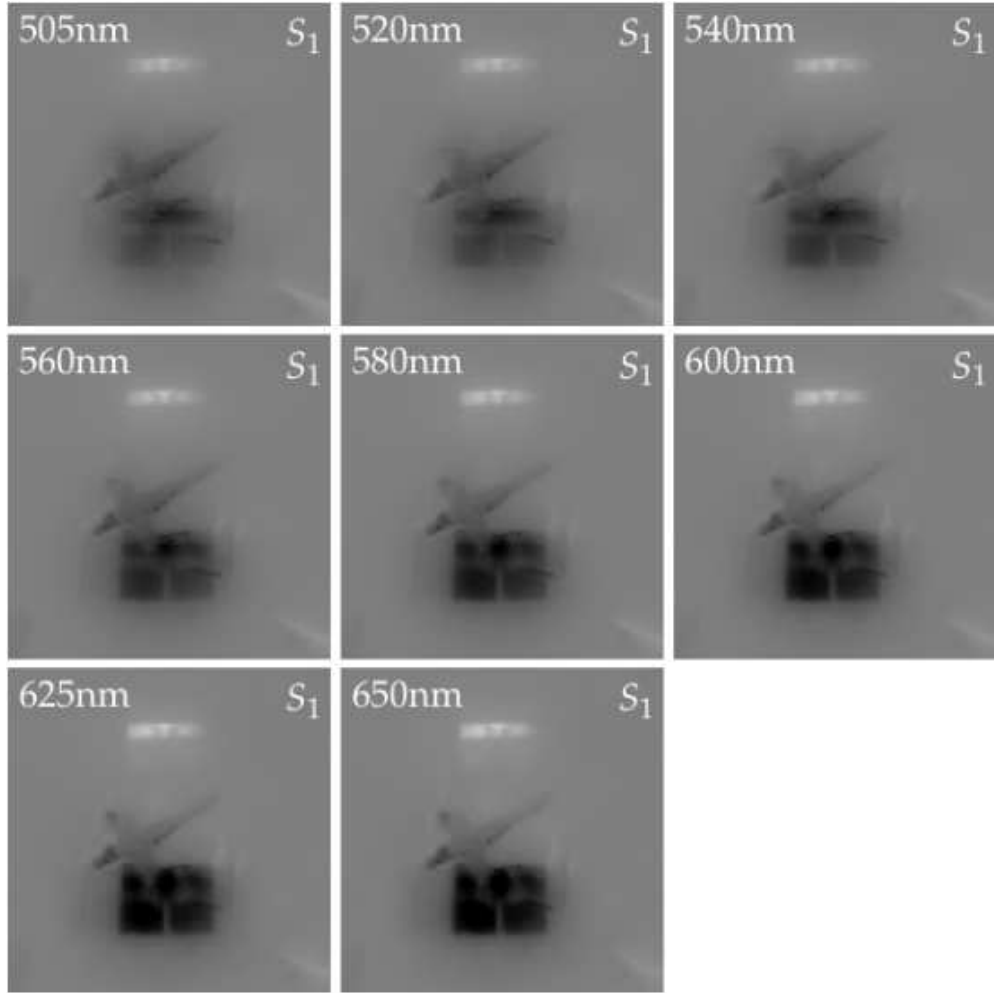


Figure 4.19: Reconstructed S_1 image planes at 8 spectral wavelengths are displayed. The polarizer film covering the eyes of the toy has strong positive S_1 components. Strong negative S_1 is observed with the polarizer film covering the legs of the toy.

4.7 Conclusion

A spectral polarization compressive imaging system was designed, analyzed, and experimentally tested. The image scene with spatial, spectral and polarization information is projected onto the FPA, producing several 2D compressive coded projections. A detailed mathematical model of the imager was presented, and an ℓ_1 regularized optimization algorithm was applied for reconstruction that takes advantage of sparsity. The polarizer and colored coding are designed with blue noise spatial patterns to enhance

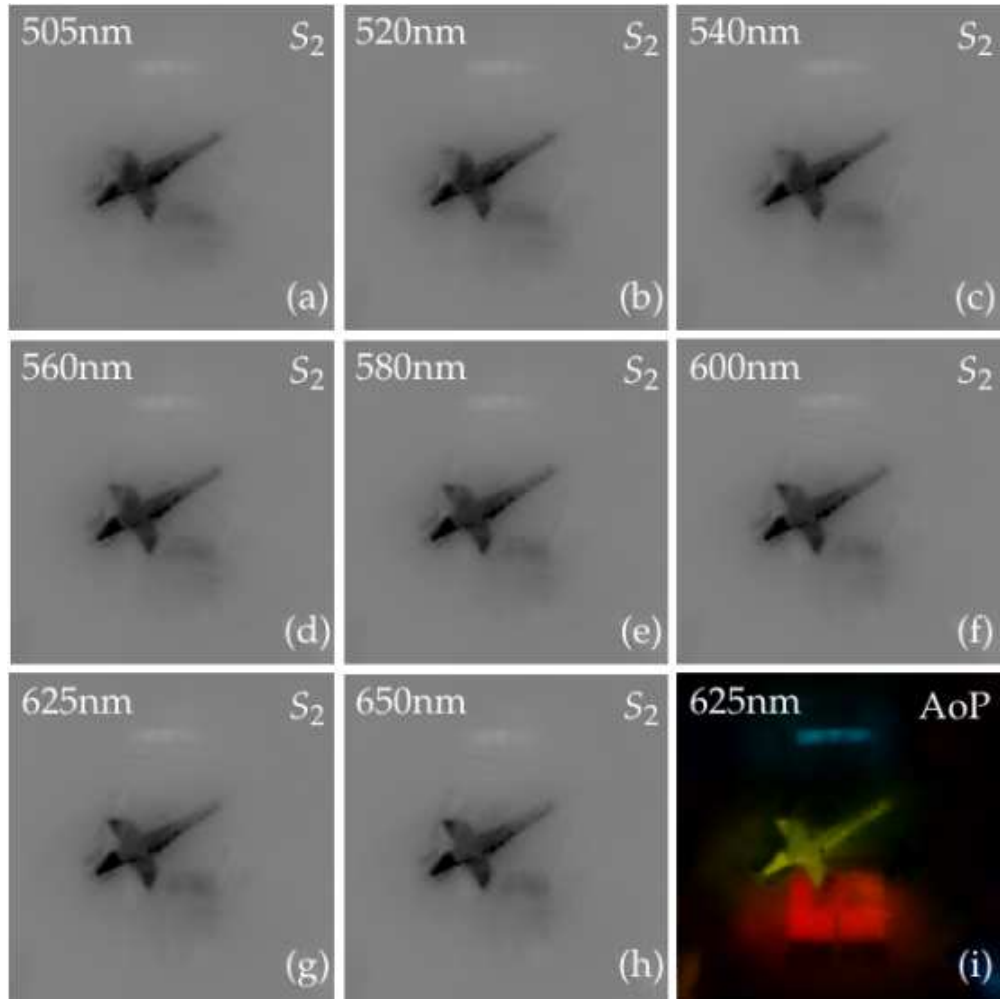


Figure 4.20: (a)-(h): Reconstructed S_2 image planes at 8 spectral wavelengths are displayed. The sword shaped polarizer film has strong negative S_2 components. (i): AoP image represented by pseudo color is computed at 625nm.

information capture and image reconstruction. Comparison between conventional compressive sensing random projections and blue noise code designs, demonstrates the advantages of the coding approach, resulting in better image reconstruction. Prism rotations are used to obtain multiple measurement shots, which change the spectral and polarization coding of the scene for every snapshot. Reconstructions are significantly enhanced as more snapshots are added. A set of laboratory experiments demonstrate successful reconstructions in spatial, spectral and polarization domains.

Chapter 5

CONCLUSIONS AND FUTURE WORK

In this dissertation, the development of a polar coded aperture compressive spectral imaging system and a pixelated-polarizer based compressive spectral polarization imaging system is described. Different from conventional high-dimensional imaging system where scanning and DoFP approaches are largely used, the newly proposed compressive high-dimensional imaging systems are capable of obtaining the full image cube from a few modulated 2D projections without performing scanning or sacrificing sensor resolution.

In the development of a polar coded aperture compressive spectral imager, a polar shaped coded aperture is designed and fabricated with spokes-rings structure. This polar coded aperture is placed on the focal plane of an objective lens, together with a circular variable filter. A low-resolution sensor integrates the modulated scene into 2D measurements. When mounted on spinning devices, this imager captures multiple measurement shots during a 2π rotation. Mathematical models are developed to characterize the spatial-spectral modulation process and continuous rotation motion. The aperture coding patterns are further optimized for reconstruction quality improvement. Computer simulations with two proposed mathematical models are performed. Reconstructions are compared between optimized and non-optimized coding patterns. A proof-of-concept experiment is conducted for further evaluations on the performance of the described imager.

Future research work on this spectral imager is twofold: 1. Efforts should be made on the development of robust modeling and image reconstruction methods regarding the rotation of the imager. 2. More accurate calibration procedures are necessary for better solutions on the coded aperture and rotation center misalignment

phenomenon.

In the dissertation, a novel compressive spectral polarization imaging system is developed. An integrated polarized color sensor combines with an double-Amici prism providing a 4D spatial, spectral and polarization modulation. A mathematical forward model is developed aiming at the direct recovery of Stokes spectral image planes. Linear polarization states are better reconstructed with well-designed blue noise polarization coding patterns. Multi-snapshots are enabled through the prism rotation. Computer simulations and a set of experiments are conducted, further validating the proposed imaging system.

Micro-polarizer array with blue noise distribution outperforms the random coding with 4dB difference in PSNR during a single snapshot comparison. Future work may include the fabrication of this blue-noise polarization pattern for additional experimental implementation. Full-Stokes snapshot spectral polarization imaging can be further developed by involving additional phase retarders in the proposed imaging system.

REFERENCES

- [1] Garini, Yuval, Ian T. Young, and George McNamara. "Spectral imaging: principles and applications." *Cytometry Part A* **69**.8: 735-747, 2006.
- [2] Shen, Hui-Liang, Jian-Fan Yao, Chunguang Li, Xin Du, Si-Jie Shao, and John Xin, "Channel selection for multispectral color imaging using binary differential evolution," *Appl. Opt.* **53**, 634-642, 2014.
- [3] Eismann, Michael T., Alan D. Stocker, and Nasser M. Nasrabadi, "Automated hyperspectral cueing for civilian search and rescue." *Proceedings of the IEEE* **97**.6: 1031-1055, 2009.
- [4] Tyo, J. Scott, Dennis L. Goldstein, David B. Chenault, and Joseph A. Shaw. "Review of passive imaging polarimetry for remote sensing applications." *Applied optics* **45**, no. 22: 5453-5469, 2006.
- [5] Curran, Paul J. "Polarized visible light as an aid to vegetation classification." *Remote Sensing of Environment* **12**, no. 6: 491-499, 1982.
- [6] Farlow, Craig Alan, David B. Chenault, J. Larry Pezzaniti, Kevin Deane Spradley, and Michael G. Gulley. "Imaging polarimeter development and applications." *Polarization Analysis and Measurement IV*, vol. **4481**, pp. 118-126, 2002.
- [7] Tyo, J. Scott, and Theodore S. Turner. "Variable-retardance, Fourier-transform imaging spectropolarimeters for visible spectrum remote sensing." *Applied Optics* **40**, no. 9: 1450-1458, 2001.
- [8] Candes, Emmanuel J., and Michael B. Wakin. "An introduction to compressive sampling." *IEEE signal processing magazine* **25**, no. 2: 21-30, 2008.
- [9] Taubman, David, and Michael Marcellin. *JPEG2000 image compression fundamentals, standards and practice: image compression fundamentals, standards and practice*. Springer Science & Business Media, 2012.
- [10] Le Gall, Didier. "MPEG: A video compression standard for multimedia applications." *Communications of the ACM* **34**, no. 4: 46-58, 1991.

- [11] Duarte, Marco F., Mark A. Davenport, Dharmpal Takhar, Jason N. Laska, Ting Sun, Kevin F. Kelly, and Richard G. Baraniuk. "Single-pixel imaging via compressive sampling." *IEEE signal processing magazine* **25**, no. 2: 83-91, 2008.
- [12] Davis, Brandon M., Amanda J. Hemphill, Derya Cebeci Maltas, Michael A. Zipper, Ping Wang, and Dor Ben-Amotz. "Multivariate hyperspectral Raman imaging using compressive detection." *Analytical chemistry* **83**, no. 13: 5086-5092, 2011.
- [13] Colaco, Andrea, Ahmed Kirmani, Gregory A. Howland, John C. Howell, and Vivek K. Goyal. "Compressive depth map acquisition using a single photon-counting detector: Parametric signal processing meets sparsity." *Computer Vision and Pattern Recognition (CVPR), 2012 IEEE Conference on*, pp. 96-102, 2012.
- [14] Howland, Gregory A., Petros Zerom, Robert W. Boyd, and John C. Howell. "Compressive sensing LIDAR for 3D imaging." *Lasers and Electro-Optics (CLEO), 2011 Conference on*, pp. 1-2. IEEE, 2011.
- [15] Wagadarikar, Ashwin, Renu John, Rebecca Willett, and David Brady. "Single disperser design for coded aperture snapshot spectral imaging." *Applied optics* **47**, no. 10 B44-B51, 2008.
- [16] Arce, Gonzalo R., David J. Brady, Lawrence Carin, Henry Arguello, and David S. Kittle. "Compressive coded aperture spectral imaging: An introduction." *Signal Processing Magazine* **31**, no. 1: 105-115, 2014.
- [17] Wu, Yuehao, Iftexhar O. Mirza, Gonzalo R. Arce, and Dennis W. Prather. "Development of a digital-micromirror-device-based multishot snapshot spectral imaging system." *Optics letters* **36**, no. 14: 2692-2694, 2011.
- [18] Arguello, Henry, Hoover Rueda, Yuehao Wu, Dennis W. Prather, and Gonzalo R. Arce. "Higher-order computational model for coded aperture spectral imaging." *Applied optics* **52**, no. 10: D12-D21, 2013.
- [19] Rueda, Hoover, Henry Arguello, and Gonzalo R. Arce. "DMD-based implementation of patterned optical filter arrays for compressive spectral imaging." *JOSA A* **32**, no. 1: 80-89, 2015.
- [20] Arguello, Henry, and Gonzalo R. Arce. "Colored coded aperture design by concentration of measure in compressive spectral imaging." *IEEE Transactions on Image Processing* **23**, no. 4: 1896-1908, 2014.
- [21] Correa, Claudia V., Henry Arguello, and Gonzalo R. Arce. "Snapshot colored compressive spectral imager." *JOSA A* **32**, no. 10: 1754-1763, 2015.

- [22] Arguello, Henry, Hoover F. Rueda, and Gonzalo R. Arce. “Spatial super-resolution in code aperture spectral imaging.” *Compressive Sensing, International Society for Optics and Photonics*, vol. **8365**, p. 83650A, 2012.
- [23] Parada-Mayorga, Alejandro, and Gonzalo R. Arce. “Colored coded aperture design in compressive spectral imaging via minimum coherence.” *IEEE Transactions on Computational Imaging* **3**, no. 2: 202-216, 2017.
- [24] Yuan, Xin, Tsung-Han Tsai, Ruoyu Zhu, Patrick Llull, David Brady, and Lawrence Carin. “Compressive hyperspectral imaging with side information.” *IEEE Journal of Selected Topics in Signal Processing* **9**, no. 6: 964-976, 2015.
- [25] Lin, Xing, Yebin Liu, Jiamin Wu, and Qionghai Dai. “Spatial-spectral encoded compressive hyperspectral imaging.” *ACM Transactions on Graphics (TOG)* **33**, no. 6: 233, 2014.
- [26] Illsley, Rolf F., Alfred J. Thelen, and Joseph H. Apfel. “Circular variable filter.” U.S. Patent 3,442,572, issued May 6, 1969.
- [27] Soldevila, F., E. Irlas, V. Durn, P. Clemente, Mercedes Fernandez-Alonso, Enrique Tajahuerce, and Jess Lancis. “Single-pixel polarimetric imaging spectrometer by compressive sensing.” *Applied Physics B* **113**, no. 4: 551-558, 2013.
- [28] Tsai, Tsung-Han, and David J. Brady. “Coded aperture snapshot spectral polarization imaging.” *Applied optics* **52**, no. 10: 2153-2161, 2013.
- [29] Tsai, Tsung-Han, Xin Yuan, and David J. Brady. “Spatial light modulator based color polarization imaging.” *Optics express* **23**, no. 9: 11912-11926, 2015.
- [30] Lustig, Michael, David Donoho, and John M. Pauly. “Sparse MRI: The application of compressed sensing for rapid MR imaging.” *Magnetic resonance in medicine* **58**, no. 6: 1182-1195, 2007.
- [31] Choi, Kerkil, and David J. Brady. “Coded aperture computed tomography.” *Adaptive Coded Aperture Imaging, Non-Imaging, and Unconventional Imaging Sensor Systems, International Society for Optics and Photonics*, vol. **7468**, p. 74680B, 2009.
- [32] Marwah, Kshitij, Gordon Wetzstein, Ashok Veeraraghavan, and Ramesh Raskar. “Compressive light field photography.” *ACM SIGGRAPH 2012 Talks*, p. 42, 2012.
- [33] Llull, Patrick, Xuejun Liao, Xin Yuan, Jianbo Yang, David Kittle, Lawrence Carin, Guillermo Sapiro, and David J. Brady. “Coded aperture compressive temporal imaging.” *Optics express* **21**, no. 9: 10526-10545, 2013.

- [34] Feng, Weiyi, Hoover Rueda, Chen Fu, Gonzalo R. Arce, Weiji He, and Qian Chen. “3D compressive spectral integral imaging.” *Optics Express* **24**, no. 22: 24859-24871, 2016.
- [35] Rueda, Hoover, Chen Fu, Daniel L. Lau, and Gonzalo R. Arce. “Single Aperture Spectral+ ToF Compressive Camera: Toward Hyperspectral+ Depth Imagery.” *IEEE Journal of Selected Topics in Signal Processing* **11**, no. 7: 992-1003, 2017.
- [36] Pinker, A. and C. Smith, “Vulnerability of GPS Signal to Jamming”, *GPS Solutions*, **3**(2), 1999.
- [37] Aboutalib, O., B. Awalt, A. Fung, B. Thai, J. Leibs, T. J. Klausutis, R. Wehling and M. James, “All source adaptive fusion for aided navigation in non-GPS environment”, *2007 SPIE Defence & Security Symposium, Visual Information Processing XVI*, **6575**, April 2007.
- [38] Sinopoli, B., M. Micheli, G. Donato, T. J. Koo, “Vision based navigation for an unmanned aerial vehicle”, *Robotics and Automation Proceedings of 2001 ICRA. IEEE International Conference*, **2**, pp.1757-1764, 2001.
- [39] Sattigeri, R., A. J. Calise, and J. Evers, “An Adaptive Vision-Based Approach to Decentralized Formation Control”, *Journal of Aerospace Computing, Information, and Communication* **1**(12), 502-525, 2004.
- [40] Cesetti, A., E. Frontoni, A. Mancini, P. Zingaretti, and S. Longhi, “A vision-based guidance system for UAV navigation and safe landing using natural landmarks”, *J. Intell. Robot. Syst.*, **57**, pp. 233257, 2009.
- [41] Kwon, H., D. Rosario, N. Gupta, M. Thielke, D. Smith, P. Rauss, P. Gillespie, and N. Nasrabadi, “Hyperspectral Imaging and Obstacle Detection for Robotics Navigation”, *U.S. Army Research Laboratory Technical Report ARL-TR-3639*, September 2005.
- [42] Aguilera, C., F. Barrera, F. Lumbreras, A.D. Sappa, R. Toledo, “Multispectral image feature points”, *Sensors*, **12**(9), pp. 12661-12672, 2012.
- [43] Murakami, Y., M. Yamaguchi and N. Ohyama, “Hybrid-resolution multispectral imaging using color filter array,” *Opt. Express*, **20**(7), 7173-7183, 2012.
- [44] Garini, Y., I. T. Young, G. McNamara, “Spectral imaging: Principles and applications”, *Cytometry Part A*, **69A**(8), 735-747, 2006.
- [45] Yang, S. “Circular, variable, broad-bandpass filters with induced transmission at 200-1100 nm,” *Appl. Opt.* **32**, 4836-4842, 1993.
- [46] Lepper, J. M., M. K. Diab, “Optical filter for spectroscopic measurement and method of producing the optical filter”, US Patent 5 760 910, 1998.

- [47] Anthon, E. M., “Compact spectrometer device”, US Patent 6 057 925, 2000.
- [48] Morozova, S. P., P. A. Morozov, V. I. Sapritsky, B. E. Lisiansky, N. L. Dovgilov, “VNIIOFI Spectroradiometer Based on a Circular Variable Filter for the Spectral Range from 2.5 μm up to 14 μm ”, *AIP Conf. Proc.* **684**(595), 2003.
- [49] Dombrowski, M., J. Lorenz, “Imaging spectroradiometer”, US Patent 5 424 543, 1995.
- [50] Cabib, D., M. Lavi, A. Gil, E. Ohel, J. Dolev, U. Milman, “A Long Wave Infrared (LWIR) spectral imager (7.7 to 12.3 μ) based on cooled detector array and high resolution Circular Variable Filter (CVF)”, *Proc. SPIE 8896, Electro-Optical and Infrared Systems: Technology and Applications X*, **88960R**, 2013.
- [51] Duarte, M., F., and R. G. Baraniuk, “Kronecker product matrices for compressive sensing.” *2010 IEEE International Conference on Acoustics, Speech and Signal Processing. IEEE*, pp. 3650-3653, 2010.
- [52] Duarte, M., F., and R. G. Baraniuk, “Kronecker compressive sensing.” *IEEE Transactions on Image Processing* **21**(2), pp.494-504, 2012.
- [53] Signoretto, M., R. Van de Plas, B. De Moor, and J. A. Suykens, “Tensor versus matrix completion: a comparison with application to spectral data”, *IEEE Signal Processing Letters* **18**(7), pp. 403-406, 2011.
- [54] Golbabaee, M., and P. Vandergheynst, “Hyperspectral image compressed sensing via low-rank and joint-sparse matrix recovery”, *2012 IEEE International Conference On Acoustics, Speech And Signal Processing (ICASSP)*, pp. 2741-2744, 2012.
- [55] Liu, L., J. Yan, X. Zheng, H. Peng, D. Guo and X. Qu, “Karhunen-Loève transform for compressive sampling hyperspectral images”. *Optical Engineering*, **54**(1), pp. 014106-014106, 2015.
- [56] Figueiredo, M., R. D. Nowak, and S. J. Wright, “Gradient projection for sparse reconstruction: Application to compressed sensing and other inverse problems,” *IEEE J. of Selected Topics in Signal Processing*, **1**, pp. 586597, 2007.
- [57] Schwartz, E. F., D. N. Greve, G. Bonmassar, “Space-variant active vision: Definition, overview and examples”, *Neural Networks* **8**, 1297-1308, 1995.
- [58] Traver, V., F., A. Bernardino, “A review of log-polar imaging for visual perception in robotics”, *Robotics and Autonomous Systems*, **58**(4), 378-398, 2010.
- [59] Buonocore, M., H., W. R. Brody, A. Macovsli, and S. L. Wood, “Polar pixel kalman filter for limited data computed tomography (CT) image reconstruction,” *SPIE Recent and future developments in medical imaging II*, **26**, pp. 109114, 1979.

- [60] Herbert, T., R. Leahy, and M. Singh, “Fast MLE for SPECT using an intermediate polar representation and a stopping criterion,” *IEEE Trans. Nucl. Sci.*, **35**, pp. 615619, 1988.
- [61] Israel-Jost, V., P. Choquet, S. Salmon, C. Blondet, E. Sonnendrucker, and A. Costantinesco, “Pinhole SPETC imaging: Compact projection/backprojection operator for efficient algebraic reconstruction,” *IEEE Trans. Med. Imag.*, **25**, pp. 158167, 2006.
- [62] Sauve, A. C., A. O. Hero, W. L. Rogers, S. J. Wilderman, and N. H. Clinthorne, “3D image reconstruction for a Compton SPECT camera model”, *IEEE Trans. Nucl. Sci.*, vol. **46**, pp. 20752084, 1999.
- [63] Mora, C., M. Rafecas, “Polar pixels for high resolution small animal PET”, *IEEE Nuclear Science Symposium Conference Record*, **5**, pp.2812-2817, 2006.
- [64] Galvis, L., H. Arguello, and Gonzalo R. Arce. “Coded aperture design in mismatched compressive spectral imaging.” *Applied optics* **54**, no. 33, 9875-9882, 2015.
- [65] Galvis, L., D. Lau, X. Ma, H. Arguello, and G. R. Arce. “Coded aperture design in compressive spectral imaging based on side information.” *Applied optics* **56**, no. 22: 6332-6340, 2017.
- [66] Cuadros, A. P. and Gonzalo R. Arce. “Coded aperture optimization in compressive X-ray tomography: a gradient descent approach.” *Optics Express* **25**, no. 20: 23833-23849, 2017.
- [67] Duarte-Carvajalino J. M. and G. Sapiro, “Learning to Sense Sparse Signals: Simultaneous Sensing Matrix and Sparsifying Dictionary Optimization,” in *IEEE Transactions on Image Processing*, vol. **18**, no. 7, pp. 1395-1408, July 2009.
- [68] Candes, E., and J. Romberg, “Sparsity and incoherence in compressive sampling.” *Inverse problems* vol. **23** no.3, 2007.
- [69] Xu, J., Y. Pi, Z. Cao, “Optimized Projection Matrix for Compressive Sensing”, *EURASIP, J. Adv. Signal Process*, 2010.
- [70] Abolghasemi, V., S. Ferdowsi and S. Sanei. “A gradient-based alternating minimization approach for optimization of the measurement matrix in compressive sensing.” *Signal Processing* **92.4**, 999-1009, 2012.
- [71] Cuadros, A. P., C. Peitsch, H. Arguello, G. R. Arce, “Coded aperture optimization for compressive X-ray tomosynthesis,” *Optics express*, **23**(25), 32788-32802, 2015.

- [72] Correa, C. V., H. Arguello, and G. R. Arce, "Spatiotemporal blue noise coded aperture design for multi-shot compressive spectral imaging," *J. Opt. Soc. Am. A* **33**, 2312-2322, 2016.
- [73] Lau, D. L., R. Ulichney, and G. R. Arce, "Fundamental characteristics of halftone textures: blue noise and green noise." *IEEE Signal Processing Magazine* vol. **20** no. 4: 28-38, 2003.
- [74] Rodriguez, J. B., G. R. Arce, and D. L. Lau, "Blue-noise multitone dithering." *IEEE Transactions on Image Processing* vol. **17** no. 8: 1368-1382, 2008.
- [75] Seldowitz, M. A., J. P. Allebach, and D. W. Sweeney, "Synthesis of digital holograms by direct binary search", *Applied Optics* **26**(14), 2788-2798, 1987.
- [76] Analoui, M., and J. P. Allebach, "Model-based halftoning using direct binary search." *SPIE/IS&T Symposium on Electronic Imaging: Science and Technology. International Society for Optics and Photonics*, 1992.
- [77] Sellar, R. G, and G. D. Boreman, "Classification of imaging spectrometers for remote sensing applications", *Opt. Eng.*, **44**(1), 013602-013602-3, 2005.
- [78] Chen, C., Y. Zhao, D. Liu, Q. Pan, Y. Cheng, "Polarization and Spectral Information Jointly Utilization in Targets Classification under Different Weather Conditions," *Photonics and Optoelectronic (SOPO)*, pp.1,4, 19-21, 2010.
- [79] Pu, Y., W. B. Wang, G. C. Tang, F. Zeng, S. Achilefu, J. H. Vitenson, I. Sawczuk, S. Peters, J. M. Lombardo, R. R. Alfano, "Spectral polarization imaging of human prostate cancer tissue using a near-infrared receptor-targeted contrast agent", *Technol Cancer Res Treat*, **4**(4) 429-436, 2005.
- [80] Bishop, K. P., H. D. McIntire, M. P. Fetrow, and L. McMackin, "Multispectral polarimeter imaging in the visible to near IR", *Targets and Backgrounds: Characterization and Representation, Proc. SPIE* **3699**, 49-57, 1999.
- [81] Loe, R. S. and M. J. Duggin, "Hyperspectral imaging polarimeter design and calibration," *Polarization Analysis, Measurement, and Remote Sensing IV, Proc. SPIE*, **4481**, 195-205, 2002.
- [82] Gao, S. and V. Gruev, "Bilinear and bicubic interpolation methods for division of focal plane polarimeters", *Optics Express*, **19**(27), 26161-26173, 2011.
- [83] Kulkarni, M. and V. Gruev, "Integrated spectral-polarization imaging sensor with aluminium nanowire polarization filters", *Optics Express*, **20**, 22997-23012, 2012.
- [84] Powell, S. B., and V. Gruev, "Calibration methods for division-of-focal-plane polarimeters", *Optics Express*, **21**(18), 21039-21055, 2013.

- [85] Murakami, Y., M. Yamaguchi and N. Ohyama, “Hybrid-resolution multispectral imaging using color filter array,” *Opt. Express*, **20**(7), 7173-7183, 2012.
- [86] Zhao, X., F. Boussaid, A. Bermak, and V. G. Chigrinov, “Thin Photo-Patterned Micropolarizer Array for CMOS Image Sensors,” *IEEE Circuits Devices Mag*, **21**, 805-807, 2009.
- [87] Guo, J., and D. Brady, “Fabrication of thin-film micropolarizer arrays for visible imaging polarimetry,” *Appl. Opt.*, **39**, 1486-1492, 2000.
- [88] Lukac, R., and K. N. Plataniotis, “Color filter arrays: design and performance analysis,” *IEEE Trans. Consumer Electronics* **51**(4), 1260-1267, 2005.
- [89] Nordin, G. P., J. T. Meier, P. C. Deguzman and M. W. Jones, “Micropolarizer array for infrared imaging polarimetry,” *J. Opt. Soc.*, Vol. **16**, 1168-1174 1999.
- [90] Pezzaniti, J. L., and R. A. Chipman, “Mueller matrix imaging polarimetry”, *Opt. Eng.* **34**, 1558-1568 (1995).
- [91] Chipman, R. A., “Polarization diversity active imaging,” *Proc. SPIE*, **3170**, 68-73 (1997).
- [92] Kittle, D., K. Choi, A. Wagadarikar, and D. J. Brady, “Multiframe image estimation for coded aperture snapshot spectral imagers”, *Appl. Opt.* **49**, 6824-6833, 2010.
- [93] Tokuda, T., S. Sato, H. Yamada, K. Sasagawa, and J. Ohta, “Polarisation-analysing CMOS photosensor with monolithically embedded wire grid polarizer,” *Electron. Lett.* **45**(4), 228-230, 2009.
- [94] Gruev, V., R. Perkins, and T. York, “CCD polarization imaging sensor with aluminum nanowire optical filters,” *Opt. Express* **18**, 19087-19094, 2010.

Appendix A

COPYRIGHT NOTICE

This appendix contains the copyright notices for the contents of this dissertation. Chapter 2 was published in the IEEE transactions on Computational Imaging.

© 2017 IEEE. Reprinted, with permission, from Chen Fu, Micheal Don, Gonzalo R. Arce, Compressive Spectral Imaging via Polar Coded Aperture, IEEE trans. on ComputationalImaging, Sept, 2017.

In reference to IEEE copyrighted material which is used with permission in this thesis, the IEEE does not endorse any of University of Delaware's products or services. Internal or personal use of this material is permitted. If interested in reprinting/republishing IEEE copyrighted material for advertising or promotional purposes or for creating new collective works for resale or redistribution, please go to http://www.ieee.org/publications_standards/publications/rights/rights_link.html to learn how to obtain a License from RightsLink.

Chapter 4 was published in the Journal of the Optical Society of America A (JOSA A).

© 2015 Optical Society of America.

One print or electronic copy of these papers may be made for personal use only. Systematic reproduction and distribution, duplication of any material in these papers for a fee or for commercial purposes, or modifications of the content of these papers are prohibited. For further information regarding Optical Society of America copyright and licensing information go to https://www.osapublishing.org/submit/review/copyright_permissions.cfm#posting

Appendix B
DISCLAIMER

Figures presented in this dissertation were not endorsed by the trademark owners and are used here to illustrate the quality of obtained reconstructions from compressive spectral imaging and compressive spectral polarization measurements and the proposed methods. The LEGO Group of companies does not sponsor, authorize or endorse the images in this dissertation. © 2018 The LEGO Group. All Rights Reserved. <https://www.lego.com/en-us/legal/legal-notice/fair-play>